Leipzig University
Faculty of Physics and Earth Sciences
Institute for Meteorology

Leibniz Institute for Tropospheric Research

Co-located observations of liquid and ice precipitation hydrometeors with a two-dimensional video disdrometer, a holographic cloud in-situ sonde, and active remote sensing

Master's thesis

Tom Gaudek

Course of studies:
Meteorology

Contact person:
Dr. Patric Seifert, TROPOS

Committee:
Jun.-Prof. Dr. Heike Kalesse-Los, LIM
Prof. Dr. Andreas Macke, TROPOS

submitted: 29 February 2024

Contents

Chapter 1

Introduction

More frequent and intense heavy precipitation events worldwide are one of the effects of ongoing global climate change (Douville et al., 2021) and pose a threat to people in the affected regions. For accurate predictions of such extreme events as well as for precise numerical weather forecasts in general, the formation and evolution of clouds as one of the main components in the atmospheric system needs to be better understood (e.g. Baumgardner et al., 2012). This can be achieved, for example, by further investigations of cloud microphysical processes, particularly those linked to precipitation formation. Clouds responsible for the same type of precipitation may have different characteristics. Rain, for example, can precipitate from liquid water clouds or from ice or mixed-phase clouds (MPC) and is therefore referred to as warm rain and cold rain, respectively. Figure 1.1 shows a global overview of the percentage of the cloud-top thermodynamic phase during rain events derived by spaceborne remote sensing, averaged from 2006 to 2011 (Mülmenstädt et al., 2015). It was found that the cloud-top phase fraction differs particularly over the continents and over the oceans. While cold rain dominates over land, the cloud-top phase during rain events over the oceans varies for different latitudes with warm rain dominating in the tropical and subtropical oceans outside the intertropical convergence zone. Furthermore, the cloud-top phase fractions strongly variate seasonally (Mülmenstädt et al., 2015).

Aerosol particles play an essential role in cloud formation and development, as they determine the initial state of a cloud system (Forster et al., 2021; Lohmann and Feichter, 2005). In air masses saturated with respect to liquid water they may act as cloud condensation nuclei inducing cloud droplet formation. For temperatures below 0°C, some types of aerosol particles may additionally act as ice nucleating particles initiating heterogeneous ice formation if the air is saturated with respect to ice. Below −37°C, this process may be accompanied by homogeneous ice formation which does not require aerosol particles

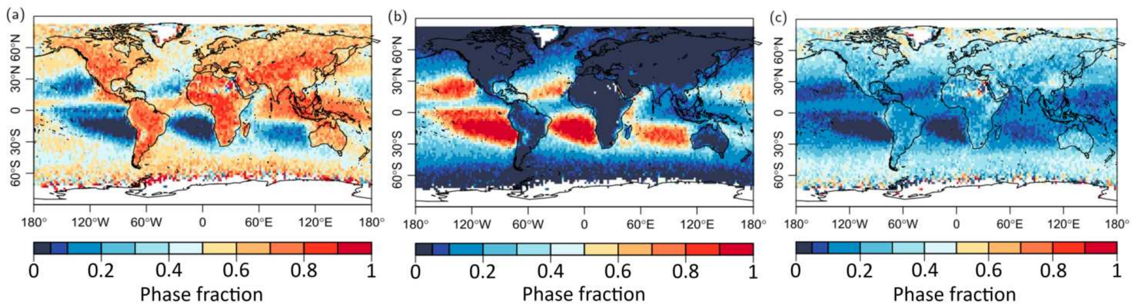

Figure 1.1: Cloud phase fractions during rain events divided into (a) ice phase, (b) liquid phase, and (c) mixed phase. CloudSat-CALIPSO data, averaged over five years (2006 – 2011) using a global 2° x 2° grid (adapted from Mülmenstädt et al., 2015).

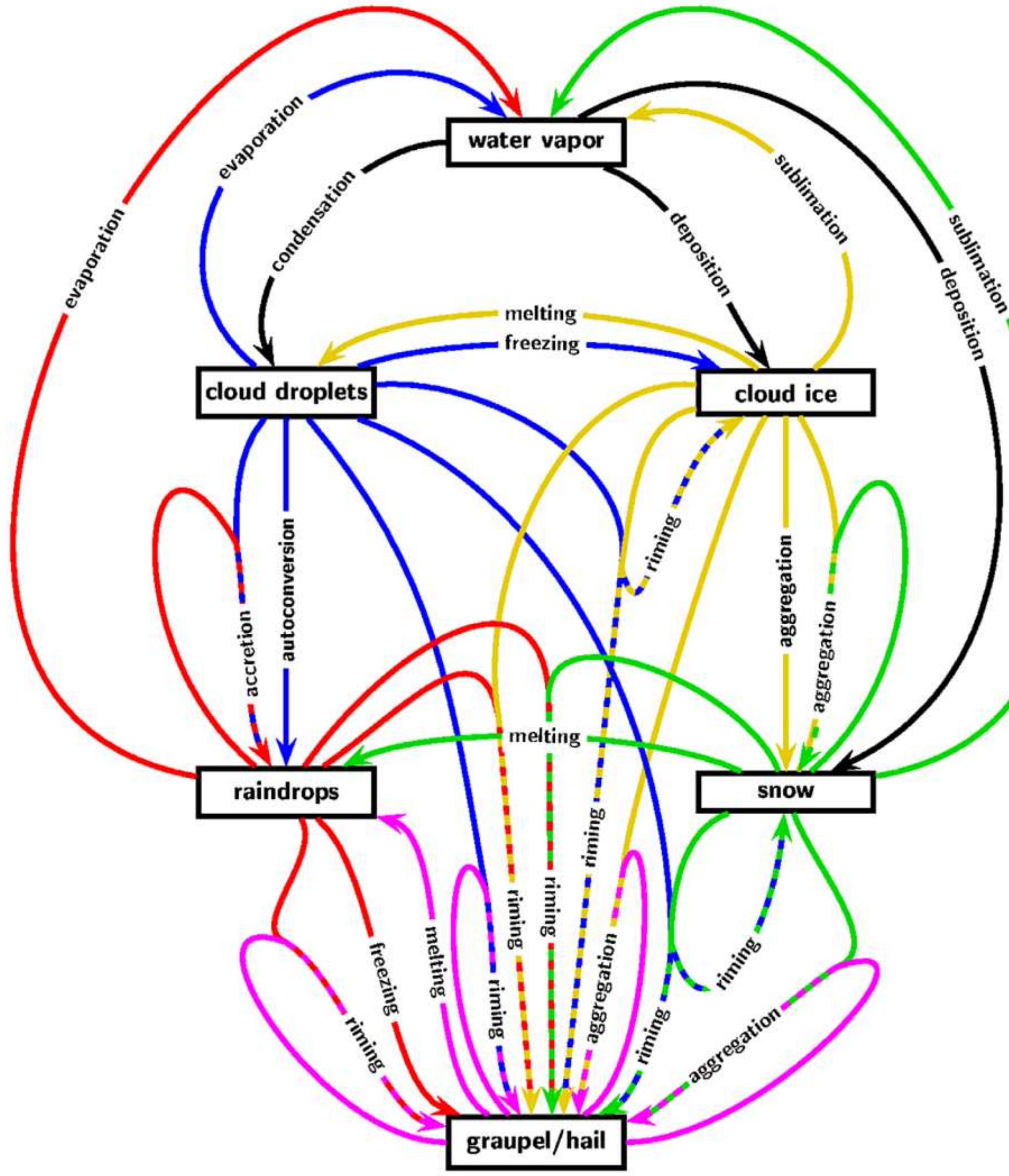

Figure 1.2: Atmospheric main water species and their interactions (Guichard and Couvreux, 2017).

as nuclei (e.g. Kärcher, 2002). However, cloud formation does not only depend on aerosol particles. Interactions between the water species themselves significantly influence cloud development as well. Particularly in MPC, a variety of different hydrometeor types may occur simultaneously. Their potential interactions with each other and with water vapour are schematically shown in Fig. 1.2. Those processes are to some extent quite complex, however, they play a key role in cloud development and thus in precipitation formation as well. In the mid-latitudes, for example, the Wegener-Bergeron-Findeisen process (Wegener, 1911; Bergeron, 1935; Findeisen, 1938) dominates cloud evolution (Boucher et al., 2013). This process allows ice crystals to grow at the expense of liquid water. However, the degree of glaciation of MPC still leads to significant uncertainties when it comes to climate predictions (e.g. Costa et al., 2017). In this regard as another example, Secondary Ice Production (SIP) cannot be quantitatively described yet (Korolev and Leisner, 2020). On the one hand, this might be due to the complexity of some processes as several water species may interact with each other. On the other hand, the observation of these mechanisms in nature and the reproducibility of corresponding laboratory experiments can be challenging (Korolev and Leisner, 2020). Typical SIP mechanisms are schematically shown in Fig. 1.3.

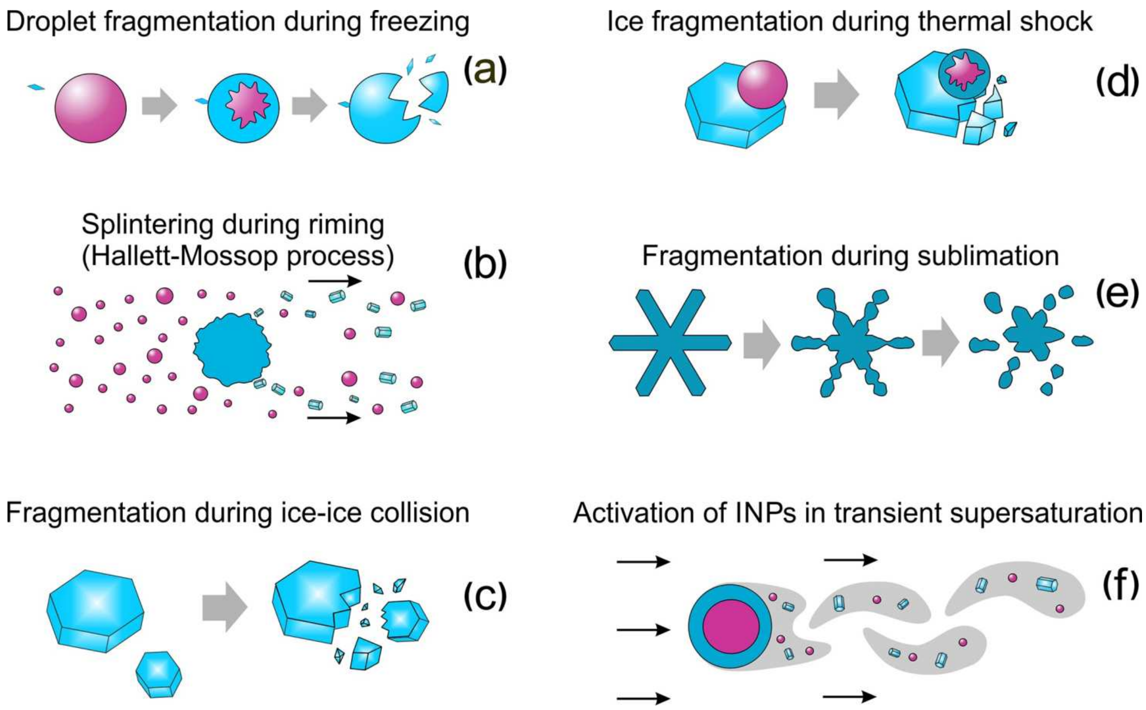

Figure 1.3: Typical Secondary Ice Production mechanisms. Blue indicates ice phase, red indicates supercooled liquid water (Korolev and Leisner, 2020).

For the investigation of cloud processes, the shape of ice crystals may provide important indications. When pristine ice crystals are growing, the resulting shape depends on the temperature and the supersaturation of the ambient air with respect to ice (e.g. Bailey and Hallett, 2009). Figure 1.4 provides the morphology of ice crystals under different ambient conditions. At low supercooling down to -3°C, ice crystals grow as plates or stellar dendrites. If temperatures are around -8°C to -10°C, crystals assume the shape of columns or needles. At even lower temperatures and larger supersaturation, the shapes become more complex. Therefore, the shape of ice crystals as an important quantity for the investigation of cloud microphysical processes needs to be detected.

One way to measure properties of ice crystals in the atmosphere and atmospheric conditions in general, including cloud properties, is offered by remote sensing. Atmospheric molecules and particles interact with electromagnetic radiation, depending on the ratio of the wavelength and the molecule or particle size. It can be distinguished between two types of remote sensing instruments that have different advantages. On the one hand, cloud radars are suitable for observing precipitation and clouds containing ice particles. Aerosol particles and liquid-water cloud droplets, on the other hand, can be better observed with lidar. Single instruments usually only measure one or a few specific parameters. Therefore, a synergy of remote sensing instruments is often necessary to investigate the current atmospheric conditions or detect atmospheric processes more accurately. Below, four methods of remote-sensing-based ice particle investigations are presented.

Bühl et al. (2016) evaluated a multi-annual combined radar and lidar dataset with a focus on MPC to relate cloud microphysical parameters such as integrated water content, liquid water content, linear depolarisation ratio, or cloud lifetime to thermodynamics. In the study, the ice mass flux at the cloud base was determined by means of ice water content and Doppler velocity. For different cloud top temperatures, the efficiency of heterogeneous ice formation and how it impacts the cloud lifetime was investigated. The authors found that most of the ice crystals precipitating from clouds with geometrical thickness of less

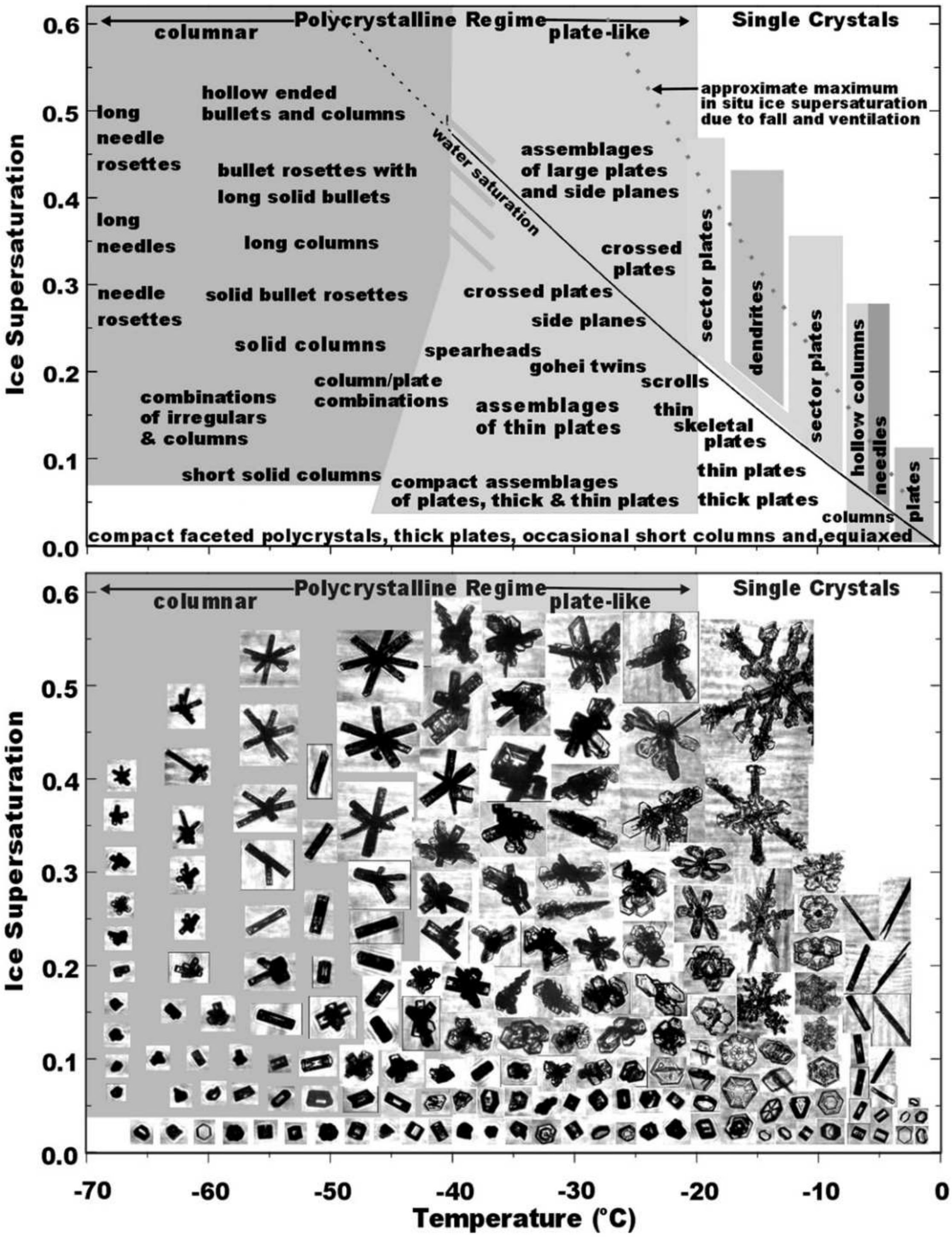

Figure 1.4: Ice crystal morphology in text (top) and picture version (bottom) observed during several laboratory experiments and field studies (Bailey and Hallett, 2009).

than 350 m are pristine. Another conclusion is that statistics of cloud observations are key to better understand the relation between cloud properties and thermodynamics. Radenz et al. (2021) conducted a similar study to compare clouds of the southern and northern mid-latitudes. Moreover, the impact of orographic waves on cloud microphysics could be considered separately in this study. However, Bühl et al. (2016) and Radenz et al. (2021) investigated only stratiform clouds and neglected the presence of multiple hydrometeor populations.

Radenz et al. (2019) described a novel approach for the retrieval of the number of different particle species from zenith-pointing radar Doppler spectra, which they refer to as peakTree. In a first step, separate peaks in the Doppler spectrum of radar measurements are found by splitting each spectrum at the local minima (Fig. 1.5). The resulting number of nodes for each spectrum provides information on the number of different particle types. Due to their different fall velocities, different particle types cause multiple peaks in the Doppler spectrum. By categorising and interpreting the measured peaks, certain categories of hydrometeors can be further analysed separately. Figure 1.6 shows an example case study which was acquired near the Faroe Islands on 2 February 2014. Here, the peakTree analysis allowed the detection of two liquid layers that are not visible in the radar reflectivity measurements. However, the detailed investigation of cloud microphysical processes requires further information about the hydrometeors involved.

Bühl et al. (2019) presented a method for the derivation of the ice crystal number concentration (ICNC) from combined remote sensing. Figure 1.7 schematically shows the general principle of this procedure. Again, the radar reflectivity is measured by cloud radar. Furthermore, the terminal fall velocity is determined by a radar wind profiler or by the combination of cloud radar and Doppler lidar. Ideally, the optical extinction coefficient derived by lidar is also taken into account for the retrieval. Subsequently, a size distribution of ice crystals needs to be found that would lead to a similar radar Doppler spectrum and lidar optical extinction like the measured one. For this purpose, a particle shape is presumed and the corresponding ICNC and fall velocity spectrum are determined. However, similar Doppler spectra can be simulated with significantly different size distributions for differently shaped particles as shown in Fig. 1.7.

Myagkov et al. (2016) described an approach to derive ice crystal shapes by polarimetric cloud radar observations. Via Range-Height Indicator (RHI) scans the differential reflectivity and the correlation coefficient are determined for radar antenna elevation an-

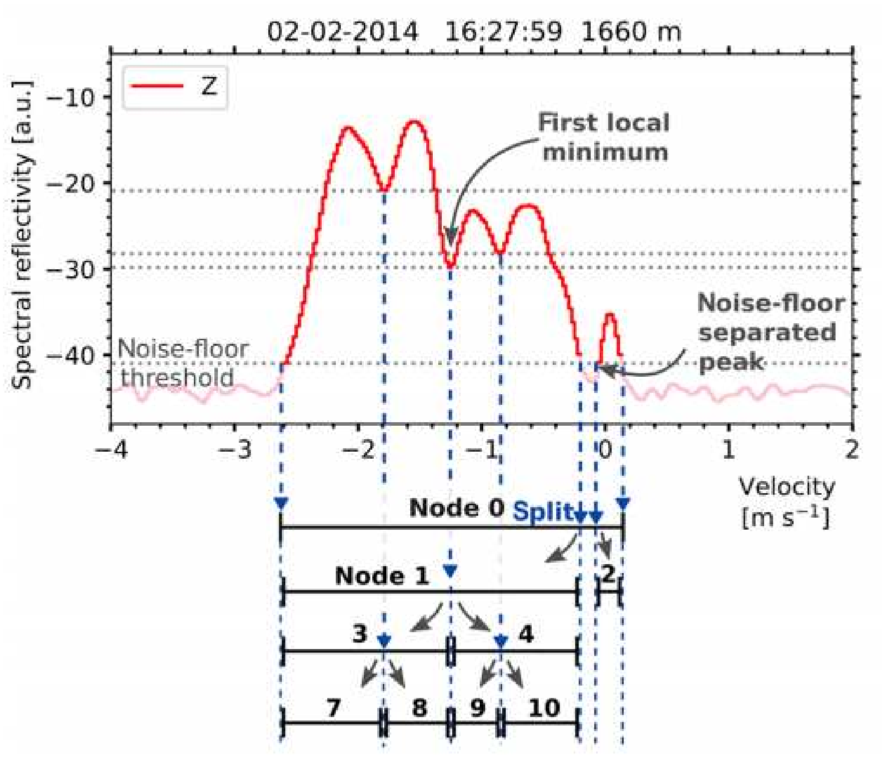

Figure 1.5: Doppler spectrum of a vertically pointing Ka-band zenith 35 GHz cloud radar (KAZR) and corresponding nodes. Faroe Islands, 2 February 2014 (Radenz et al., 2019).

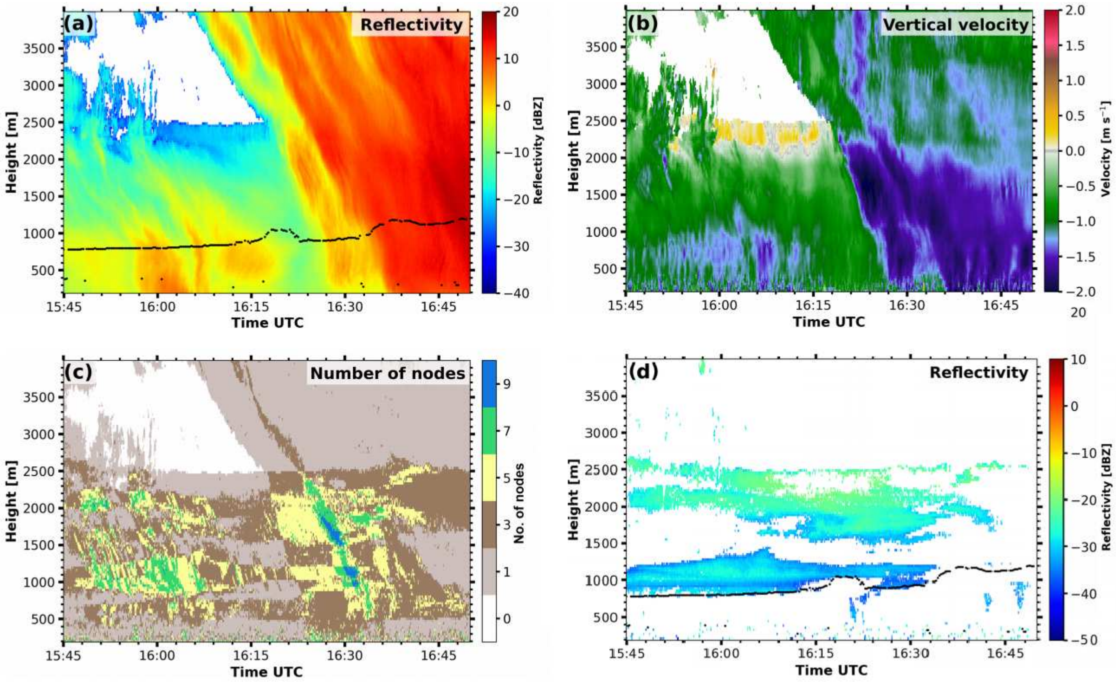

Figure 1.6: Time-height cross sections of KAZR (a) reflectivity and cloud-base height detected by lidar (black dots), (b) mean vertical velocity, (c) number of nodes from peakTree, and (d) reflectivity for liquid water nodes only. Faroe Islands, 2 February 2014. Adapted from Radenz et al. (2019).

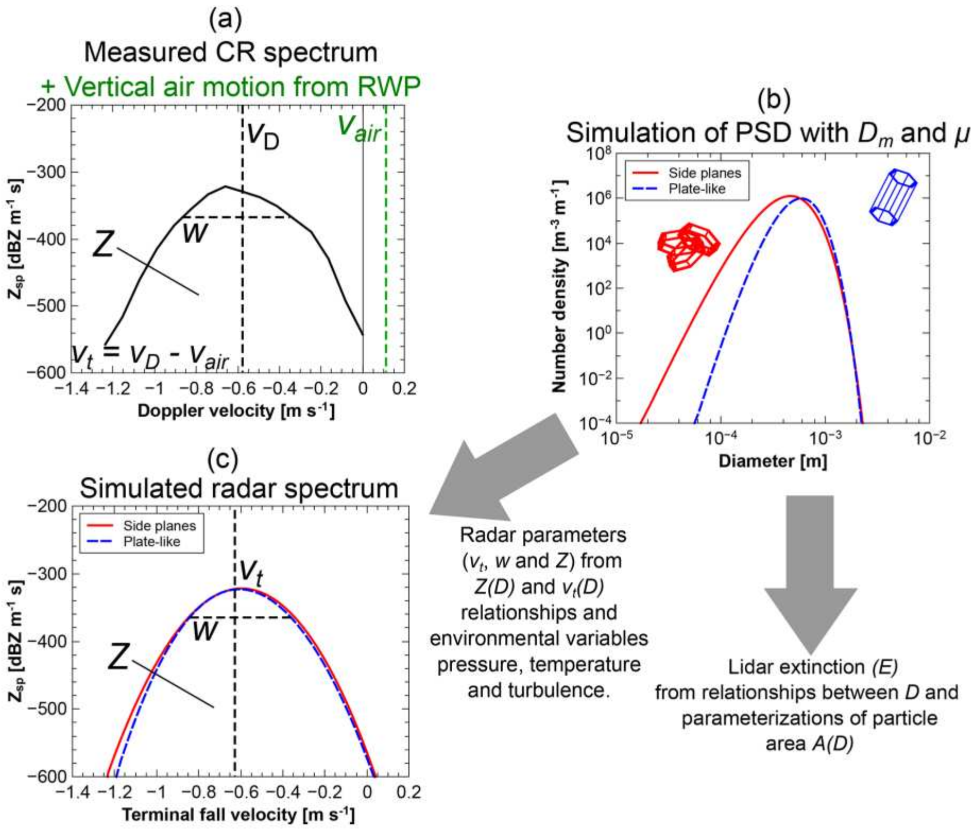

Figure 1.7: Schematical overview of the ICNC retrieval presented by Bühl et al. (2019) with (a) an example cloud radar spectrum measured at Lindenberg on 11 June 2015 at 19:00 UTC, (b) simulated particle size distributions for two different particle shapes, and (c) the cloud radar spectra corresponding to (b) (Bühl et al., 2019).

gles between 30° and 150°, while the antenna azimuth direction is hold constant. From the two observables, the polarizability ratio is estimated, which depends on the geometrical axis ratio and the apparent particle density and thus represents the morphology of ice particles. Subsequently, the observations were compared with experimental results from free-fall cloud chamber measurements. According to Myagkov et al. (2016), the good agreement of the polarizability ratios for ice crystals formed at certain temperatures derived from cloud radar and laboratory measurements (Fig. 1.8) indirectly evaluates this retrieval method. Furthermore, the results are in good agreement with the ice crystal habit diagram shown in Fig. 1.4.

The four methods presented above reveal that atmospheric ice crystals can already be examined well with remote sensing. However, for a direct evaluation of those retrievals, in-situ observations of single hydrometeors conducted simultaneously to remote sensing measurements are essential. Moreover, such in-situ observations can help to find connections between precipitation properties on the ground and the structure of cloud systems to better understand intermediate processes. This is the main motivation for this master's thesis focusing on the two-dimensional video disdrometer (2DVD) as a potential instrument which might provide such in-situ measurements. For this purpose, a 2DVD system was recently acquired by Leibniz Institute for Tropospheric Research (TROPOS). This 2DVD was operated during a measurement campaign in Switzerland, where data for this master's thesis were collected. The campaign and operated instruments are presented in Chapter 2. Particular attention is paid to the 2DVD including a detailed explanation of the measurement principle and data processing chain, the calibration procedure, and former 2DVD related research. For the characterisation of the 2DVD as one of the main objectives of this thesis, a variety of parameters describing precipitation and single particles can be derived from the measurements. Those parameters are presented in Chapter 3. The presumably most important intention of this work is the 2DVD evaluation. The overarching

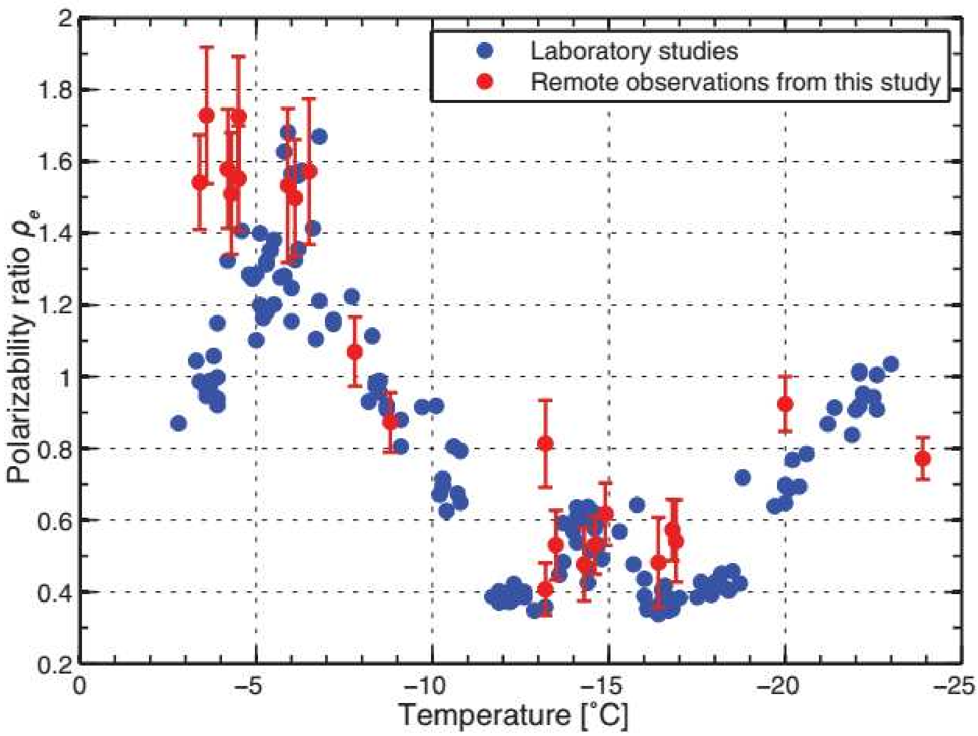

Figure 1.8: Relations of polarizability ratio and temperature for ice crystals. Blue circles indicate results of laboratory studies using a free-fall chamber. Red circles show results retrieved from remote sensing observations with hybrid Mira-35 with bars representing ±1 standard deviation (Myagkov et al., 2016).

question is whether and, if so, how well the instrument can distinguish different particle types. Co-located measurements with a holographic in-situ sonde, conducted from 16 to 18 January 2023 during the campaign, may offer valuable clues to that issue. Furthermore, educated-eye protocols about shapes of precipitating ice crystals were created during several snowfall events. Moreover, the 2DVD measurements can be evaluated against other precipitation sensors by comparing precipitation rates, for example. Results with regard to the 2DVD evaluation and the observation of different particle types are presented in Chapter 4. A third objective of the master's thesis consists in the evaluation of the possible contribution of the 2DVD to the detection of cloud microphysical processes. This goal is partly dependent on the 2DVD evaluation, because the precipitation properties on ground need to be detected as precisely as possible for the evaluation of remote-sensing signatures of clouds, especially with regard to the retrievals presented above. During the 2DVD data collection, cloud seeding experiments were conducted and seeding signatures could be obtained by the instrument. Results of those experiments are presented in Sect. 4.3.

Chapter 2

Measurement campaign and operating instruments

2.1 Cloudlab and PolarCAP

The data for the master's thesis were collected during a measurement campaign at Rapier-Platz near Eriswil, Switzerland (47.0705°N, 7.8729°E, 921 m above sea level) which took place from December 2022 to March 2023. Rapier-Platz is located in the Swiss middleland between the Jura and the Alps. Typical meteorological conditions during wintertime are below-zero temperatures and steady winds from north east called 'Bise', often accompanied by stratus clouds which are suitable as natural cloud laboratory. The observations were conducted within the framework of the two collaborating research projects Cloudlab of ETH Zürich and PolarCAP (Polarimetric Radar Signatures of Ice Formation Pathways from Controlled Aerosol Perturbations) of Leibniz Institute for Tropospheric Research (TROPOS). Cloudlab (Henneberger et al., 2023) in general aims at a better understanding of cloud physics, the investigation of stratus formation and dissipation, and the validation and improvement of the cloud microphysics scheme of the icosahedric non-hydrostatic (ICON) weather forecast model (Zängl et al., 2014; Omanovic et al., 2024). In order to achieve these goals, a variety of field measurements, laboratory experiments and modelling studies are planned. More specifically, seeding experiments in mixed-phase stratus clouds, accompanied by remote sensing and in-situ observations should provide new insights in cloud microphysical processes. Those observations are complemented by extensive, mainly remote-sensing-based measurements with the Leipzig Aerosol and Cloud Remote Observations System (LACROS) (Bühl et al., 2013; Myagkov et al., 2016; Radenz et al., 2021; Teisseire et al., 2024) in the frame of PolarCAP. Besides the support of Cloudlab with field observations and expertise, the goals of PolarCAP are the investigation of MPC development as well as the evaluation of MPC retrievals based on remote sensing. For the characterisation of MPC, cloud-Doppler radar and (Doppler) lidar techniques are applied and Cloudlab in-situ measurements and seeding experiments are used. Moreover, simulations with numerical cloud-resolving models are conducted. Due to the variety of instruments, the measurement location and its duration, the presented field campaign offers a rare opportunity to compare precipitation measurements of several remote sensing and in-situ instruments and in particular to evaluate the performance of the 2DVD under different conditions.

2.2 Instrument overview

Many of the instruments at the measurement site are of relevance for the intentions of this thesis. Figure 2.1 shows the setup of the platform LACROS during the campaign. However, the main focus will be on the 2DVD (see Sect. 2.3). In addition, the holographic

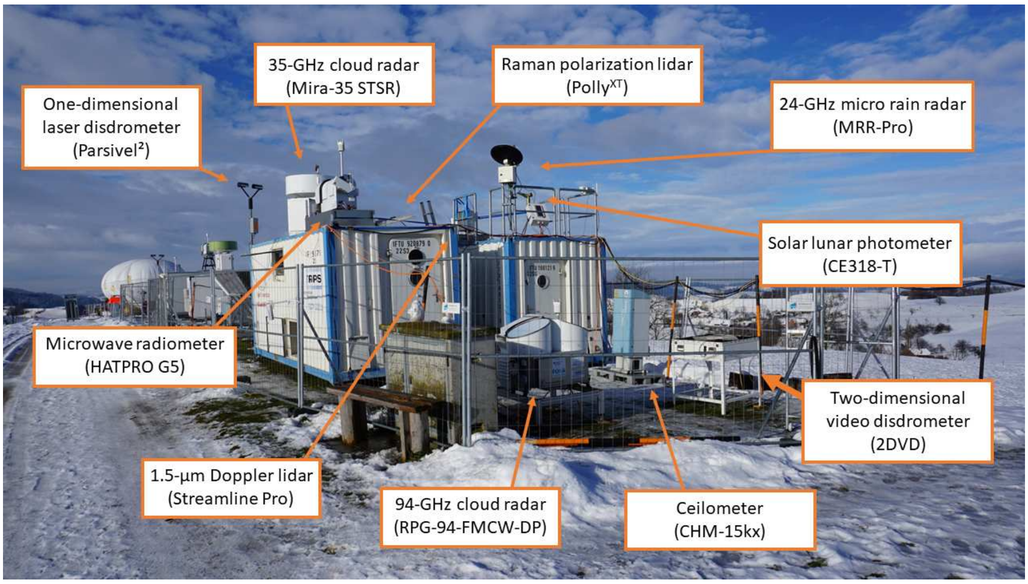

Figure 2.1: Setup of LACROS at the measurement site including instrument designations. Further instruments of ETH Zürich and METEK GmbH can be seen on the left in the background.

in-situ sonde HOLIMO of ETH Zürich (Sect. 2.4) is of particular interest when it comes to the evaluation of the 2DVD. Furthermore, measurements of several other instruments belonging to LACROS could be analysed in combination with 2DVD data. This includes, firstly, a number of active remote sensing instruments such as a 35-GHz and a 94-GHz cloud radar, a 24-GHz micro rain radar, a 1.5-µm Doppler lidar, a ceilometer and a Raman polarisation lidar as well as a passive measuring microwave radiometer and a solar lunar photometer. Many of those instruments can be considered when it comes to the comparison of precipitation rates, for example. Secondly, further in-situ sensors such as a one-dimensional laser disdrometer and Vaisala weather stations allow further direct comparisons of precipitation observations. An overview about all LACROS instruments is given in Tbl. 2.1.

Table 2.1: Instrumentation of the mobile platform LACROS. More details on the instruments are given in Radenz et al. (2021).

Instrument	Type	Atmospheric parameters	Resolution
Polly^{XT}	Multiwavelength Raman polarisation lidar, pointed 5° off-zenith	Particle backscatter and extinction coefficient; linear depolarisation ratio; water vapour mixing ratio	7.5 m; 30 s
Streamline Pro	1.5-µm Doppler lidar	vertical wind speed and direction profiles, particle backscatter profiles	48 m
Mira-35	35-GHz scanning cloud radar	Vertical structure, boundaries and vertical-velocity dynamics of clouds and precipitation; contributes to cloud liquid and ice water profiles	30 m; 3 s
RPG94_LACROS	94-GHz vertically pointing cloud radar	Vertical structure, boundaries and vertical-velocity dynamics of clouds and precipitation; profiles of cloud liquid water and ice water content	15 – 30 m; 1 – 30 s
MRR-Pro	24-GHz rain radar	Vertical profiles of drop size distribution, rain rate and liquid water content	10 m; 1 s
HATPRO G5	14-channel microwave radiometer	Estimated profiles of temperature and humidity; integrated water vapor and liquid water path	100 – 1000 m; 1 s
Solar lunar photometer	CE318-T	Aerosol Optical Depth particle volume size distributions	$< 0.1\%$
Ceilometer	CHM-15kx	cloud bottom height Particle backscatter	± 5 m
Weather station	Vaisala WXT536	Atmospheric pressure, temperature, relative humidity, surface wind, rain rate	± 3% at 10 m s^{-1} ± 1 hPa
Parsivel²	One-dimensional laser disdrometer	Precipitation rate, type, size distribution, radar reflectivity	0.5 – 25 mm (solid) 0.2 – 20 m s^{-1}
2DVD	Two-dimensional video disdrometer	Precipitation rate, size distribution, fall velocity, particle imaging	see Tbl. 2.2

2.3 Two-dimensional video disdrometer (2DVD)

The 2DVD is a ground-based precipitation gauge which detects single precipitation particles within a certain measuring area. Originally designed to measure rain drop size distributions, the first instruments of this kind operated since 1996 (Schönhuber et al., 2007). The investigation of solid hydrometeors with such devices has rather been subject of research in recent years, as will be pointed out in Sect. 2.3.3. The instrument which was operated during PolarCAP was developed by Joanneum Research, Graz, Austria. Table 2.2 shows the specifications of the 2DVD. At this point it should be mentioned that the horizontal wind measured by the weather station, which was connected to the HATPRO G5 on the container roof, did not exceed $10\,\mathrm{m\,s^{-1}}$ during the conduction of any 2DVD measurements presented in this work, unless otherwise stated.

2.3.1 Measurement principle and data processing

The schematic equipment configuration of the 2DVD is shown in Fig. 2.3. Two high-power lamps (halogen or LED) each continuously emit light to a mirror which reflects it towards a Fresnel lens. There, the light is diverged and travels through a slit plate so that a light sheet is created from each halogen lamp. Those two light sheets are aligned orthogonally against each other in the horizontal plane and have a height difference of around 6 mm. The area where the two sheets lie on top of each other is the so-called virtual measuring area and of approximately 10 cm x 10 cm in size. After travelling through another slit plate, the light is then reflected by another mirror to the respective line camera.

The instrument is designed advantageous for further reasons. The virtual measuring area is much smaller than the opening of the housing (25 cm x 25 cm) so that possible splashes of droplets hitting the housing would not be processed. Moreover, the lid is heated which avoids that snow accumulates on the instrument and gets blown into the virtual measuring area by wind gusts.

If a hydrometeor is falling through the virtual measuring area, its shape automatically gets reconstructed. In a first step, this is done for the video signal of each camera separately, as is schematically shown in Fig. 2.4. The photodetectors (pixels) of the line camera generate an electronic signal at incident light. This signal is continuously compared against a threshold level. If the measured value is below this threshold, the corresponding pixel is recognised as shaded. By assembling the shaded pixels of consecutive time steps, a one-dimensional particle shape is finally reconstructed.

In a second step, a matching algorithm is applied to merge the information for the same particle from both cameras. For this purpose, several criteria that a pair of images needs to fulfil are considered. A time period is defined in which a particle needs to reach the lower light plane after it entered the upper light plane of the instrument. This time

Table 2.2: 2DVD specifications. Values marked with a * account for particle velocities $<10\,\mathrm{ms^{-1}}$.

quantity	value
uncertainty of	
vertical resolution	$< 0.17\,\mathrm{mm}$*
horizontal resolution	$< 0.17\,\mathrm{mm}$*
vertical velocity	$< 4\%$*
camera frequency	55.2 kHz
virtual measuring area	$\sim 100\,\mathrm{cm^2}$

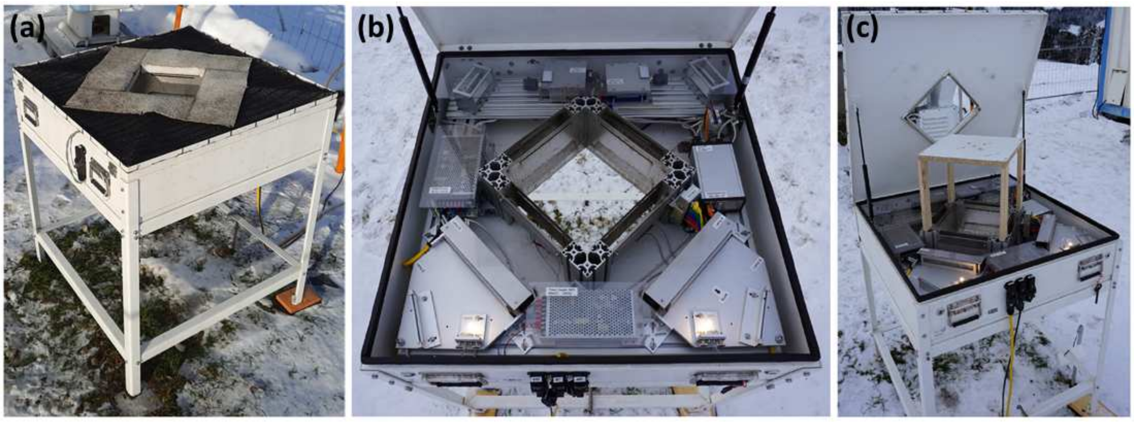

Figure 2.2: The 2DVD at the measurement site (a) in operating modus, (b) with open lid, and (c) during the calibration with calibration pattern.

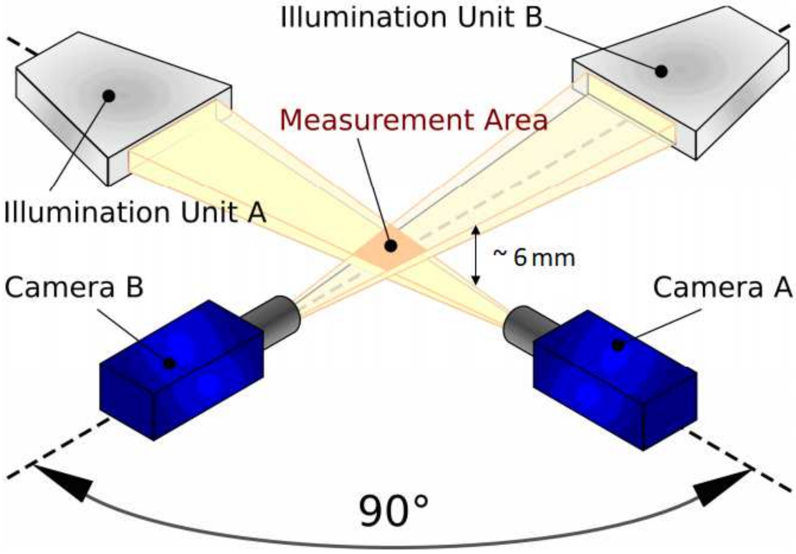

Figure 2.3: Measurement principle of the 2DVD. The light sheets are aligned orthogonally against each other with a vertical distance of around 6 mm. The measuring area is around 10 cm x 10 cm in size (adapted from Schönhuber et al., 2016).

frame should be adapted to the relationship between particle size and fall velocity. In case of liquid droplets, this relation is well-known (e.g. Atlas et al., 1973). For solid and mixed-phase hydrometeors, terminal velocities of particles of the same size can vary much more, depending on the particle type, shape, and, if applicable, the degree of riming (Locatelli and Hobbs, 1974; Barthazy and Schefold, 2006). Thus, the time period to fall from the upper to the lower light plane should be set more broad in case of solid or mixed-phase precipitation. Moreover, droplets show regular symmetries which can be assumed by the matching algorithm. Solid particles, on the other hand, may appear with much more complex shapes. Matching algorithms for solid or mixed-phase precipitation have been continuously developed during the last years (see Sect. 2.3.3). For those reasons, the 2DVDs manufacturer provides two different matching algorithms for liquid and solid or mixed-phase precipitation, herein referred to as hyd-algorithm and sno-algorithm, respectively. After the application of such an algorithm, single hydrometeors are identified and information about their properties are retrieved (see section Sect. 3.1). Particles that are only seen in one camera or whose information of both cameras could not be merged are not further processed.

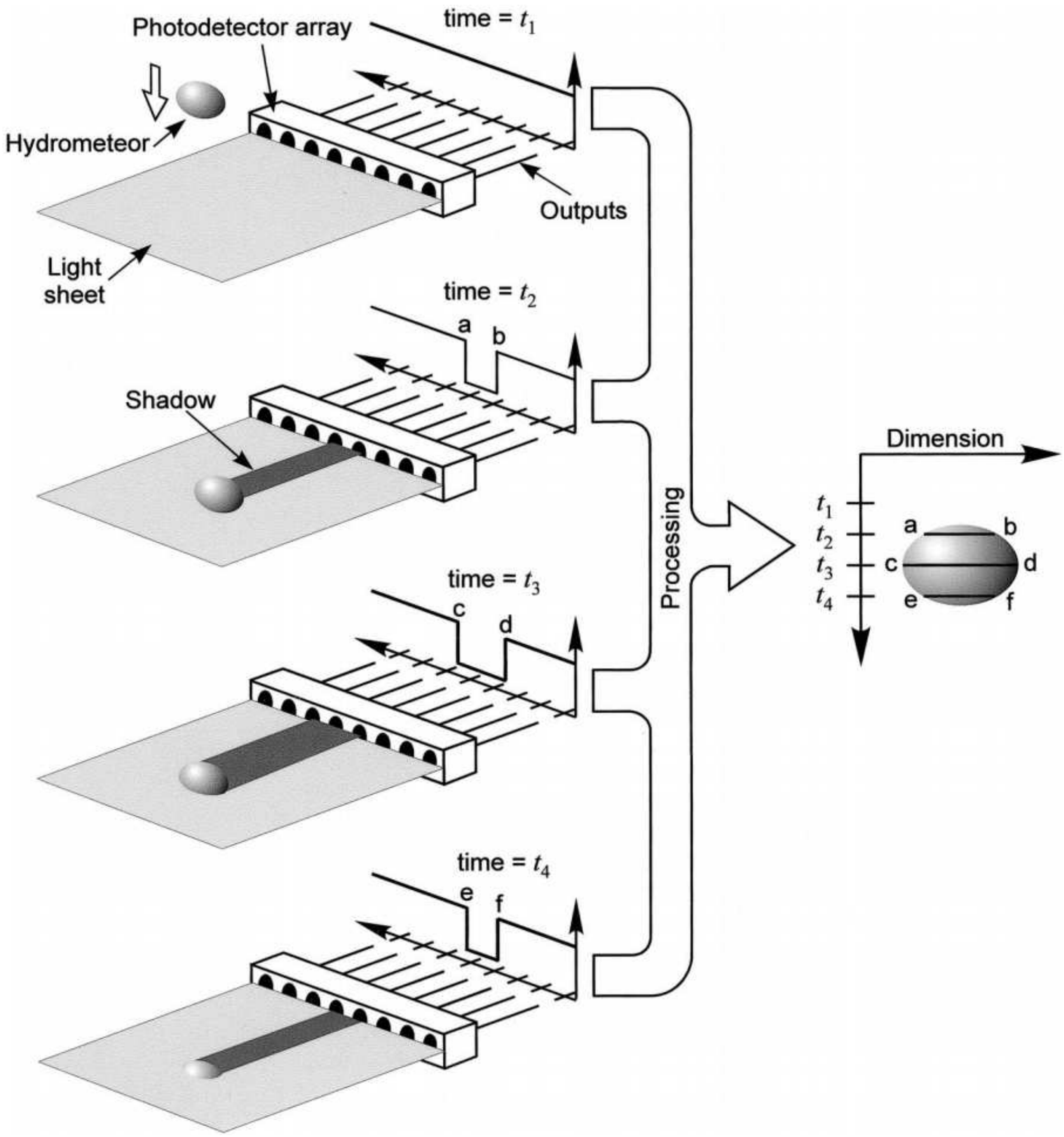

Figure 2.4: Reconstruction of a hydrometeor shape from camera perspective. When the hydrometeor is falling through the virtual measuring area during different time steps, the illumination of single pixels of the line camera is interrupted allowing the reconstruction of the particle shape (Kruger and Krajewski, 2002).

To calculate the correct size of each particle, the actual pixel width p has to be known. As p depends on the location in the virtual measuring area, an individual pixel width accounts for every single particle:

$$p = p(x, y) \cdot f_{corr} \qquad (mm) \tag{2.1}$$

with $p(x, y)$ as pixel width seen from the location (x,y) in the light plane and f_{corr} as correction factor dependent on the particle size and provided by the manufacturer. The pixel height on the other hand depends on the vertical velocity of the particle with larger velocities leading to larger pixel heights. With those pixel information, hydrometeors can be displayed visually and properties of single particles are calculated by programs of the 2DVD manufacturer (see Chapter 3). For the purposes of hydrometeor display and further precipitation analysis (see Chapter 4), own programs were written. The data processing chain up to 2DVD level0 data as netCDF files is schematically shown in App. A.

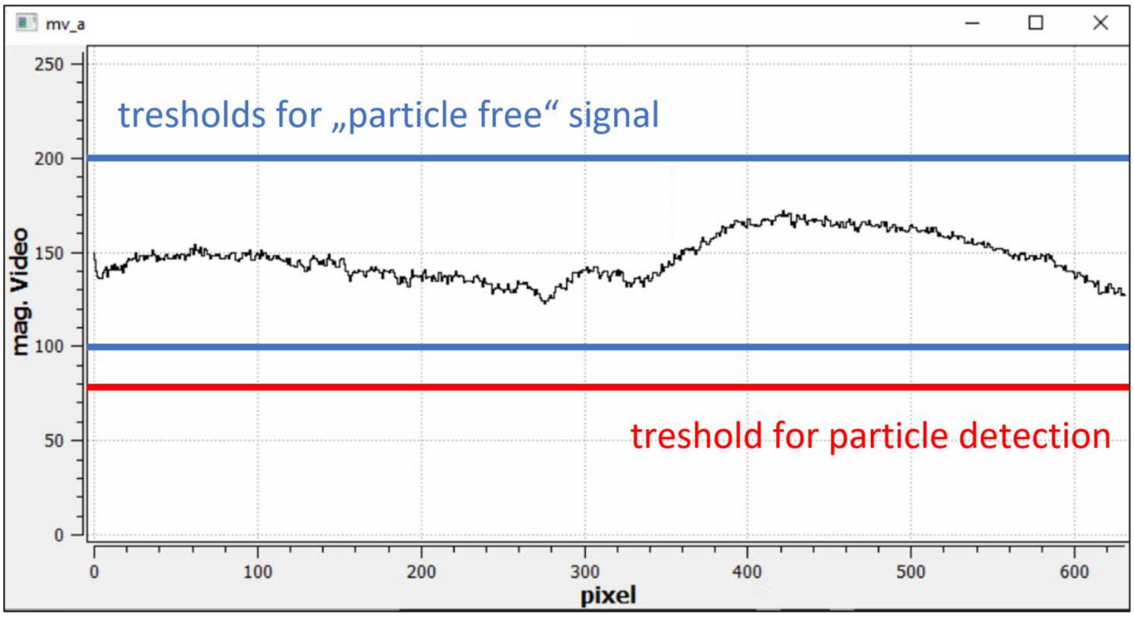

Figure 2.5: Calibration step 1: Video level adjustment for one camera.

2.3.2 Calibration procedure

In order to calibrate the 2DVD, the following three main steps have to be taken. In a first step, the video levels of the live signals need to be adjusted. The signal of each pixel must be between an upper and a lower threshold (Fig. 2.5). The signal adjustment is done by aligning the optical elements of the 2DVD such as the lamps and mirrors. Once, the signals are within the right intensity range, the distance of the two light planes needs to be measured precisely in a second step. For this purpose, some steel spheres with a diameter of 10 mm are thrown through each hole of a calibration pattern (Fig. 2.2c). With this measurement as an input, a program then calculates the plane distance for every corner of the virtual measuring area. The resulting values need to be adjusted in a configuration file before further measurements are taken. During this step, no hydrometeors must enter the measuring area. Eventually, some correction factors included in the configuration file need to be checked. Therefore, a set of calibration steel spheres with diameters ranging from 0.5 mm to 10 mm are part of the 2DVD equipment. Ideally, more than 100 spheres of each diameter must be thrown through the virtual measuring area. Subsequently, this measurement can be evaluated by having a look at the detected diameters of the spheres. If the values are in good agreement with the given diameters of the spheres, the calibration is finished. If the agreement is poor over a series of repetitions of the calibration, the manufacturer of the 2DVD, Joanneum Research, can provide correction factors adapted to the taken measurements.

2.3.3 Former 2DVD research

The first 2DVD of Joanneum Research was delivered in 1996 and the instrument technology has been developed continuously since then (Schönhuber et al., 2007). The instrument design was adapted over time to a number of challenges that were faced during measurements such as performance under windy conditions or strong temperature variations. Three generations of 2DVDs with different specifications have been manufactured by Joanneum Research so far. Hence, one has to pay attention to the instrument version when it comes to publications about 2DVD related research.

Nešpor et al. (2000) indicated the disadvantageous design of an earlier 2DVD version, which led to measurement uncertainties of smaller droplets at higher wind speeds. The wind field around and inside this 2DVD version was simulated and discussed by Habib and Krajewski (2001). An anomaly in up-to-date-generation 2DVD data caused either by hanging droplets at the upper rim of a metal slit or by small droplets reaching a mirror between the camera and the illumination unit was discovered by Larsen and Schönhuber (2018). Larsen and Blouin (2020) analysed uncertainties in the derived effective measuring area (see Chapter 3) and developed a corresponding refinement algorithm. The instrument was originally designed to derive drop size distributions of rain events, but snowfall measurements became an important part of 2DVD research as well. In this context, several studies were conducted to develop a suitable matching algorithm (see Sect. 2.3.1) for solid or mixed-phase precipitation (Hanesch, 1999; Huang et al., 2010; Grazioli et al., 2014; Bernauer et al., 2015).

Studies about raindrop properties such as raindrop shapes (Tokay et al., 2000), droplet axis ratios (Thurai and Bringi, 2005), or canting angle distributions (Huang et al., 2008) were conducted. A 3D droplet reconstruction method developed by Schönhuber et al. (2016) is used, for example, by Zheng et al. (2023) to revisit droplet axis ratios. Raindrop fall velocities in particular were investigated under different wind conditions in Colorado and Alabama (Bringi et al., 2018) and during different monsoon seasons in India (Das et al., 2020). Moreover, raindrops of fall velocities larger than theoretically expected, so-called superterminal raindrops, were examined by Leijnse and Uijlenhoet (2010) and Larsen et al. (2014). (Gatlin et al., 2015) analysed a high number of data sets of 2DVD measurements to descry large raindrops. The largest detected example exhibited a diameter of 9.7 mm and was detected in a hail-producing thunderstorm in northern Oklahoma.

The investigation of precipitation properties made up a large part of research with 2DVDs. Studies focusing on rainfall properties were conducted in Colorado (Bringi and Hubbert, 1997), Austria and Papua New Guinea (Randeu et al., 2002), the Netherlands (Leijnse et al., 2010b) or Sumatra (Marzuki et al., 2013), for example. Spatial and temporal precipitation distributions were examined by Larsen et al. (2005) and Gires et al. (2015). However, the majority of 2DVD related rainfall research refers to measurements of the Drop Size Distribution (DSD). DSDs were ascertained in the southwestern Amazon basin (Tokay et al., 2002) and characterised during Typhoons (Wen et al., 2018; Feng et al., 2021) and different seasons in China (Wen et al., 2019; Luo et al., 2021). Marzuki et al. (2010) investigated the impact of the bin size to the DSD. Testik and Pei (2017) found a wind-dependency of the DSD due to collisional breakup processes at higher wind speeds, leading to increasing amounts of small drops and decreasing amounts of large drops. DSD shapes by means of parameters of the uncorrelated raindrop mass spectrum are described by Williams et al. (2014). Thurai et al. (2014) examined the correlation of DSD parameters measured by co-located 2DVDs. Uijlenhoet et al. (2006) investigated the shape of measured DSDs and estimated bulk rainfall variables such as liquid water content, rain rate, and radar reflectivity from it. DSD measurements are the subject of numerous further studies. Often, they are compared with measurements of other precipitation observing instruments or they are used in combination with radar data. Both types of studies are mentioned later in this subsection.

Due to the ability of deriving ice crystal shapes from the camera recordings, studies on mixed-phase and solid precipitation took up a significant part of recent 2DVD research. Brandes et al. (2007) examined statistical properties of particle size distributions of winter storms in Colorado and found an underestimation of small particles, especially at windy conditions. Moreover, a relation of particle bulk density and median volume diameter was found by Brandes et al. (2007), but also in further studies (e.g., Zhang et al., 2021). Increasing fall speeds of snow aggregates with increasing temperature were measured by Brandes et al. (2008). Bernauer et al. (2015) conducted reproducible experiments with irregularly shaped Styrofoam particles and found self-consistent behaviour of the 2DVD. The multifractality of ice crystals was analysed by Raupach et al. (2017). Moreover, several studies were conducted in which solid precipitation was characterised at certain locations, for example, by Wen et al. (2017) in China. During most 2DVD research about solid particles, other instruments such as different types of disdrometers or radar instruments were used simultaneously. Those studies are mentioned further below.

Especially during the last decade, classification of hydrometeors detected by 2DVD gained research interest. The classifications are partly based on already existing algorithms, but also new methods were developed. Grazioli et al. (2014) and Gavrilov et al. (2015) classified solid hydrometeors by means of a Support Vector Machine (Boser et al., 1992). Lee et al. (2015) categorised solid hydrometeors based on investigated relationships between particle fall velocity and diameter. Bernauer et al. (2016) developed a new classification algorithm for solid precipitation events which subdivides one-minute intervals into dominating ice crystal type and dominating degree of riming. Besides research about particle classification, investigations into the accuracy and reliability of 2DVD in distinguishing between convective and stratiform precipitation were made by Bukovčić et al. (2015) and Wen et al. (2017).

The 2DVD was often compared with other in-situ precipitation measurement instruments, especially with the OTT Hydromet particle size and velocity (Parsivel) disdrometer (Löffler-Mang and Joss, 2000) or its second generation (Parsivel^2). From many comparative studies that were undertaken (Krajewski et al., 2006; Battaglia et al., 2010; Tokay et al., 2013; Raupach and Berne, 2015; Park et al., 2017; Liu et al., 2019), one can conclude, that measured DSDs in general agree well between the Parsivel and the 2DVD. However, particularly at higher rain rates, the Parsivel seems to overestimate the amount of large drops. Battaglia et al. (2010) additionally reported an overestimation of small snowflakes, while Park et al. (2017) discovered an underestimation of small droplets compared to the 2DVD results. Co-located precipitation measurements with 2DVD and different rain gauges showed, that rain duration and rain rate measurements can significantly differ between those instruments and may depend, for example, on wind speed and precipitation type (Liu et al., 2013, 2019; Cauteruccio et al., 2023).

Before the appearance of the 2DVD, the Joss-Waldvogel disdrometer (JWD, Joss and Waldvogel (1967)) was seen as the standard instrument for surface precipitation measurements for several decades (Williams et al., 2000), for which reason many studies performed simultaneous JWD and 2DVD observations. In general, both instruments show good agreement for DSD measurements (Williams et al., 2000; Tokay et al., 2001; Liu et al., 2013; Tokay et al., 2013; Chang et al., 2020). Chang et al. (2020) reports lower concentrations for small and large droplets measured by the JWD whose maximum detectable particle diameter is smaller than that for the 2DVD as well (Tokay et al., 2001). At rain rates larger than $20\,\mathrm{mm\,h^{-1}}$, Liu et al. (2013) recorded lower rain rates with the JWD than with the 2DVD.

Further studies compare some other instruments with the 2DVD. Krajewski et al. (2006) found good agreements of measured rain rates of the 2DVD and a dual-beam spectropluviometer (Hauser et al., 1984). According to Helms et al. (2022), the Precipitation Imaging Package (PIP, Pettersen et al. (2020)) and the Multi-Angle Snowflake Camera (MASC, Garrett et al. (2012)) are advantageous compared to the 2DVD when it comes to snowflake shape measurements. Thurai et al. (2017a) conducted measurements with a 2DVD and a Meteorological Particle Spectrometer (MPS, Baumgardner et al. (2002)) and revealed that the MPS delivers more accurate measurements of droplets smaller than 0.7 mm due to its 50-µm resolution. Co-located rain rate measurements with a 2DVD and a Present Weather Detector (Vaisala PWD22) produced rather similar results (Liu et al., 2013). The Precipitation Microphysical Characteristics Sensor (PMCS, Liu et al. (2014)) can detect small particles very well and is therefore suited for simultaneous measurements with the 2DVD, according to Liu et al. (2019). Chang et al. (2020) found that the precipitation occurrence sensor system (POSS, Sheppard (1990)) measures higher concentrations of small droplets (< 1 mm) than the 2DVD and detects big droplets better due to the high sampling volume. Caracciolo et al. (2006) compared measurements of a 2DVD and a bistatic Doppler rain-gauge disdrometer called Pludix (PLUviometro-DIsdrometro in X-band, 9.5 GHz, Prodi et al. (2000)) and concluded, that the Pludix performance is rain rate dependent. In a non-comparative study, Miriovsky et al. (2004) relied on the good agreement between different disdrometer types and investigated the small-scale spatial variability of radar reflectivity with four different instruments.

For precipitation measurements, the 2DVD is often combined with other remote sensing instruments. For example, observations of micro rain radar (MRR) and 2DVD do in general agree well, except for the detection of small droplets whose concentration is often larger in MRR observations (Diederich et al., 2004; Chang et al., 2020). Adirosi et al. (2020) found that radar reflectivities derived from both instruments do not differ more than around 2 dB. Nevertheless, actual rain rates showed between 28% and 36.7% difference, mainly depending on the precipitation type. Zhou et al. (2020) investigated vertical raindrop distributions and relationships between rain rate and radar reflectivity by means of co-located MRR and 2DVD measurements. By using a microwave radiometer (MWR), Kneifel et al. (2010) and Löhnert et al. (2011) investigated snow scattering by my means of co-located MWR and 2DVD measurements.

As the 2DVD can measure precipitation rates, DSDs, and particle shapes, the radar reflectivity Z and even polarimetric radar parameters can be retrieved from 2DVD observations (Schönhuber et al., 2000). This offers a wide range of opportunities to compare and evaluate 2DVD and polarimetric radar data. Numerous studies from the last three decades show, that such an instrument combination can be advantageous when it comes to the examination of precipitation properties, especially DSDs. For such purposes, radars with different frequency bands were used. In the S-Band regime (2–4 GHz), many comparative studies were conducted with regard to measured, derived, or modelled PSD or radar reflectivity (Ibrahim et al., 1998; Schuur et al., 2001; Bringi et al., 2003; Maeso et al., 2005; Brandes et al., 2004, 2006; Liu et al., 2018; Adirosi et al., 2020; Tao et al., 2020; Lee et al., 2023). Often, the 2DVD was used to determine the shape of the DSD and radar instruments measured polarimetric radar variables. The combination of both was then used to estimate precipitation rates or to characterise precipitation microphysics (Zhang et al., 2001, 2011; Brandes et al., 2003; Cao et al., 2008; Kim et al., 2020; Chen et al., 2021). Observations of particle shapes with the 2DVD were used in combination with radar measurements to estimate rainfall (Kim et al., 2016), to monitor liquid-ice phase transitions of winter precipitation (Bukovčić et al., 2017), to derive the visibility in aggregated snow (Bukovčić et al., 2021), or to estimate liquid fraction of wet snow (Suh et al., 2021). Measurements in the C-Band regime (4–8 GHz) were undertaken to compare radar and 2DVD performances (Schönhuber et al., 1997; Bringi et al., 2006), to estimate precipitation rates (Chen et al., 2021), and to investigate relations between DSD and drop shape (Chang et al., 2009) or between radar reflectivity and snow rate (Huang et al., 2010, 2015). By means of polarimetric X-Band (8–12 GHz) radar and 2DVD measurements, rainfall was estimated (Anagnostou et al., 2004; Leijnse et al., 2010a; Thurai et al., 2017b), DSDs were investigated (Schuur et al., 2001; Okazaki et al., 2023), and partial radar beam blockage was analysed (Shakti et al., 2013). Baquero et al. (2006) simulated X-Band polarimetric radar data from 2DVD measurements in Puerto Rico and Kalogiros et al. (2014) used the 2DVD as evaluation instrument for a rain-path attenuation correction algorithm for

X-Band radar observations. Nishikawa et al. (2016) compared relations between specific attenuation and radar reflectivity in the Ka-Band regime (24–40 GHz) for different ice crystal shapes which were determined by 2DVD measurements.

Data obtained by the 2DVD were also used to improve models for DSDs (Zhang et al., 2008; Cao and Zhang, 2009; Adirosi et al., 2016; Thurai and Bringi, 2018) or polarimetric radar variables for different frequency bands (Thurai et al., 2007). Wen et al. (2018) presents a model which retrieves the DSD from polarimetric variables and uses 2DVD measurements for the model evaluation.

2DVD observations are even used since over a decade in combination with satellite measurements. The Global Precipitation Measurement (GPM) mission by the National Aeronautics and Space Administration (NASA) includes spaceborne radar and radiometer measurements of precipitation (e.g. D'Adderio et al., 2018). For the ground validation of those data, a measurement infrastructure, which includes 2DVD instruments, has been developed (Petersen et al., 2010). This reflects the reliability of the instrument with regard to precipitation measurements.

The large number and variety of studies presented above proofs the versatility of the 2DVD. Research has shown, that the instrument is suitable for the observation of liquid and solid precipitation and that it can distinguish between different ice crystal shapes. For those reasons, the 2DVD is valuable for co-located measurements of precipitation with different instrument types.

2.4 HOLIMO

The HOLographic Imager for Microscopic Objects (HOLIMO) is an in-situ sonde developed by ETH Zürich (Henneberger et al., 2013). By this instrument, cloud particles with diameters between 6 µm and 2 mm of a well defined sample volume of 12 cm^3 can be imaged two-dimensionally (Ramelli et al., 2021). From the observations, the size spectrum and concentrations of cloud particles as well as the water content of clouds can be calculated. HOLIMO can either be operated on the ground or attached to slowly moving aircraft, such as helikites or ropeways. The instrument is compatible with the tethered balloon system HoloBalloon (Ramelli et al., 2020) which operated during the Cloudlab and PolarCAP campaign (Fig. 2.6). This system allows the in-situ measurement of vertical profiles up to 1 km above the ground which enables detailed cloud characterisation. Furthermore, it may observe the changes of cloud particle properties during seeding experiments.

By conducting ground-based HOLIMO measurements next to the 2DVD, the possibility for a direct evaluation of the 2DVD measurements is given. Figure 2.7 shows a measurement example of HOLIMO on 8 March 2019 during a campaign in Wolfgang, Switzerland (Ramelli et al., 2021). It is clearly visible, that different particle types such as large rimed particles, columnar crystals, or irregular particles can be distinguished from each other. The measurements of HOLIMO and 2DVD are compared for precipitation events with clearly dominating particle types, so that conclusions about the 2DVD measurements can be drawn (see Sect. 4.2). However, due to the small sample volume and the limitation of the maximum detectable particle size, no conclusions should be drawn about the concentration or size distribution of precipitation particles.

Figure 2.6: The tethered balloon system HoloBalloon including HOLIMO on 8 December 2022 at Rapier-Platz, Switzerland. The picture is taken by Christopher Fuchs, ETH Zürich.

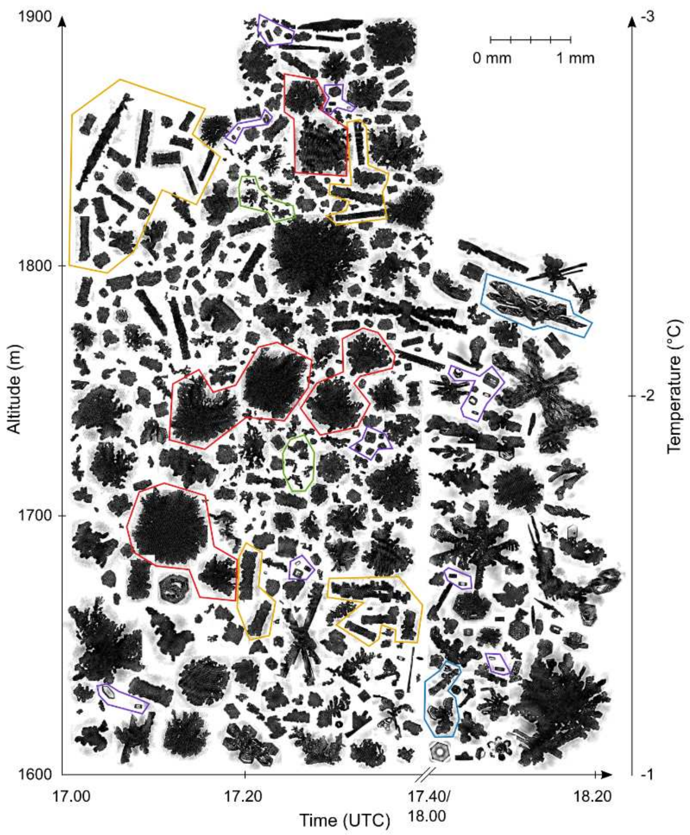

Figure 2.7: HOLIMO measurement example from 8 March 2019 at Wolfgang, Switzerland. The colours point out different particle types such as large rimed particles (red), columns (yellow), aggregates (blue), pristine ice particles (purple) and irregular particles (green) (Ramelli et al., 2021).

Chapter 3

2DVD – deducible hydrometeor and precipitation properties

In this chapter, variables of single hydrometeors which are provided by the manufacturers software are explained. Further, different variables and ways to analyse precipitation from 2DVD data are presented.

3.1 Properties of single particles

By means of software which was delivered from the 2DVDs manufacturer, a set of parameters is determined for each single hydrometeor:

a. The equivalent spherical diameter D_{eq} (mm) equals the diameter of a sphere with the same volume as the respective hydrometeor.

b. The vertical velocity ν ($\mathrm{m\,s^{-1}}$) is determined by the time required by the hydrometeor to fall from the upper to the lower light sheet.

c. The particle volume V ($\mathrm{mm^3}$) is calculated by splitting the hydrometeor into horizontal slices whereas each slice is assumed to have an area of an ellipse and the height of one line. V is the sum of all slice volumes (Kruger and Krajewski, 2002).

d. The effective measuring area A_{eff} ($\mathrm{mm^2}$) is defined as the part of the virtual measuring area in which a hydrometeor with a certain size could have been detected. Between the detected particle and the borders of the virtual measuring area, there must be at least one non-shadowed pixel which reduces A_{eff} the more the larger the particle is.

e. The oblateness O (without unit) is defined as the ratio of particle height and particle width. The manufacturers software calculates O from information of both cameras A and B as follows:

$$O = \sqrt{\left(\frac{height_A}{width_A}\right)\left(\frac{height_B}{width_B}\right)} \tag{3.1}$$

$width_A$ and $width_B$ represent the width of the widest scan line of the respective camera (Kruger and Krajewski, 2002). O is an important shape parameter which can be helpful for the detection of different ice crystal shapes. However, for solid particles, the applied method to calculate O can be highly error-prone, especially at horizontal winds that tilt falling hydrometeors.

For the display of single particles, an own program was written. This is based on the pixel information for each line and each camera which can be received by the manufacturers software. Examples can be found in Sect. 4.2.

Measurement uncertainties given by the 2DVDs manufacturer are shown in Tbl. 2.2. For the calculation of precipitation parameters from the variables presented above, the correct assumption of uncertainties is challenging and was neglected in most 2DVD research. The actual uncertainties are mostly dependent on vertical and horizontal winds and may therefore vary for different hydrometeors. An uncertainty of ±4% can be assumed for ν, based on manufacturers data. For vertical and horizontal resolutions, an uncertainty of less than 0.17 mm is specified.

3.2 Precipitation properties

3.2.1 Precipitation rate

The 2DVD is an advantageous instrument to determine precipitation rates under different weather conditions because hydrometeors of various types can be well observed. The precipitation rate R of the 2DVD for liquid precipitation is calculated as follows:

$$R = \sum_{j(t_0)=1}^{j(t_0+\Delta t)} V_j \frac{3600}{\Delta t} \frac{1}{A_{eff,j}} \qquad \left[\mathrm{mm\,h^{-1}}\right] \tag{3.2}$$

with the integration time interval Δt (s) and the effective measuring area $A_{eff,j}$ ($\mathrm{mm^2}$) and volume V_j ($\mathrm{mm^3}$) of each particle j. In case of solid precipitation, the liquid equivalent volume $V_{eq,j}$ of particles must be taken into account for the calculation of R. For ice, a density ρ_{ice} of $0.9\,\mathrm{g\,cm^{-3}}$ can be assumed which yields

$$V_{eq,j} = V_j \frac{\rho_{ice}}{\rho_{H_2O}} \qquad \left[\mathrm{mm^3}\right] \tag{3.3}$$

with $\rho_{H_2O} = 1\,\mathrm{g\,cm^{-3}}$ and eventually

$$R = \sum_{j(t_0)=1}^{j(t_0+\Delta t)} V_{eq,j} \frac{3600}{\Delta t} \frac{1}{A_{eff,j}} \qquad \left[\mathrm{mm\,h^{-1}}\right] \tag{3.4}$$

However, especially for large snow particles, the exact determination of the particle volume is challenging because the delicate structure of ice crystals can not be sufficiently resolved. For this purpose, studies about the snow bulk density in dependence of particle size were conducted (Brandes et al., 2007; Zhang et al., 2021) and different density–size relations were determined. However, this issue is not further explored in this thesis.

3.2.2 Particle size distribution

The determination of the particle size distribution (PSD), in case of liquid precipitation referred to as drop size distribution (DSD), has been the most important component of 2DVD research in the past. It is defined as the number of detected particles per unit of air volume and per unit of particle diameter interval. The PSD is usually denoted as $N(D_i)$. The choice of the size class width ΔD (mm) is essential for the resulting PSD shape. In this work, ΔD was chosen to equal the horizontal resolution of the instrument which is 0.17 mm. The PSD is computed as followed:

$$N(D_i) = \frac{1}{\Delta t \Delta D} \sum_{j=1}^{M_i} \frac{1}{A_{eff,i,j} \cdot 10^{-6} \cdot \nu_{i,j}} \qquad \left[\mathrm{m}^{-3}\,\mathrm{mm}^{-1}\right] \tag{3.5}$$

with M_i as the number of particles in size class i during Δt and $\nu_{i,j}$ as vertical velocity of particle j in size class i.

3.2.3 Relations of particle properties

Precipitation can be analysed by establishing time series of particle properties such as D_{eq}, V, O, or ν. For example, trends in precipitation evolution may become visible. Particularly with regard to the presented measurement campaign, cloud seeding signatures may be detected.

Moreover, the relation of variables mentioned in Sect. 3.1 to each other often indicates different particle types. Especially plotting diameter versus oblateness and diameter versus vertical velocity proves useful for the precipitation analysis.

3.2.4 Particle number concentration

The particle number concentration (PNC) describes the number of hydrometeors per unit of air volume:

$$PNC = \frac{1}{\Delta t} \sum_{j=1}^{M} \frac{1}{A_{eff,j} \cdot 10^{-6} \cdot \nu_j} \qquad \left[\mathrm{m}^{-3}\right] \tag{3.6}$$

with M as number of particles during Δt. The PNC on the ground can be helpful, for example, for closure studies regarding precipitation evolution.

Chapter 4

Measurement results

In this chapter, measurement results of the PolarCAP and Cloudlab campaign are presented. Section 4.1 includes the calibration outcome and measurement evaluation of the 2DVD. The latter is achieved by comparing 2DVD precipitation rates and PSD with simultaneous measurements of other instruments. In Sect. 4.2, precipitation events that led to differently shaped solid precipitation particles on the ground are examined. Those events were monitored by various ground-based in-situ and remote-sensing instruments which offered the opportunity to study precipitation formation and development. Section 4.3 presents ground precipitation signatures of cloud seeding experiments and thus another important application example of the 2DVD.

4.1 2DVD calibration and evaluation

4.1.1 Calibration procedure on 12 December 2022

On 12 December 2022 around noon, opportune weather conditions, i.e. no precipitation and only weak winds enabled the calibration of the 2DVD. The set of steel spheres with known diameters ranging from 0.5 mm to 10 mm was measured accurately enough to use the applied calibration factors for the whole campaign. Figure 4.1 shows the relation between O and D_{eq} for each steel sphere. Ideally, O would equal 1 for each sphere and D_{eq} would equal the value of one of the yellow grid points. The vast majority of spheres of all sizes induces the expected diameters. Measured D_{eq} of 0.5 mm-spheres deviate the most from the actual size but not by more than the stated resolution of 0.17 mm. Due to electrostatic charge, the smallest spheres sometimes cling together which explains some of the clear outliers. Another reason for outliers could be that the matching algorithm assigned different spheres to each other as multiple steel spheres of the smallest size may simultaneously have entered the measuring area more frequently during the calibration (Randeu et al., 2002).

4.1.2 Comparison of precipitation rates of different instruments

LACROS contains three different in-situ instruments, whose precipitation rates can be compared against each other, which are the 2DVD, the Parsivel^2 and the Vaisala weather station. Since the 2DVD has established as a valuable in-situ instrument for precipitation measurements, many studies have compared the device with other precipitation sensors (see Sect. 2.3.3). Especially 2DVD and Parsivel^2 have been evaluated most frequently against each other.

In this section, precipitation rates for rain are examined. For the instrument comparison in this work, a time period was chosen in which both warm and cold rain occurred.

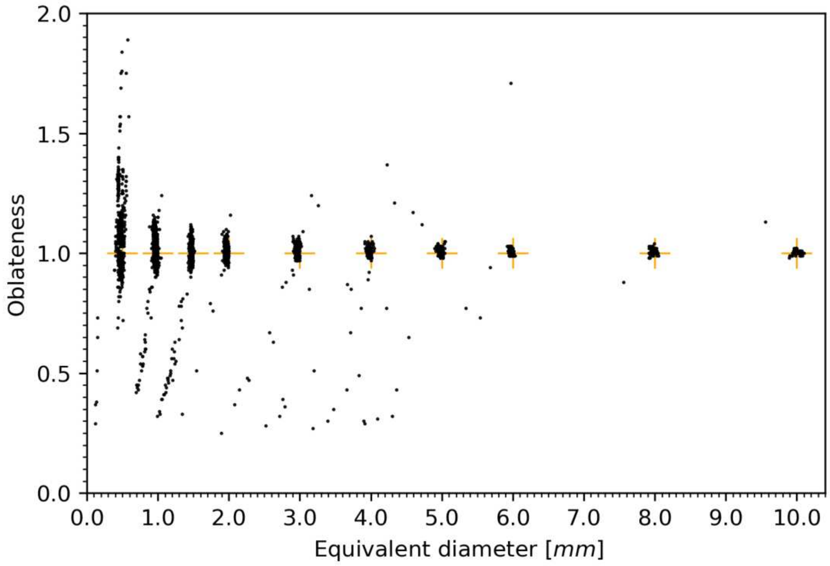

Figure 4.1: Calibration results on 12 December 2022 at the beginning of the PolarCAP campaign. Each data point represents one calibration sphere with known diameter. Outliers are mostly caused by spheres clinging together.

In case of stratiform precipitation, cold rain usually produces larger droplets, because ice crystals have a longer residence time in the cloud where they can grow, whereas condensed cloud droplets precipitate as soon as they are large enough to fall out of the cloud.

Figures 4.2a and b show the RPG94_LACROS Doppler velocity and the slanted linear depolarisation ratio (SLDR), respectively, from 00:00 UTC to 11:00 UTC on 5 January 2023. Until around 05:30 UTC at 1.4 km height, absolute values of the Doppler velocity suddenly increase and significantly higher SLDR values can be identified. Those changes are caused by melting ice crystals which firstly increase their fall velocity during the melting process and secondly cause higher SLDR values while liquid water is present around the initial ice crystals. By this so called melting layer, cold-rain events can be distinguished from warm-rain events by polarimetric Doppler radar measurements.

R and accumulated precipitation determined by the 2DVD, Parsivel^2, and the weather station are shown in Fig. 4.2c. R was calculated for both instruments with an integration time interval of 60 s to better compare the results and evaluate the instruments against each other. First of all, it is noticeable, that the weather station did not detect any particles. R of both 2DVD and Parsivel^2 is zero between 05:30 UTC and 06:15 UTC, which better allows a separate consideration of the cold-rain period before 05:30 UTC and the warm-rain period after 06:15 UTC.

In general, R of the 2DVD and the Parsivel^2 agree well with each other. However, at some times, peaks of the Parsivel^2 are higher than those of the 2DVD. Moreover, between around 03:45 UTC and 05:30 UTC, R of the Parsivel^2 slightly exceeded R of the 2DVD. This is reflected in the accumulated precipitation, which is 0.57 mm for the 2DVD and 0.63 mm for the Parsivel^2 at 06:00 UTC. At 11:00 UTC, accumulated precipitation is 0.93 mm for the 2DVD and 0.98 mm for the Parsivel^2. This shows, that firstly, the Parsivel^2 detected 0.06 mm more precipitation during the cold-rain period and secondly, R of the two instruments only varied by 0.01 mm in the warm-rain period.

Figure 4.3a and b show the PSD of the 2DVD from 03:45 UTC to 06:00 UTC where R of the Parsivel^2 is noticeably higher than of the 2DVD, and from 06:00 UTC to 11:00 UTC for the warm-rain period, respectively. It is remarkable that almost no droplets with

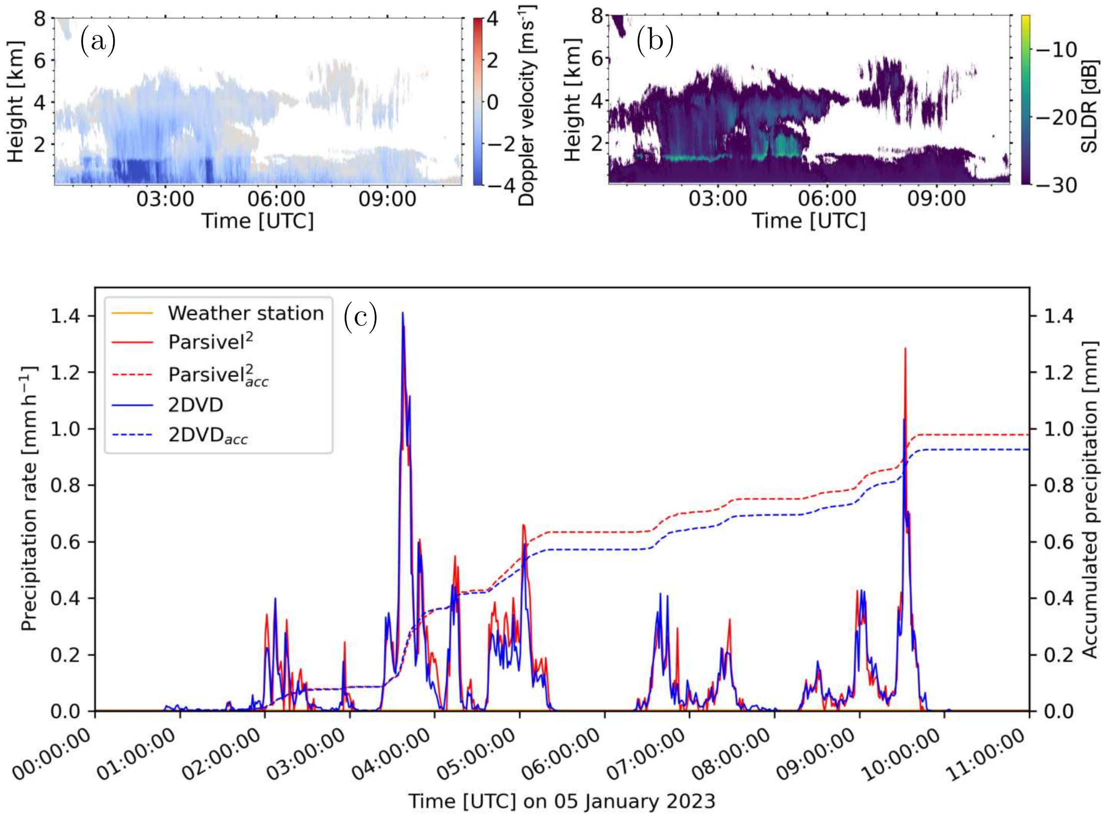

Figure 4.2: In-situ and remote-sensing measurement results for the drizzle event on 5 January 2023. RPG94_LACROS (a) Doppler velocity, (b) SLDR, and (c) precipitation rates and accumulated precipitation determined by measurements of different instruments are shown. Integration intervals for all presented precipitation rates are 60 s. Note that the weather station has not detected any hydrometeors.

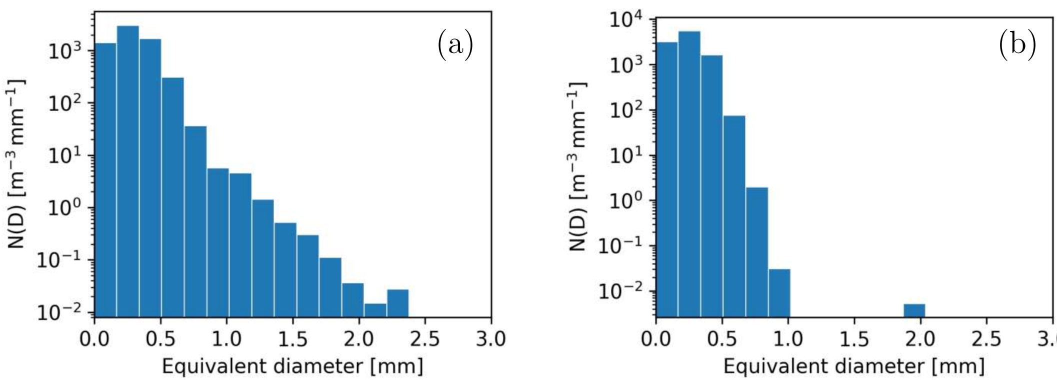

Figure 4.3: 2DVD PSD of precipitation on 5 January 2023 (a) from 03:45 UTC to 06:00 UTC and (b) from 06:00 UTC to 11:00 UTC.

$D_{eq} > 1$ mm occurred during the warm-rain period, but the cold rain contained a proportion of droplets of such size. Therefore, there is a possibility, that the difference in R between 2DVD and Parsivel^2 during the cold-rain period is caused by larger droplets. Minutely averaged horizontal wind speeds derived by measurements of the Vaisala weather station attached to the HATPRO 5G on the container roof are shown in Fig. 4.4. They are on average 2 m s^{-1} to 3 m s^{-1} higher during the cold-rain period, but if this difference contributed to the difference in R cannot be evaluated at this point. Further, the wind

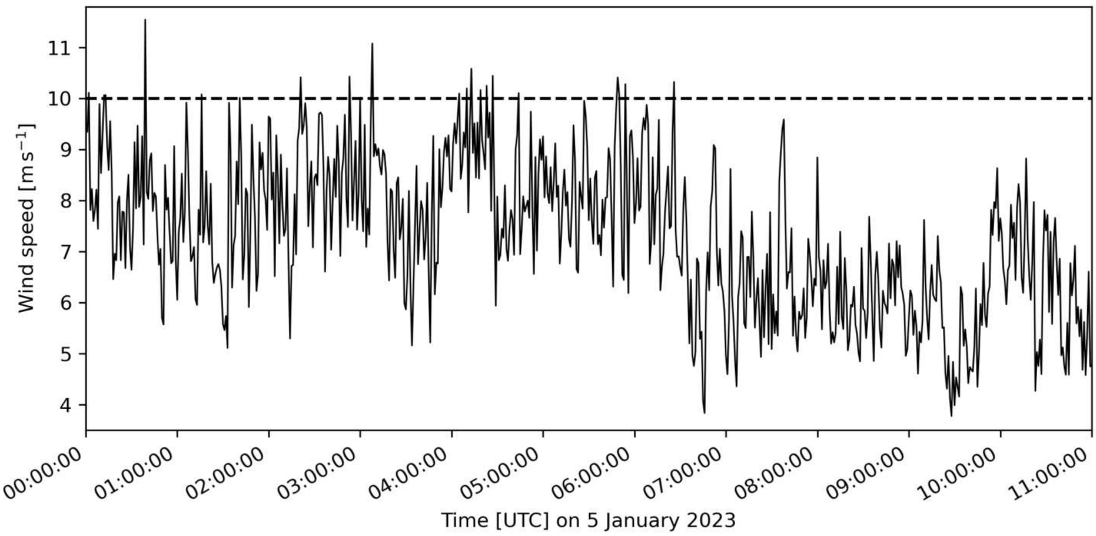

Figure 4.4: Minutely averaged horizontal ground wind speeds measured by the Vaisala weather station on the container roof on 5 January 2023 from 00:00 UTC to 11:00 UTC. The dashed line indicates $10\,\mathrm{m\,s^{-1}}$, which is the threshold up to which the 2DVD instrument specifications (Tbl. 2.2) are valid.

speed exceeds $10\,\mathrm{m\,s^{-1}}$ at some single minutes, during which the 2DVD specifications are theoretically not valid anymore. However, the impact on R is most likely negligible.

4.2 Detection of different ice crystal shapes

On 17 and 18 January 2023, the holographic imager HOLIMO was operated on the ground next to the 2DVD (Fig. 4.5). During those two days, solid precipitation with different ice crystal shapes at different times was observed by eye and recorded in an educated-eye protocol. Table 4.1 shows an overview about observed particle shapes during the four investigated time periods. In the following, the meteorological scenario on 17 and 18 January 2023 is presented. Furthermore, measurement data of the 2DVD, HOLIMO, and remote-sensing instruments of LACROS are analysed to investigate four concrete time periods in which different ice crystal shapes were observed by eye.

During 17 and 18 January 2023, a low pressure system over the North Sea transported cold and humid air masses towards central Europe. An occlusion front stretched from southern Czech Republic through northern Switzerland to the Bay of Biscay and determined the weather over the measurement location at Rapier-Platz during this time (Fig. 4.6). Figure 4.7 shows GFS model temperatures at 850 hPa over Europe and illustrates, that temperatures over the measurement location at Rapier-Platz were clearly below 0°C.

Table 4.1: Educated-eye protocol entries about ice crystal shapes on 17 and 18 January 2023.

date	**time period**	**observed particles (protocol)**
17 January 2023	11:30 – 11:35 UTC	small irregular crystals, partly aggregated
	13:50 – 13:54 UTC	mix of dendrites, heavily rimed particles, and irregular crystals
	14:07 – 14:11 UTC	high number of dendrites
18 January 2023	09:44 – 09:48 UTC	some needles, mix of shapes

Figure 4.5: HOLIMO (foreground) and the 2DVD (background) during their operation on 16 January 2023. The picture is taken by Kevin Ohneiser.

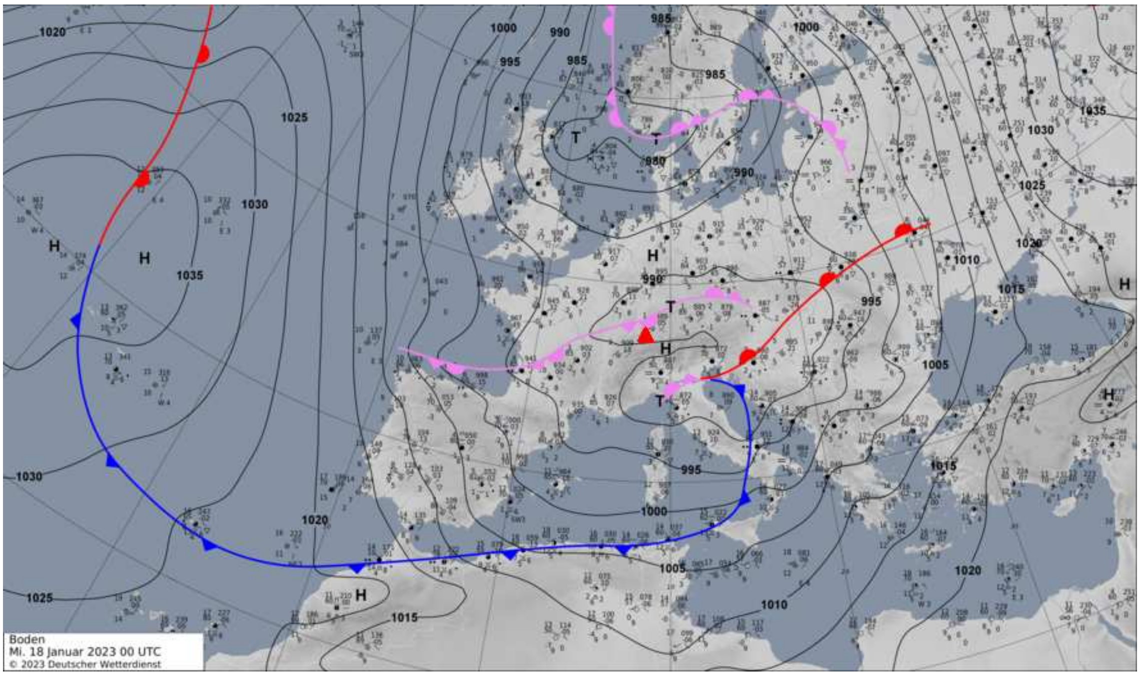

Figure 4.6: Air pressure at mean sea level and weather fronts over Europe at 00 UTC on 18 January 2023. The red triangle indicates Rapier-Platz near Eriswil, Switzerland. The map is adapted from Wetterzentrale (2023a).

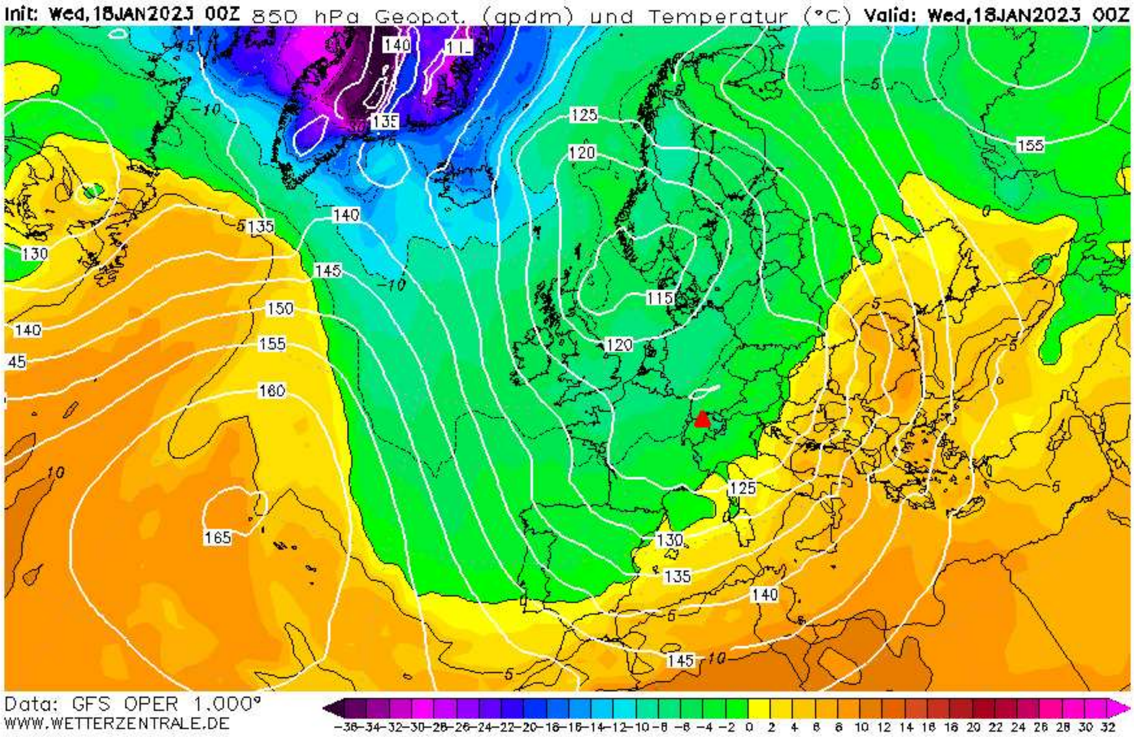

Figure 4.7: Geopotential and temperature at 850 hPa over Europe at 00 UTC on 18 January 2023. The red triangle shows the measurement location. The map is adapted from Wetterzentrale (2023b).

The reflectivity measurements of the RPG94_LACROS radar show stratiform precipitation systems on both days (Fig. 4.8a, b). Because the instruments blower system was off during the investigated case study period, snow accumulation occurred on the radome sheets which led to non-negligible attenuation effects. Thus, the reflectivity offset to Mira-35 was calculated as described in App. B and was determined to be 20 dB. From the RPG94_LACROS Doppler velocity, convective precipitation-generating cells can be identified on both days (Fig. 4.8c, d). SLDR values do not show any sudden increase with decreasing height which indicates the absence of a melting layer (Fig. 4.8e, f). In the following subsections, results of in-situ and remote-sensing measurements for four different time periods during 17 and 18 January 2023 are presented. HOLIMO data were processed by Christopher Fuchs, ETH Zürich (personal communication).

4.2.1 17 January 2023, 11:30 – 11:35 UTC: irregular crystals and aggregates

On 17 January 2023 from 11:30 to 11:35 UTC, irregular and aggregated crystals were observed by eye. Figure 4.9 shows 2DVD measurements during that time period. In the O versus D_{eq} diagram, two clusters stand out, the first one with $D_{eq} < 0.5$ mm and $O < 0.45$, the second one with $0.2\,\mathrm{mm} < D_{eq} < 1.5\,\mathrm{mm}$ and $0.7 < O < 1.3$. Vertical velocities of the first cluster are mainly below $0.5\,\mathrm{m\,s^{-1}}$. Single particles shown in Fig. 4.9a, hereafter referred to as particle 1, particle 2, etc., were arbitrarily chosen in a way that as many clusters in Fig. 4.9a and b as possible are represented. The smallest particles such as particle 1 only have the size of one or two times the resolution of the 2DVD and can therefore hardly be resolved in detail. Particle 2 seems to be columnar or needle-shaped, particles 3 and 4 could be irregular crystals or aggregates, possibly also rimed to some extent. In the 2DVD measurements, some particles appear with unrealistically long vertical edges in

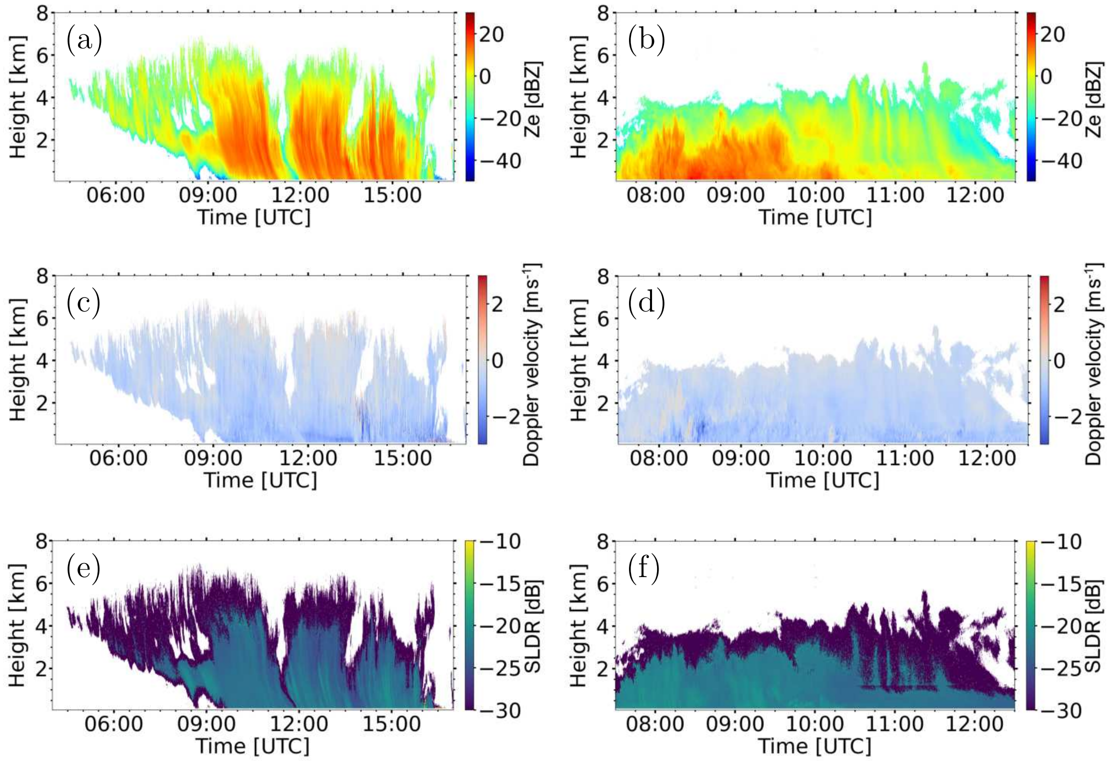

Figure 4.8: RPG94_LACROS (a, b) reflectivity, (c, d) Doppler velocity, and (e, f) SLDR on 17 January (left) and 18 January 2023 (right). An offset to Mira-35 of 20 dB was added to the reflectivity measurements (a, b) due to snow accumulation on the radome sheets (see App. B).

all cases presented in this section. All of them have O values > 2. For this reason, they are colored orange in the v versus D_{eq} diagram and are not included in the O versus D_{eq} diagram in this and the following subsections. Examples can be found in Fig. C.1. This phenomenon was also observed by Grazioli et al. (2014) who suggests that such signatures are caused by particles which linger in the virtual measurement area for an unusual long time span, for example, due to small-scale wind effects.

HOLIMO data were only analysed for one minute from 11:32 UTC to 11:33 UTC because a sufficient amount of ice crystals has been detected in this period. Figure 4.10 shows all HOLIMO images that were detected by the algorithm of Christopher Fuchs, ETH Zürich. The particle sizes vary from around 0.15 mm, which is about the resolution of the 2DVD, to 2.5 mm. A variety of crystal shapes was detected and some particles resemble the ones detected by the 2DVD. The columnar crystal (Fig. 4.10, line 3, column 3) equals particle 2 from the 2DVD measurements, for example. Some particles measured by HOLIMO can be identified as aggregates, such as the aggregated plates (Fig. 4.10, line 2, column 2) and others as irregular crystals (e.g., line 2, column 3). The smallest particle detected by HOLIMO (line 1, column 4) would probably appear in the 2DVD measurements similar as particle 1 in Fig. 4.9c.

In the following subsections, further remote sensing results are presented after the in-situ measurement results. Unfortunately, from 11:30 UTC to 11:35 UTC there are no Mira-35 measurements available (because the radar was performing a scan pattern) and can therefore not be presented at this point.

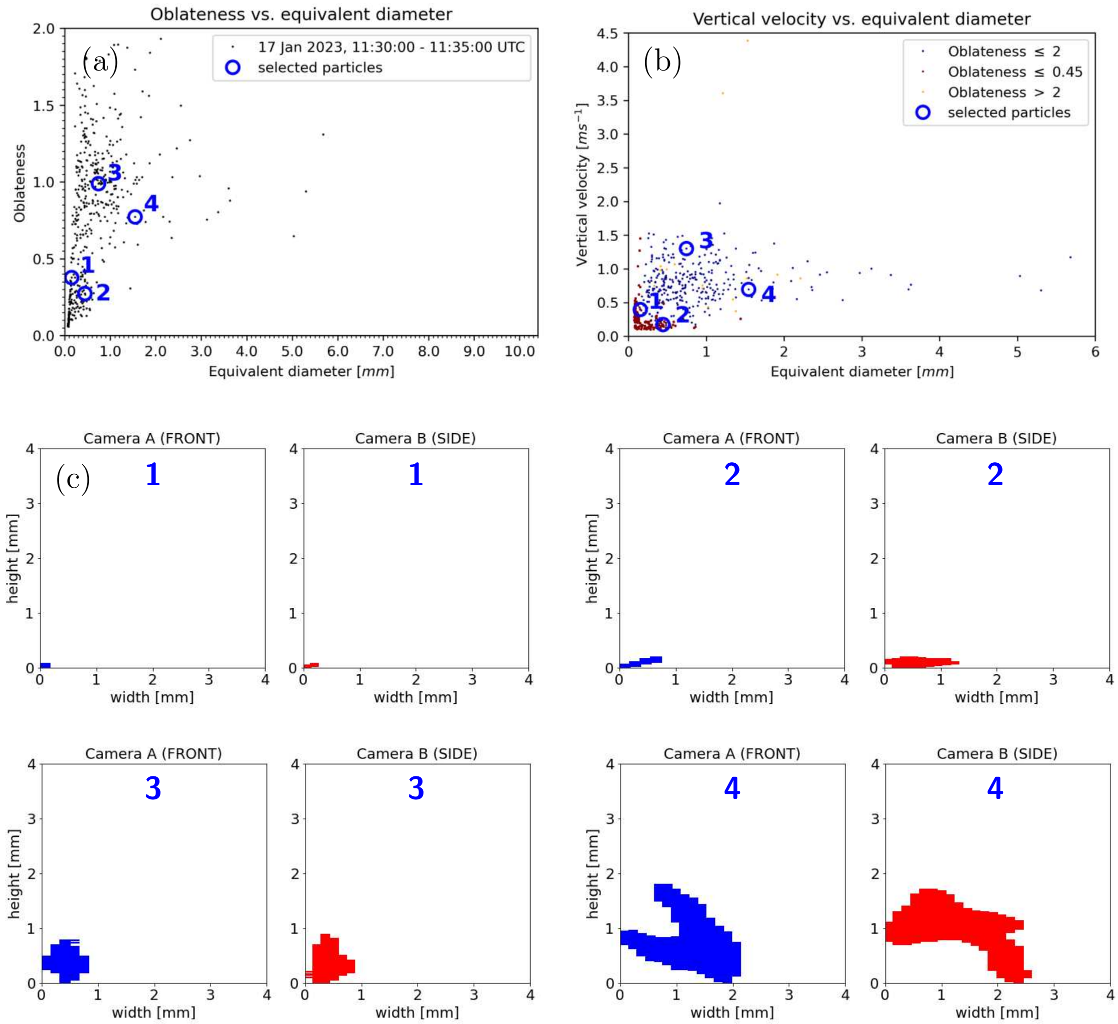

Figure 4.9: 2DVD measurements on 17 January 2023 from 11:30 UTC to 11:35 UTC including (a) oblateness versus equivalent diameter, (b) vertical velocity versus equivalent diameter, and (c) single characteristic hydrometeors. The blue numbers indicate the same hydrometeor in all subfigures.

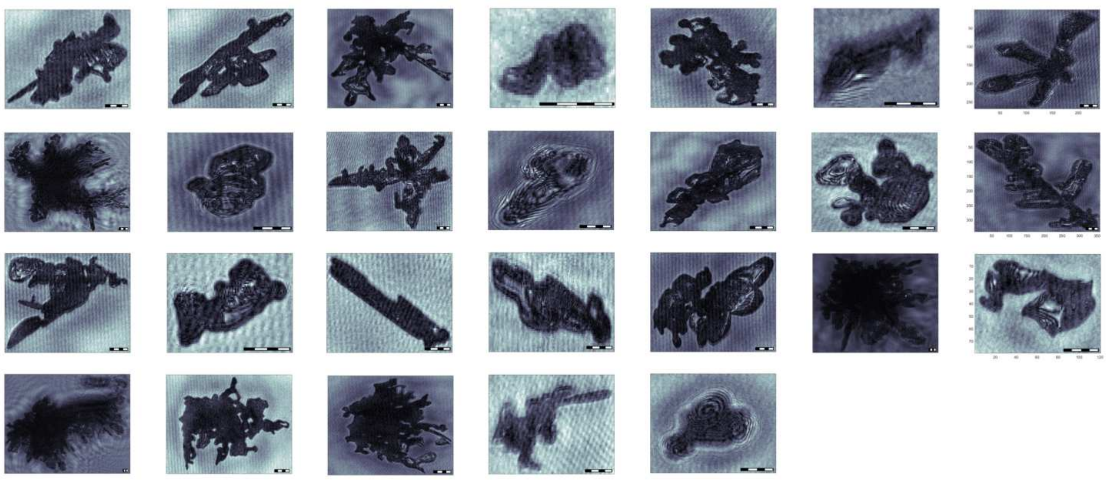

Figure 4.10: Ice crystals detected by HOLIMO on 17 January 2023 from 11:32 UTC to 11:33 UTC. The scale in the lower right corner of each picture corresponds to 100 µm with 25 µm subdivision.

4.2.2 17 January 2023, 13:50 – 13:54 UTC: dendrites, strongly rimed particles, irregular crystals

Around 2.5 hours after the detection of irregular crystals and aggregates, dendrites and rimed particles were observed additionally by eye. 2DVD measurement results show two main clusters and one less pronounced one (Fig. 4.11a and b). The first cluster ranges in D_{eq} from 0.2 mm to 0.7 mm, in O from 0.2 to 0.5, and in v from $0.1\,\mathrm{m\,s^{-1}}$ to $0.5\,\mathrm{m\,s^{-1}}$. Such oblate particles are often columnar and appear in the 2DVD measurements like particle 1 (Fig. 4.11c) or similar. The second main cluster includes particles with D_{eq} between

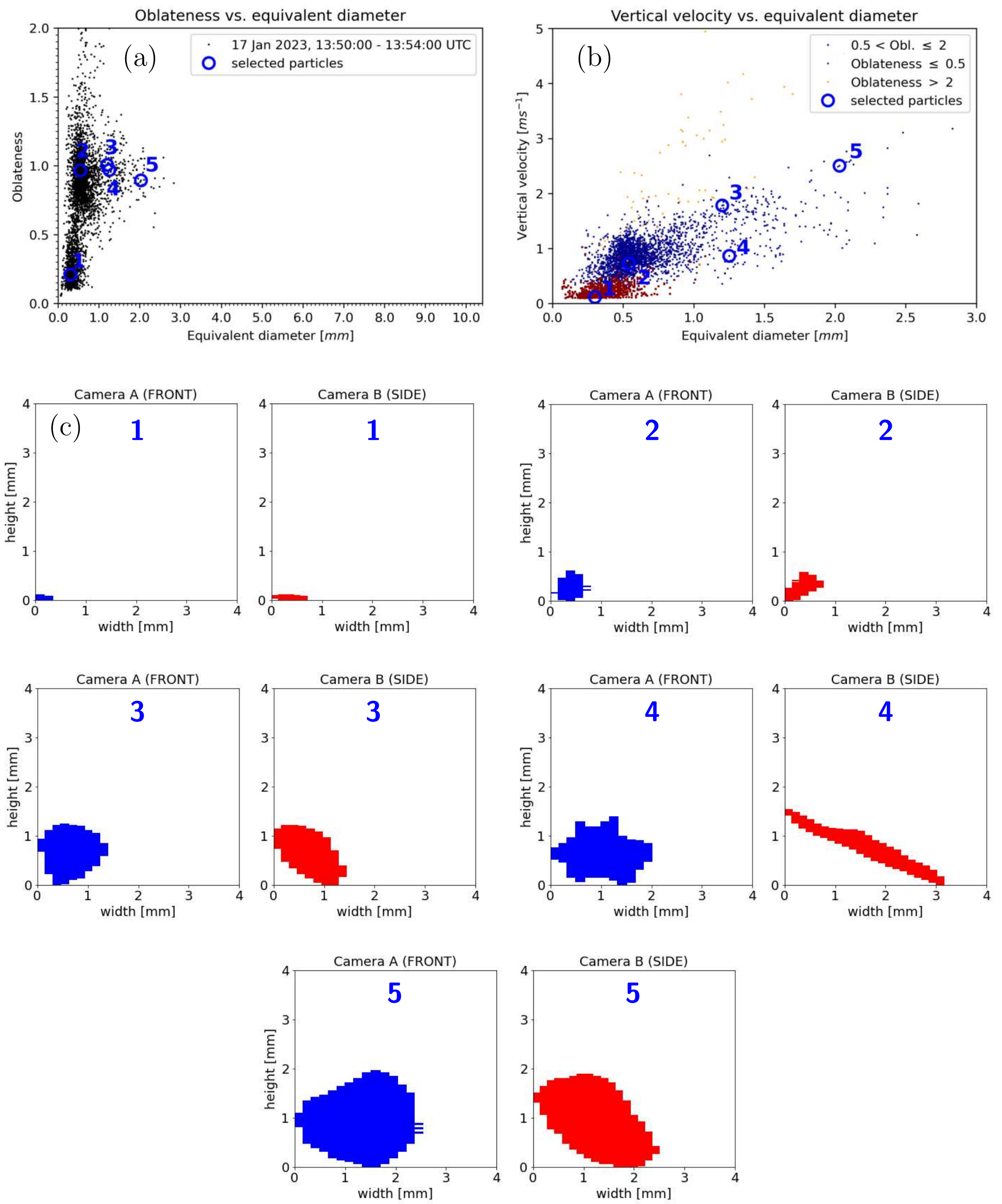

Figure 4.11: 2DVD measurements on 17 January 2023 from 13:50 UTC to 13:54 UTC including (a) oblateness versus equivalent diameter, (b) vertical velocity versus equivalent diameter, and (c) single characteristic hydrometeors. The blue numbers indicate the same hydrometeor in all subfigures.

0.3 mm and 0.8 mm, with O between 0.7 and 1.3, and v between 0.5 m s^{-1} to 1.4 m s^{-1}. Due to the large O range, particles in this cluster can be shaped differently. As D_{eq} is below 1 mm and thus quite small, the particle shapes are additionally not well resolved. Further, particles with $D_{eq} > 1$ mm, O between 0.5 and 1.5, and varying v were measured. Figure 4.11b shows a slight trend towards higher v of larger particles. Moreover, two hydrometeor types could be identified from pictures of single particles (Fig. 4.11c) which are graupel-like particles (particle 3 and 5) and dendrites (particle 4). Particle 1 could be a needle or a column and particle 3 could have different basic shapes and be rimed to some extent. As in the previous case, 2DVD data contain particles with $O > 2$ and v up to 5 m s^{-1} which are not included in Fig. 4.11a.

HOLIMO images from this time period show a number of different crystal shapes (Fig. 4.12). The pictures show columns from which needles are grown perpendicularly (e.g., line 2, column 4; line 3, column 1), irregular crystals (e.g., line 2, column 5; line 2, column 6), one dendrite (line 5, column 5), particles that can be interpreted as aggregates (e.g., line 1, column 2; line 3, column 6), and particles that seem to be strongly rimed (e.g., line 3, column 4).

The conduction of simultaneous remote sensing measurements enables the investigation of the formation of different particle shapes. Precipitation measurements of Mira-35 during this and the subsequent time period (Sect. 4.2.3) are shown in Fig. 4.13. To investigate the surrounding conditions of the hydrometeors from the time of their formation until they were detected by the in-situ instruments on the measurement site, a fall streak algorithm written by Kevin Ohneiser, TROPOS (personal communication), was applied. The basic principle of the algorithm is that a time point when a fall streak reaches ground which refers to the lowest height bin is chosen. In each further step, the bin above within ±30 s is chosen such that the reflectivity gradient to the bin below is minimal. In case of horizontally homogeneous reflectivity values, the bin with the highest reflectivity is chosen. The fall streak reaching the ground during this time period at 13:51 UTC starts at around 2.8 km height. At around 1 km, significant wind shear is visible. Figure 4.14 presents the reflectivity of RPG94_LACROS, spectral width and Doppler velocity by Mira-35, and the temperature of the European Centre for Medium-range Weather Forecasts (ECMWF)

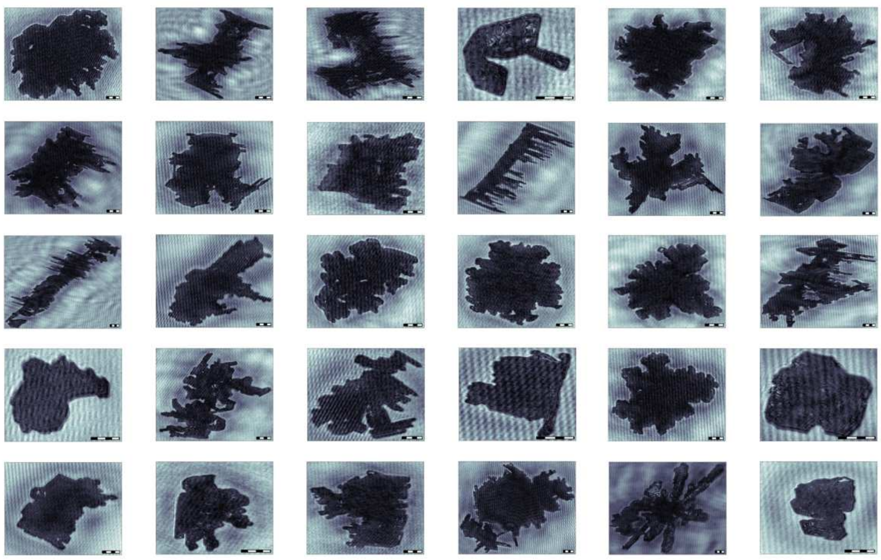

Figure 4.12: Ice crystals detected by HOLIMO on 17 January 2023 from 13:50 UTC to 13:54 UTC. The scale in the lower right corner of each picture corresponds to 100 µm with 25 µm subdivision.

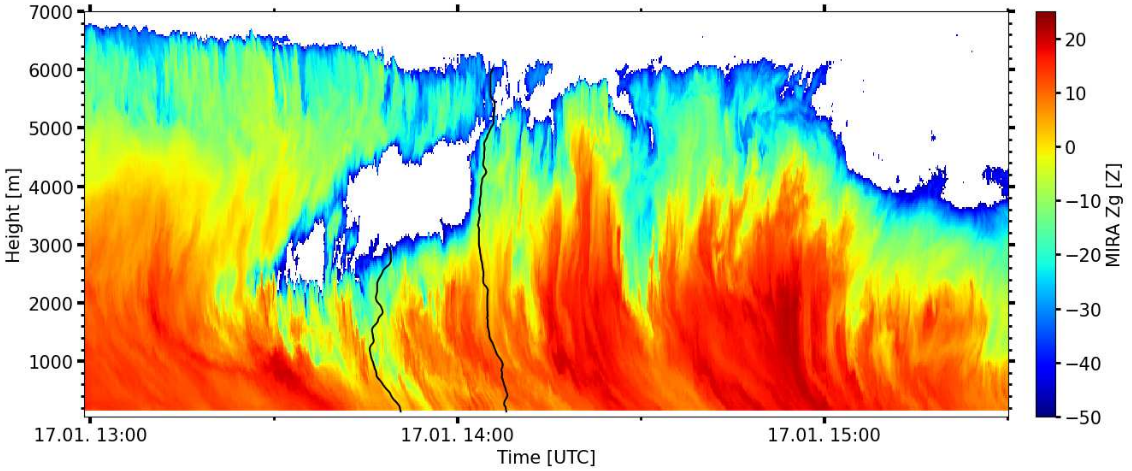

Figure 4.13: Mira-35 reflectivities on 17 January 2023 from 13:00 UTC to 15:30 UTC. The black lines indicate the way of hydrometeors reaching the ground at 13:51 UTC and 14:08 UTC, respectively, according to the fall streak algorithm written by Kevin Ohneiser, TROPOS.

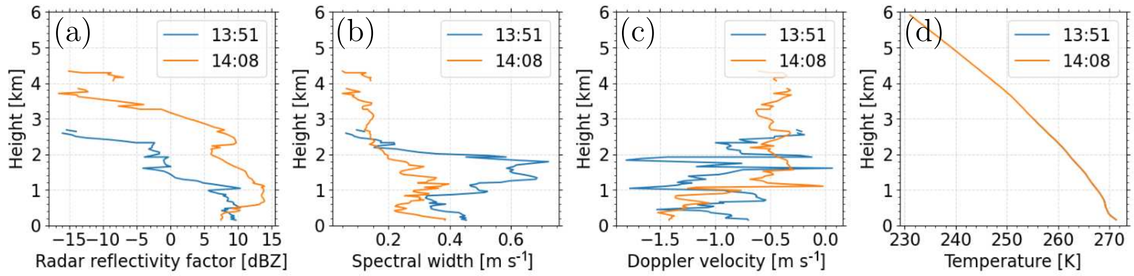

Figure 4.14: (a) RPG94_LACROS reflectivity plus 20 dB offset, (b) spectral width, (c) Doppler velocity, and (d) temperature of the ECMWF model along the black fall streaks in Fig. 4.13 (17 January 2023). Time points in the labels correspond to the time the fall streaks reach the ground.

model. The RPG94_LACROS reflectivity shows two strong increases, one up to around −3 dBZ at 2.6 km to 2.4 km, just below the top of the fall streak, and a second one between 1.6 km and 1 km up to 10 dBZ. During the first increase, temperatures were around −15°C. According to the ice crystal habit diagram in Fig. 1.4, dendrites grow at this temperature if the ice supersaturation is high enough. The second one occurs at temperatures between around −9°C to −5°C which are suitable conditions for column and needle formation. Between 2.2 km and 1.8 km, the spectral width is significantly increasing which can be explained either by the presence of an increasing number of particle modes or increased turbulence. At around 1.3 km and 1 km, there are decreases in the spectral width. The Doppler velocity is fluctuating, but increasing absolute velocity values below 1.6 km are visible.

The formation of needles and dendrites can be explained by the remote sensing signatures and model temperatures along the fall streak in combination with the habit diagram of Bailey and Hallett (2009). The significant wind shear below around 1000 m might have contributed to particle aggregation which would explain the observation of aggregates by HOLIMO. Somewhere along the fall streak, a cloud layer containing liquid water droplets must have been present to enable riming of entering ice crystals. For such kind of examination, further analysis of the remote-sensing data would be required.

4.2.3 17 January 2023, 14:07 – 14:11 UTC: dendrites

About another 15 minutes later, a "high number of dendrites" is reported in the educated-eye protocol. However, the 2DVD signatures (Fig. 4.15) look quite similar to those shown in Sect. 4.2.2 (Fig. 4.11). The main difference between the two time periods is that more larger particles with D_{eq} up to 7 mm were measured from 14:07 UTC to 14:11 UTC. Particles 3 and 4 indicate that indeed some hydrometeors in the corresponding size range are plate-like crystals or dendrites. Especially the shape of particle 5 (Fig. 4.15) suggests

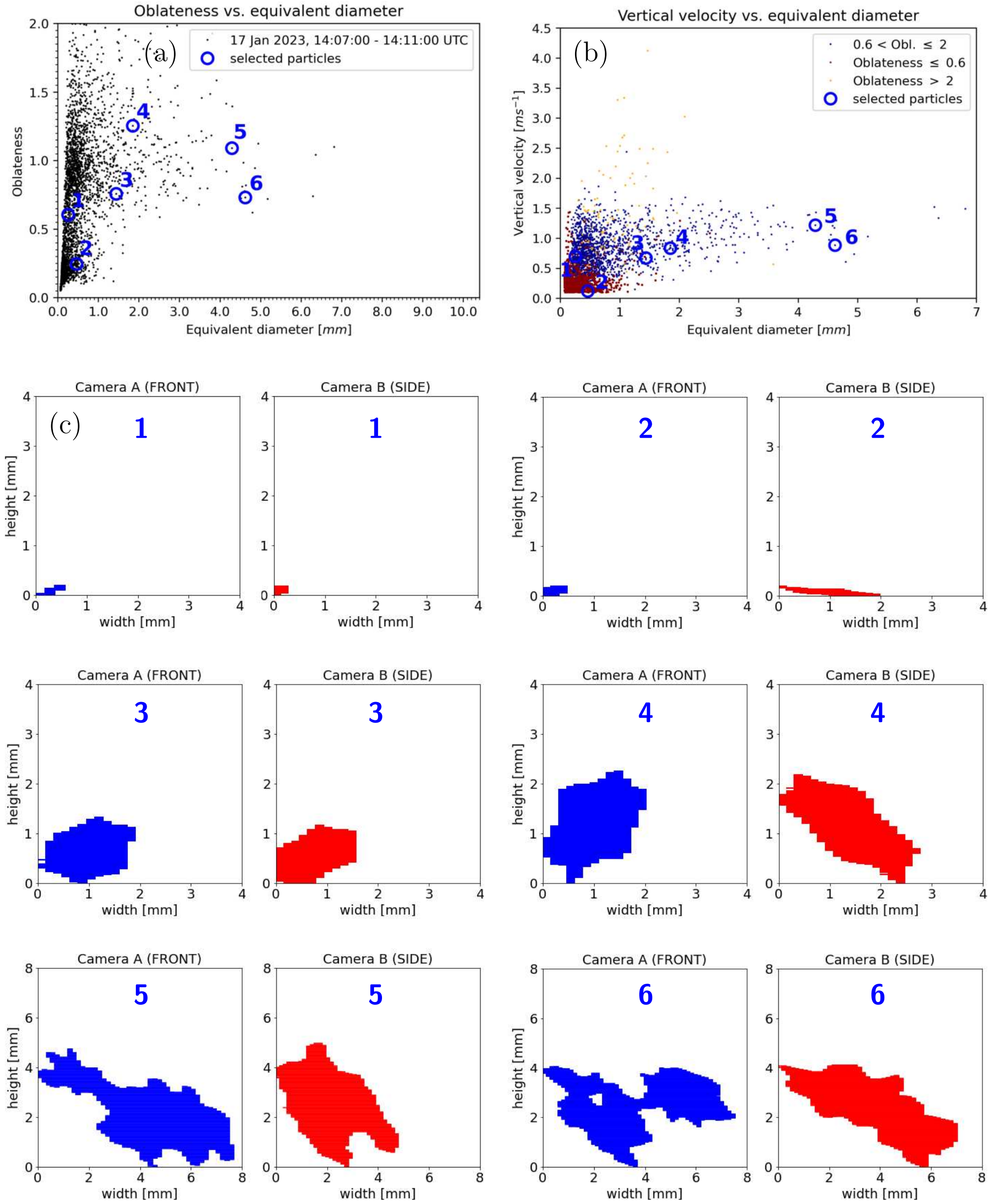

Figure 4.15: 2DVD measurements on 17 January 2023 from 14:07 UTC to 14:11 UTC including (a) oblateness versus equivalent diameter, (b) vertical velocity versus equivalent diameter, and (c) single characteristic hydrometeors. The blue numbers indicate the same hydrometeor in all subfigures. Particles 5 and 6 in (c) have a different scale than the other particles.

that some dendrites also aggregated with other particles due to the dendrite-like structure in the left in camera A.

HOLIMO images detected from 14:07 UTC to 14:11 UTC (Fig. 4.16) resemble the ones from the previous time period (Sect. 4.2.2). A similar fraction of columns was found (e.g., line 1, columns 1, 4, and 7). Also irregular crystals (e.g., line 3, column 5), aggregates (e.g., line 2, column 6; line 3, column 2), and rimed particles (e.g., line 1, column 2) were measured. However, no dendrites are visible in the HOLIMO images which is remarkable as a high amount of dendrites was observed by eye.

The fall streak that reached the ground during this time period is shown in Fig. 4.13. According to the Mira-35 measurements, it starts at around 6 km height. However, RPG94_LACROS data start at 4.4 km height due to the signal attenuation caused by snow accumulation on the radome sheets which is also the reason for the gap between 3.9 km and 4.1 km in Fig. 4.14. From 3.5 km to 2.5 km and from 2 km to 1 km height, reflectivity increases are visible. ECMWF model temperatures range from −20°C to −15°C during the first reflectivity increase which are good conditions for dendrite or plate-like crystal formation (see Fig. 1.4). During the second reflectivity increase, temperatures were between −11°C and −6°C which suggests the formation of plate-like and columnar crystals. The spectral width is significantly smaller than at the previous case and Doppler velocities are less fluctuating with absolute values smaller than those at 13:51 UTC at most heights.

Similar to the previous case, needle, dendrite and plate-like crystal formation can be assigned to different heights of the fall streak. The liquid water layer should still be present as rimed particles were detected again. Irregular crystals might have grown because particles that formed at the the top of the fall streak have penetrated layers of different microphysical properties. A comparison of the reflectivity curves in Fig. 4.14 shows that the upper height range with increasing reflectivity from 3.5 km to 2.5 km at 14:08 UTC is significantly larger than the one from 2.6 km to 2.4 km at 13:51 UTC. This difference might explain the higher amount of dendrites or plates in the 2DVD data from 14:07 UTC to 14:11 UTC.

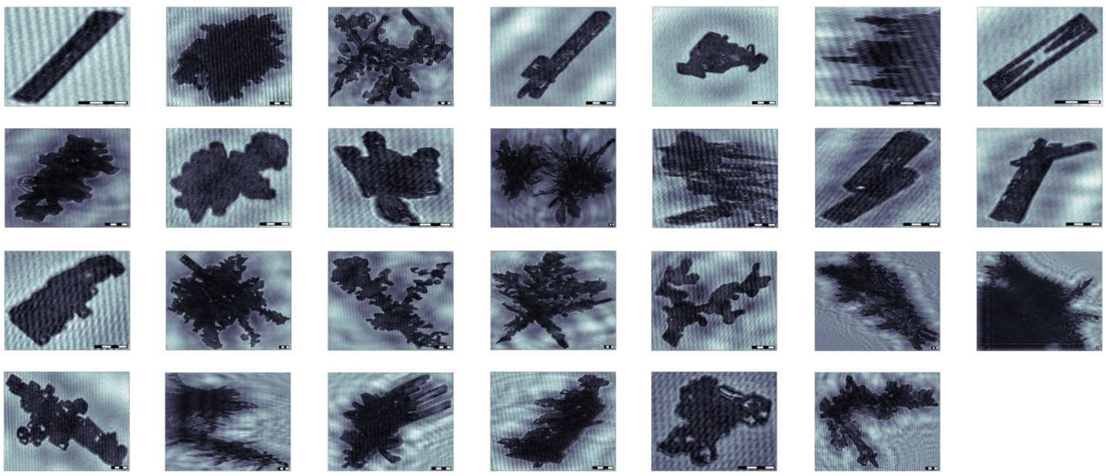

Figure 4.16: Ice crystals detected by HOLIMO on 17 January 2023 from 14:07 UTC to 14:11 UTC. The scale in the lower right corner of each picture corresponds to 100 µm with 25 µm subdivision.

4.2.4 18 January 2023, 09:44 – 09:48 UTC: needles / columns

On 18 January from 09:44 UTC to 09:48 UTC, a "mix of shapes" including "some needles" was observed according to the educated-eye protocol. Indeed, the 2DVD signatures (Fig. 4.17) suggest a majority of needles or columnar particles during that time period: O of most hydrometeors is clearly below 0.5 and a distinct trend towards decreasing particle number with increasing O is visible. Most particles have a $D_{eq} < 1\,\mathrm{mm}$ and $v < 0.5\,\mathrm{m\,s^{-1}}$, particles 1 and 2 (Fig. 4.17c) are characteristic for this cluster. Particle 3 has some sharp edges and should therefore not be a graupel particle but cannot be further categorised due to it's small size.

HOLIMO images taken during this time period (Fig. 4.18) are more various than the 2DVD results suggest. Some images (line 3, column 2; line 3, column 6) show long and thin crystals and look similar to the 2DVD particles 1 and 2 (Fig. 4.17). Other particles detected by HOLIMO have different basic shapes such as dendrites (line 3, column 1) or plates (line 1, column 7) and needles are grown on them.

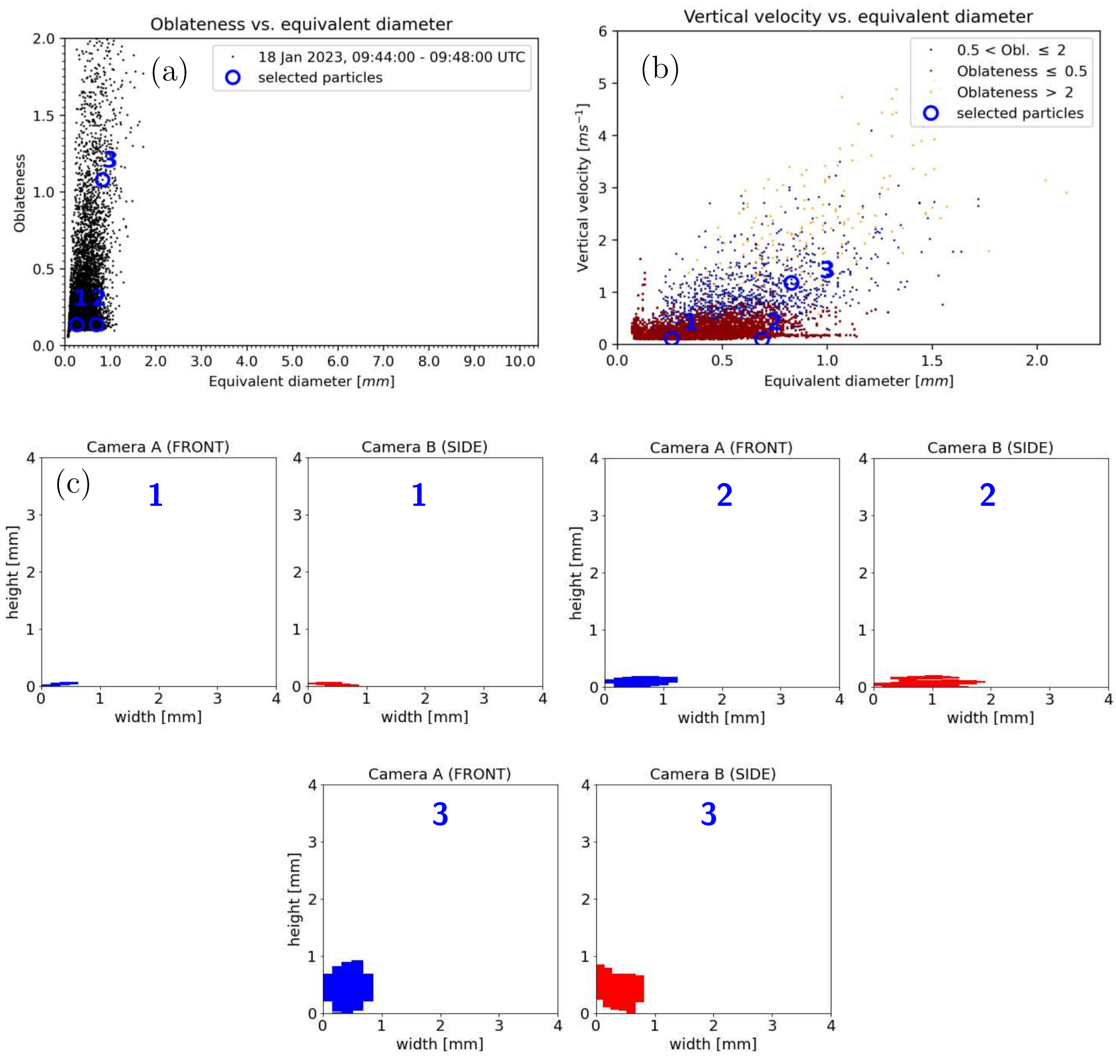

Figure 4.17: 2DVD measurements on 18 January 2023 from 09:44 UTC to 09:48 UTC including (a) oblateness versus equivalent diameter, (b) vertical velocity versus equivalent diameter, and (c) single characteristic hydrometeors. The blue numbers indicate the same hydrometeor in all subfigures.

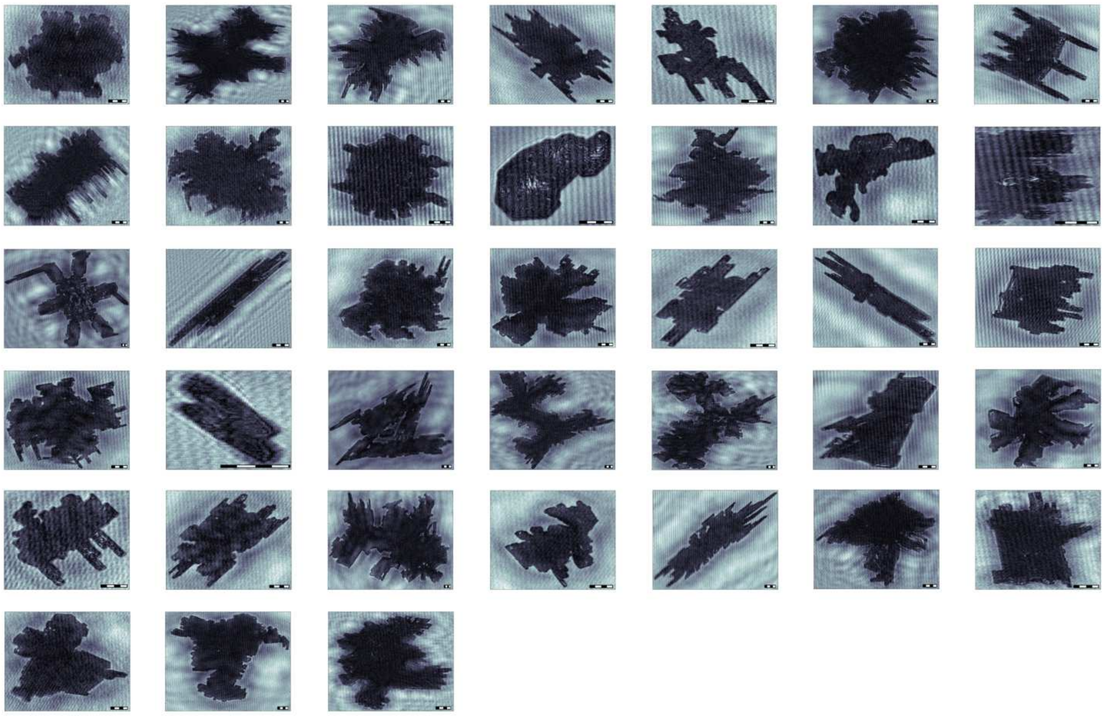

Figure 4.18: Ice crystals detected by HOLIMO on 18 January 2023 from 09:44 UTC to 09:48 UTC. The scale in the lower right corner of each picture corresponds to 100 µm with 25 µm subdivision.

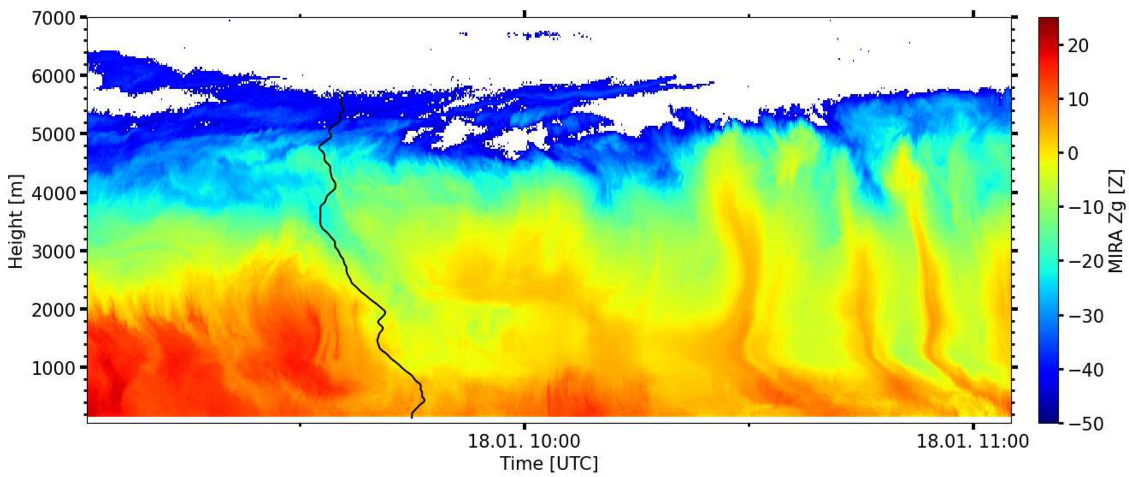

Figure 4.19: Mira-35 reflectivities on 18 January 2023. The black line indicates the fall streak reaching the ground at 09:45 UTC according to the algorithm written by Kevin Ohneiser, TROPOS.

Figure 4.19 shows Mira-35 reflectivities and the fall streak reaching the ground at 09:45 UTC. There is a continuous reflectivity increase between 3.5 km and 2.2 km height (Fig. 4.20). Temperatures at this height range are between −25°C and −15°C at which mainly plate-like crystals and, towards −15°C, dendrites are growing (Bailey and Hallett, 2009). At around 800 m, the reflectivity increases again by around 5 dB. At this height, the temperature was around −7°C which favours the growth of needles. The SLDR shows a sudden increase up to −18 dB at the lowest 600 m which is a further indicator for the formation of needles or columnar crystals. The spectral width along this fall streak is generally low, shows a significant peak at 1 km and increases below 800 m. Doppler velocities fluctuate around $-0.8\,\mathrm{m\,s^{-1}}$.

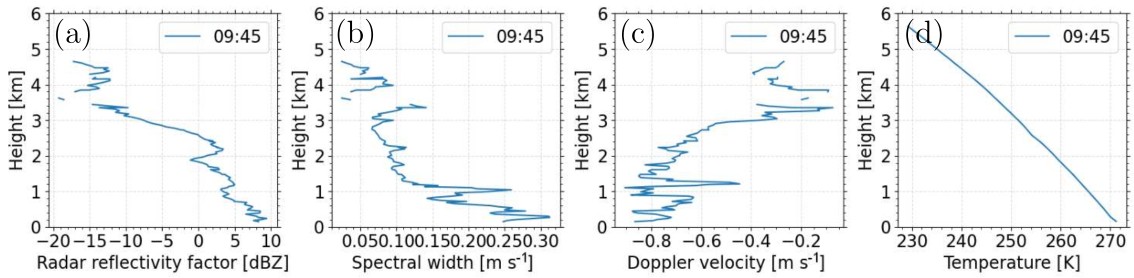

Figure 4.20: (a) Reflectivity of RPG94_LACROS plus 20 dB offset, (b) RPG94_LACROS spectral width, (c) Doppler velocity, and (d) ECMWF model temperature along the black fall streak in Fig. 4.19 (18 January 2023) which reaches the ground at 09:45 UTC.

For this case, the observed ice crystal shapes can be explained well by remote sensing measurements. Dendrites and plates were probably formed at altitudes of 2.2 km and higher, where the reflectivity increases downwards. Needles were formed or grew on already existing particles at 800 m and below.

4.3 Case studies: Precipitation monitoring during cloud seeding experiments

For a better understanding of cloud-microphysical processes, seeding experiments are conducted in the frame of Cloudlab and PolarCAP. During such experiments, a drone carrying seeding flares flies into a MPC. When the flares are combusted, aerosol particles are generated and may initiate ice crystal nucleation (Henneberger et al., 2023). Under suitable conditions, the ice particles then grow and start to precipitate. If the seeding location in the cloud was chosen accordingly, HOLIMO attached to the helikite (Ramelli et al., 2020) can observe the formed cloud-ice crystals, remote-sensing instruments can monitor potential changes in cloud properties, and in-situ instruments on the ground might even detect precipitation particles, if they reached the ground at the measurement site. The latter was the case on 25 January 2023 during two seeding experiments starting at 18:55 UTC and 19:48 UTC. The RPG_LACROS reflectivity and SLDR from 16:00 UTC to 21:00 UTC is shown in Fig. 4.21. The presence of a typical low-level stratiform Bise cloud offered excellent synoptic conditions for seeding experiments. The cloud consisted mainly of liquid water droplets, but on-again-off-again, ice crystals were formed at the cloud top which then grew on the expense of liquid water and caused an increase of radar reflectivity. The two seeding experiments are reflected in both increased reflectivity and SLDR for several minutes.

During the afternoon and evening on 25 January 2023, R determined from the 2DVD measurements (Fig. 4.22) shows two sudden increases, each only for two or three minutes, around 15 minutes after the start of each seeding event. The times of increased R are identical with those of increased reflectivity and SLDR in Fig. 4.21, which suggests that the formation of according particles detected by the 2DVD was initiated by the aerosols of the burning flares.

To analyse the precipitation induced by the seeding events, three time periods are investigated with a focus on detected particle shapes. The first period was chosen from 18:00 UTC to 19:00 UTC for a background reference to get information about hydrometeors precipitating without seeding impact. The second period from 19:10 UTC to 19:13 UTC and the third period from 20:00 UTC to 20:03 UTC cover the peaks in R after each seeding

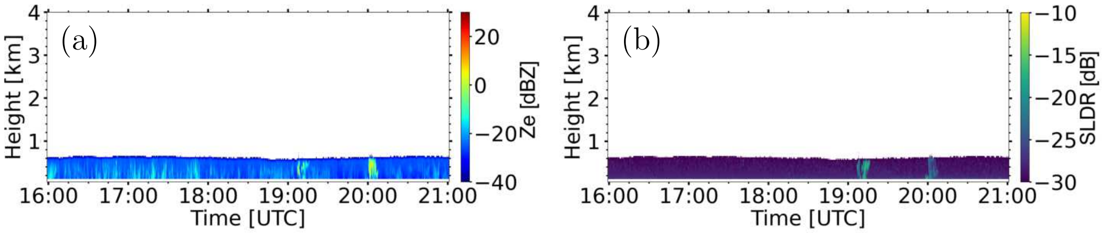

Figure 4.21: RPG94_LACROS (a) reflectivity and (b) SLDR of a typical Bise cloud on 25 January 2023. The formation of cloud ice is visible after the seeding events at 18:55 UTC and 19:48 UTC.

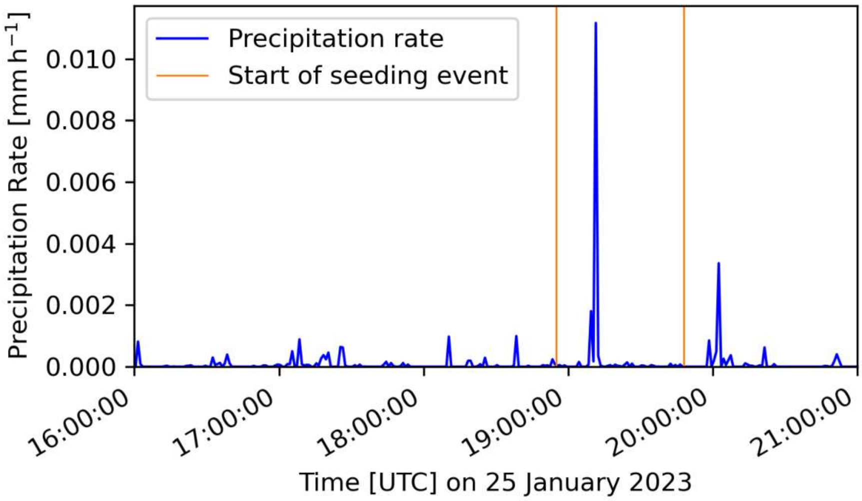

Figure 4.22: Precipitation rate determined by 2DVD data on 25 January 2023. An integration interval of 60 s was chosen and due to solid precipitation, a hydrometeor density of 0.9 g cm^{-3} was assumed. Orange lines indicate times of aerosol releases during cloud seeding experiments.

event. During the first period which is 60 minutes, the 2DVD detected only 51 particles. During the three-minute periods two and three, 235 and 176 particles were detected, respectively, which indicates the seeding impact on the precipitation. The relation of ν and D_{eq} for each particle of all three periods is shown in Fig. 4.23a, images of hydrometeors characteristic for the respective clusters are presented in Fig. 4.23b. Most of the particles that were observed during period one before the seeding events varied in D_{eq} from 0.2 mm to 0.3 mm and in ν from 0.75 m s^{-1} to 1.5 m s^{-1}.

Characteristic hydrometeors for that period indicate columns or needles as major particle type which mostly were rimed to some extent. This accounts for periods two and three as well, which is supported by SLDR values of up to around -15 dB. Further, a temperature sensor attached to the seeding drone measured -5°C during each flare combustion, which is a suitable environment for column and needle formation (Bailey and Hallett, 2009). However, the particles were much smaller with D_{eq} mostly below 0.2 mm and $\nu < 0.5$ m s^{-1} which may be due to a shorter residence time in the cloud. Particles observed in the first period could be larger because they might have stayed longer in the cloud due to turbulence, which also results in stronger riming and thus higher ν. The 2DVD results have again revealed that from the the instruments measurements, one can distinguish between ice crystal shapes and thus, the 2DVD can contribute to the investigation of aerosol-cloud-interaction if precipitating hydrometeors reach the ground.

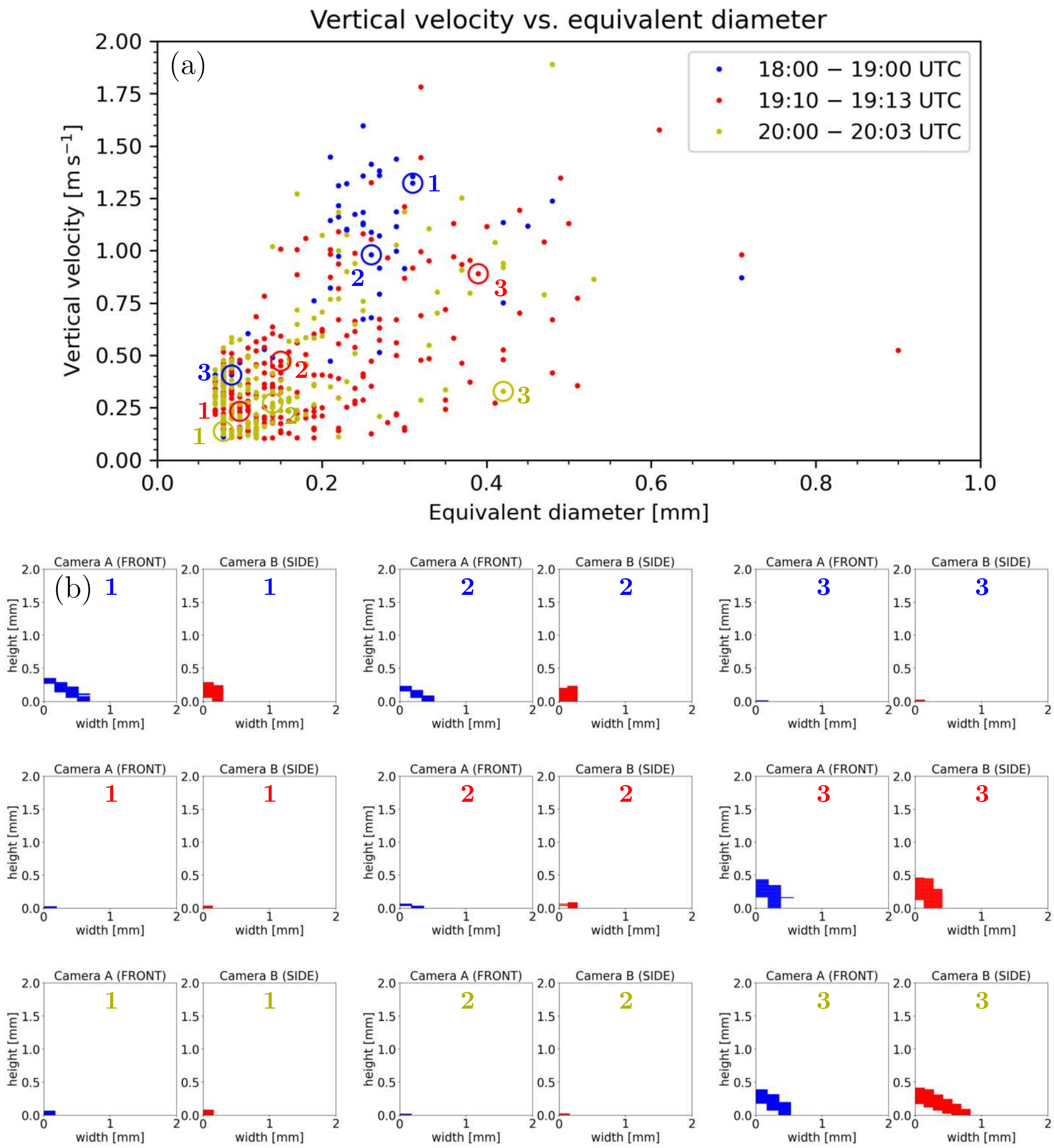

Figure 4.23: 2DVD measurements on 25 January 2023 at different time periods. (a) shows the v versus D_{eq} relation for all particles that were detected in the respective time period. (b) presents hydrometeors characteristic for the respective clusters in (a) from 18:00 UTC – 19:00 UTC (blue numbers), 19:10 UTC – 19:13 UTC (red numbers), and 20:00 UTC – 20:03 UTC (yellow numbers). The coloured numbers in (a) and (b) indicate the same hydrometeors. Total particle numbers are 51 (blue), 235 (red), and 176 (yellow).

Chapter 5

Discussion

A comparison of R of different instruments was done for a cold-rain and a warm-rain event on 5 January 2023. The separation into cold and warm rain was based on the presence of a melting layer which in turn was identified by RPG_LACROS Doppler velocity and SLDR (Fig. 4.2a, b). Presumably, this method cannot conclusively clarify whether a proportion of warm rain also contributed to precipitation during the cold-rain period or not. The weather station was running during that time period and has recorded precipitation on other days during the campaign. Thus, it remains unclear, why it has not detected any droplets on 5 January 2023. The PSDs of the 2DVD (Fig. 4.3) confirm, that during the cold-rain period partly larger droplets have been detected than during the warm-rain period, where most likely drizzle occurred.

Comparison studies about the 2DVD and the Parsivel^2 report that, at heavy rainfall, the Parsivel^2 tends to overestimate large particles with diameters larger than 3.5 mm (Liu et al., 2019) or 4 mm (Park et al., 2017) and to underestimate small droplets with a few 100 µm in diameter (e.g., Park et al., 2017). However, on 5 January, only light rain or drizzle was observed, so that those conditions do not apply. Wind speeds averaged per minute exceeded $10\,\mathrm{m\,s^{-1}}$ several times for single minutes during the cold-rain period. Up to this value, according to the manufacturer, the uncertainty specifications (Tbl. 2.2) are valid, which should be mentioned again at this point, although the effect is probably negligible. Nevertheless, wind speeds were generally slightly higher during the cold-rain period, which might have contributed to the difference in R.

The 2DVD measurement results in Sect. 4.2 show that it may depend on several factors, how well a particle type can be deduced from the two camera images. Plates or dendrites, for example, are only clearly recognisable as such if their width is at least 1 mm to 2 mm and only if they do not fall exactly horizontally but inclined through the virtual measuring area. Otherwise, they could appear as horizontal lines from both camera perspectives which would make a distinction from needles or columnar crystals more challenging. The latter usually appear as horizontal lines and often can be identified by different widths from the two camera perspectives. Columns or needles would only appear with the same length in both camera images if they are aligned in a 45° angle towards both cameras. Graupel usually does not show any sharp edges and appears rounded from both perspectives. Slightly rimed particles on the other hand seem to be hard to identify as such.

The analysis of 2DVD data in Sect. 4.2, especially during case 2 (Fig. 4.11) demonstrated that unrealistic particles are not filtered by the sno-algorithm of the manufacturer. Such particles are mainly vertically prolonged, oftentimes with long smooth edges (see App. C) and should therefore be filtered by adjusted sno-algorithm criteria.

The four cases presented in Sects. 4.2.1 to 4.2.4 were chosen according to the educated-eye protocol entries. This choice allowed the examination of in-situ measurement data containing information about differently shaped solid hydrometeors. During most of the time periods, a larger variety of shapes was measured by either the 2DVD or HOLIMO than was reported in the educated-eye protocol. Especially the "high number of dendrites" on 17 January 2023 at 14:07 UTC to 14:11 UTC could not be validated by the measurements. Presumably, larger particles were perceived disproportionately strongly by eye.

In Sect. 4.2 it was found that 2DVD and HOLIMO generally show good agreement. The type of some of the presented particles would most likely be identifiable as such if the particle would have been detected by the other instrument. However, the measurements of one of the instruments shows additional particle types. Figures 4.11 and 4.15 suggest that the number of dendrites and aggregates around 2 mm and larger increased within 15 minutes during that day which is supported by higher dendrite concentrations reported by the educated-eye protocol. HOLIMO on the other hand did not detect any dendrites during the third time period (Fig. 4.16) which could be caused by its detection limit of 2 mm.

The combination of remote-sensing signatures and the ECMWF model temperature along fall streaks proves helpful to understand the formation of different hydrometeor types and crystal shapes. In general, at height ranges where the reflectivity of RPG94_LACROS increases, particle growth or particle formation can be assumed. This is the case, for example, for the lowest 800 m at case 4 (Sect. 4.2.4). Only at this height range, ambient temperatures would allow the formation of needles, according to Bailey and Hallett (2009). In this case, increased SLDR values confirmed this theory. Further, a larger variety of particle shapes was detected by the in-situ instruments when values of the RPG94_LACROS spectral width near the ground were higher. When the spectral width increased at a certain height range, for example between 2.2 km and 1.8 km during case 2 (Sect. 4.2.2), the cause could be particle riming. The application of a liquid water layer detection algorithm might be helpful for further investigations to better understand particle formation along fall streaks.

The particle size in the 2DVD data is given by the manufacturer as equivalent diameter of a sphere with the same volume (D_{eq}). In case of solid particles, an expression of the size by means of maximum diameter would be advantageous to make the data better comparable with the results of other studies, for example, about velocity-size relationships of different ice crystal shapes (Locatelli and Hobbs, 1974; Barthazy and Schefold, 2006).

Section 4.3 provides a framework for a closure study of which important components were investigated, starting with ice nucleation and cloud development, up to the observation of particles on the ground. The measurements of the different instruments were consistent insomuch as they confirmed the theory of the formation of needles or columnar ice crystals and their subsequent partial riming. The 2DVD contributed decisively, as the precipitation signatures on the ground were well captured. Measurements from other instruments, e.g. Polly$^{\mathrm{XT}}$, should be included in the case study in order to better understand and quantify microphysical processes inside the cloud.

Furthermore, R of the 2DVD may currently be much affected by errors, because on the one hand, a particle density for a certain time interval has to be assumed with the presented calculation method. On the other hand, this density refers to the total particle volume detected by the 2DVD, which might partly be composed of air, since filigree structures cannot be resolved by the 2DVD. However, in the case of small needles or columns, this effect is be small, so that R in Sect. 4.3 should be reliable.

Chapter 6

Summary, Conclusions, and Outlook

In this thesis, the observation of precipitation with a 2DVD and other in-situ and remote-sensing instruments was investigated. Special focus was on the 2DVD as a ground-based in-situ instrument which detects single hydrometeors. The measurement principle, calibration procedure, data processing chain, and former 2DVD-related research was presented. The Cloudlab and PolarCAP measurement campaign in Switzerland was introduced, where data for this work were collected. The variety of instrumentation included in this campaign, from the holographic in-situ sonde HOLIMO and other ground-based in-situ sensors up to extensive remote-sensing instrumentation offered a unique framework to study cloud formation and development as well as precipitation evolution.

The performance of the 2DVD under different synoptic conditions could be evaluated against other in-situ sensors including HOLIMO. Precipitation rates of the LACROS in-situ instruments were compared for a warm-rain and cold-rain period. During snowfall events where different ice crystal shapes were observed, simultaneous HOLIMO measurements revealed strengths and weaknesses of the 2DVDs ability to distinguish different ice crystal shapes. A case study about a cloud seeding experiment eventually indicated that the 2DVD can be a valuable instrument for the investigation of cloud-aerosol-interaction with precipitation formation, because it can reliably cover precipitation monitoring on the ground.

In general, the objectives of this work have been achieved. The first goal was to get familiar with the 2DVD functioning. The measurement principle, data processing chain including different matching algorithms, and calibration procedure were studied and presented. During the calibration on 12 December 2022, inserting the smallest steel spheres with diameters of 0.5 mm was sometimes challenging, as they often clinged together due to electrostatics. Nevertheless, the calibration procedure proved reliable.

The second objective of this thesis was to characterise the 2DVD by means of available parameters describing precipitation and single particles. In this thesis, only hydrometeor parameters which are provided by the manufacturers software were used. This shows that the current status of software is sufficient enough to produce the presented measurement results. However, in former studies about the instrument, further parameters such as maximum diameter, perimeter, or bulk density (e.g., Grazioli et al., 2014; Bernauer et al., 2016; Zhang et al., 2021) were derived which might improve the data analysis.

Thirdly, the 2DVD should be evaluated under different synoptic conditions and against other precipitation sensors. Time periods with warm and cold rain for rain rate comparisons, as well as time periods with differently shaped precipitating ice particles could be investigated which allowed fruitful analyses. The rain rate comparison with the Parsivel[2] revealed good agreement, but the investigated time period does only allow to draw conclusions about the instrument performance for small droplets and drizzle. Convective rain events which produce larger droplets could not be monitored during the measurement campaign. The snow and graupel measurements on 17 and 18 January 2023 indicated, that the 2DVD can generally distinguish between different ice crystal shapes. Especially for particles of several millimeters in size, shapes could mostly be identified. However, if particles are only some 100 µm in size, one often has to speculate about the particle shape. Usually, pristine columns and needles with small sizes can be identified as well, as the measurements presented in Sect. 4.3 confirm too. However, the differentiation of dendrites, irregular particles, or aggregates with $D_{eq} < 1\,\mathrm{mm}$ by means of the camera images turned out to be challenging. For particles of such size, HOLIMO could reliably help to identify particle shapes. On the other hand, the small sample volume and the limited detectable particle size of HOLIMO do not allow the derivation of particle concentrations. The educated-eye helped to identify time periods with different dominating particle shapes. However, the results show that it most likely focused too much on larger particles that were clearly visible. Eventually, the study demonstrates the complementarity of educated-eye, 2DVD, and HOLIMO observations, because each of them served a certain purpose. The measurements of different ice crystals has also revealed that the 2DVD sno-algorithm provided by the manufacturer did not filter unrealistic particles which had an O of 2 and larger. Therefore, further data evaluation is necessary to adjust the sno-algorithm such that unrealistic particles are filtered.

The fourth goal of this work was to prove the 2DVD's ability to contribute to the investigation of cloud-microphysical processes. The results of the cloud seeding experiments presented in Sect. 4.3 clearly demonstrate, that the 2DVD delivered reliable information about the ground precipitation and allowed the determination of particle shapes. However, the columnar shape of the particles might have been advantageous, as previous results showed that other shapes are difficult to identify in case of such small particles.

The results of this thesis, as well as former 2DVD-related research studies indicate that the analysis of the instrument data still has potential and that an improvement could yield more detailed or accurate information about precipitation and single particles. It is necessary to investigate the snow bulk density for different particle types, shapes, and sizes to improve the accuracy of R at different conditions.

With regard to the differentiation of ice crystal types, further precipitation events with higher percentages of one dominating shape should be identified and analysed in order to allow a better interpretation of 2DVD signatures. In a following step, the development of an automatic particle classification algorithm would be advantageous to investigate differently shaped particles separately from each other. This could possibly be achieved by applying a machine learning algorithm to a suitable dataset.

The determination of the radar reflectivity from the 2DVD data, as already done in many studies (see Sect. 2.3.3), should be included in future data analysis in order to allow better comparisons with remote-sensing measurements. This would also enable a better interpretation of remote-sensing signatures by 2DVD data, which has potential to be expanded in the future.

Finally, further datasets of the 2DVD are available, for example, from the Multidisciplinary drifting Observatory for the Study of Arctic Climate (MOSAiC) expedition (Shupe et al., 2022) or from PolarCAP 2023/24, which can be evaluated with regard to the different aspects mentioned above.

Appendix A

2DVD data processing chain

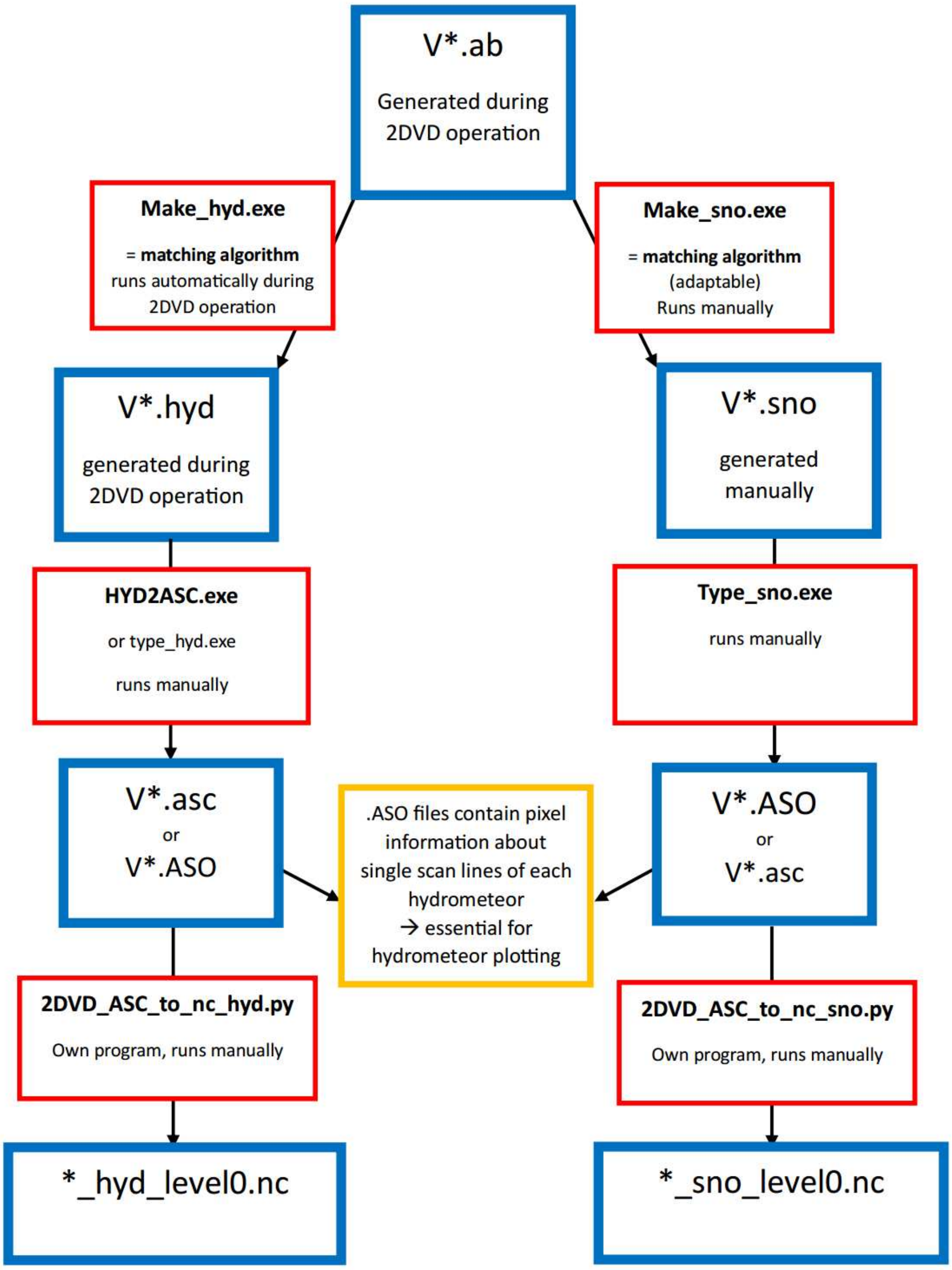

Figure A.1: Data processing chain of the 2DVD raw data. Blue boxes indicate files, red boxes indicate programs.

Appendix B

Calibration offset between Mira-35 and RPG94_LACROS

Due to an outage of the RPG94_LACROS blower system on 17 and 18 January 2023, snow accumulation occurred on the radome sheets. Thus, the reflectivity offset to Mira-35 needs to be determined to revise the RPG94_LACROS data. The offset was calculated as described below.

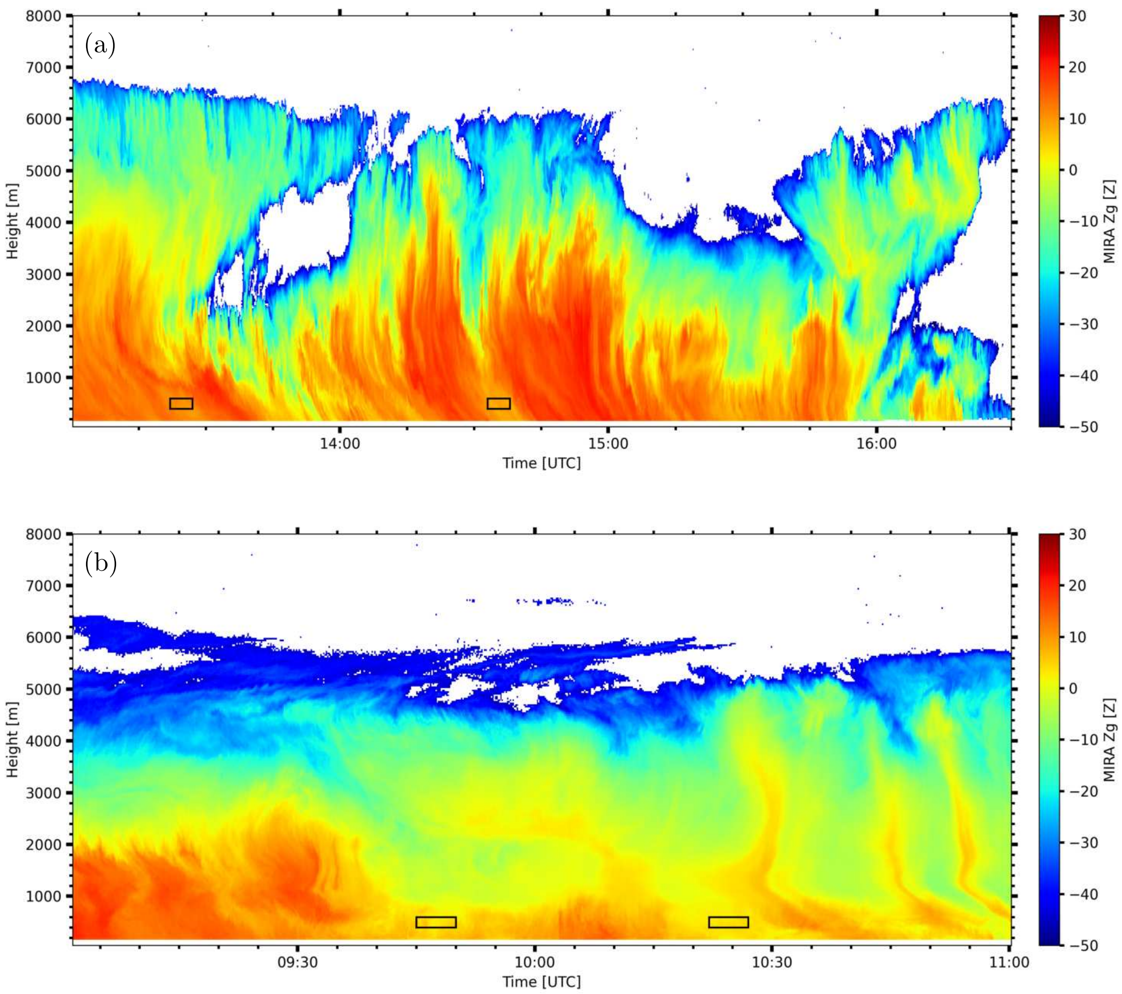

Figure B.1: Radar reflectivities measured by Mira-35 on (a) 17 and (b) 18 January 2023. The black rectangles indicate time periods and height ranges that are taken into account for RPG94_LACROS offset calculation.

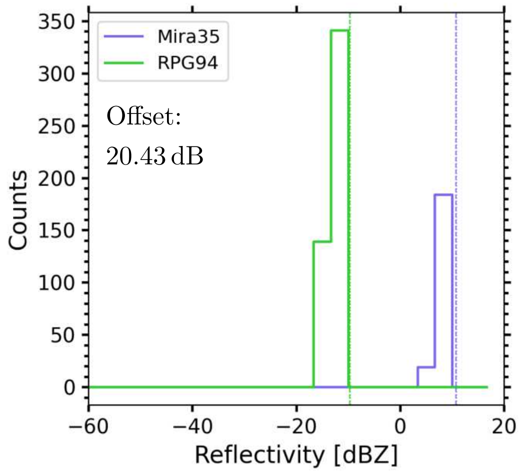

(a) 17 Jan 2023, 13:22 – 13:27 UTC

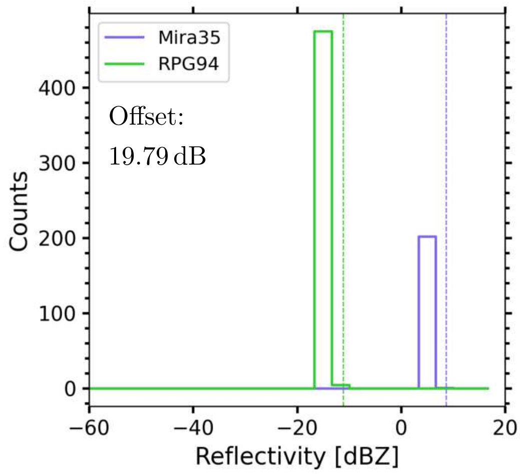

(b) 17 Jan 2023, 14:33 – 14:38 UTC

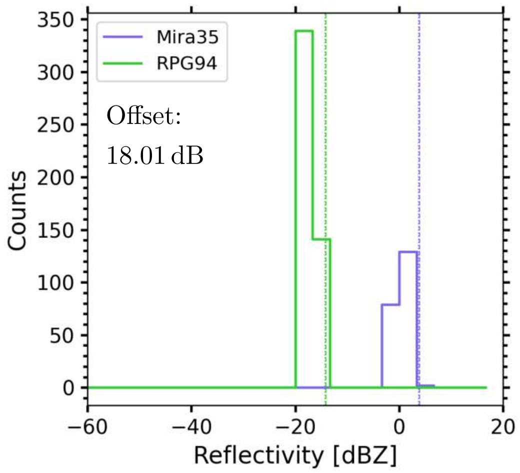

(c) 18 Jan 2023, 09:45 – 09:50 UTC

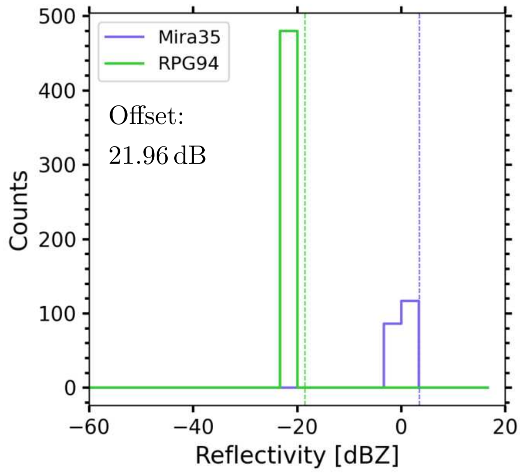

(d) 18 Jan 2023, 10:22 – 10:27 UTC

Figure B.2: Histograms of measured radar reflectivities for different time periods which are indicated by the subcaptions. Dotted lines show the mean reflectivity detected by the respective instrument. The shown offset represents the difference of Mira-35 and RPG94 mean reflectivities.

For four time periods, two on 17 and two on 18 January, the mean reflectivities of both instruments were calculated within the height range of 400 m and 600 m. Figure B.1 presents Mira-35 reflectivities for both days with indicated time periods for the offset calculation. For each time period, the difference in mean reflectivity between Mira-35 and RPG94_LACROS was determined (Fig. B.2) and an approximate average offset of 20 dB for both days was found.

The height range and time periods were selected according to the following criteria. Firstly, reflectivities should not exceed 10 dBZ as the offset may be biased by saturation effects otherwise. Secondly, the reflectivities for one time period and height range should be as homogeneous as possible. Thirdly, the height range was chosen to be 400 m to 600 m to ensure a complete overlap between radar pulse and telescope field of view on the one hand and to avoid signal attenuation as much as possible on the other hand.

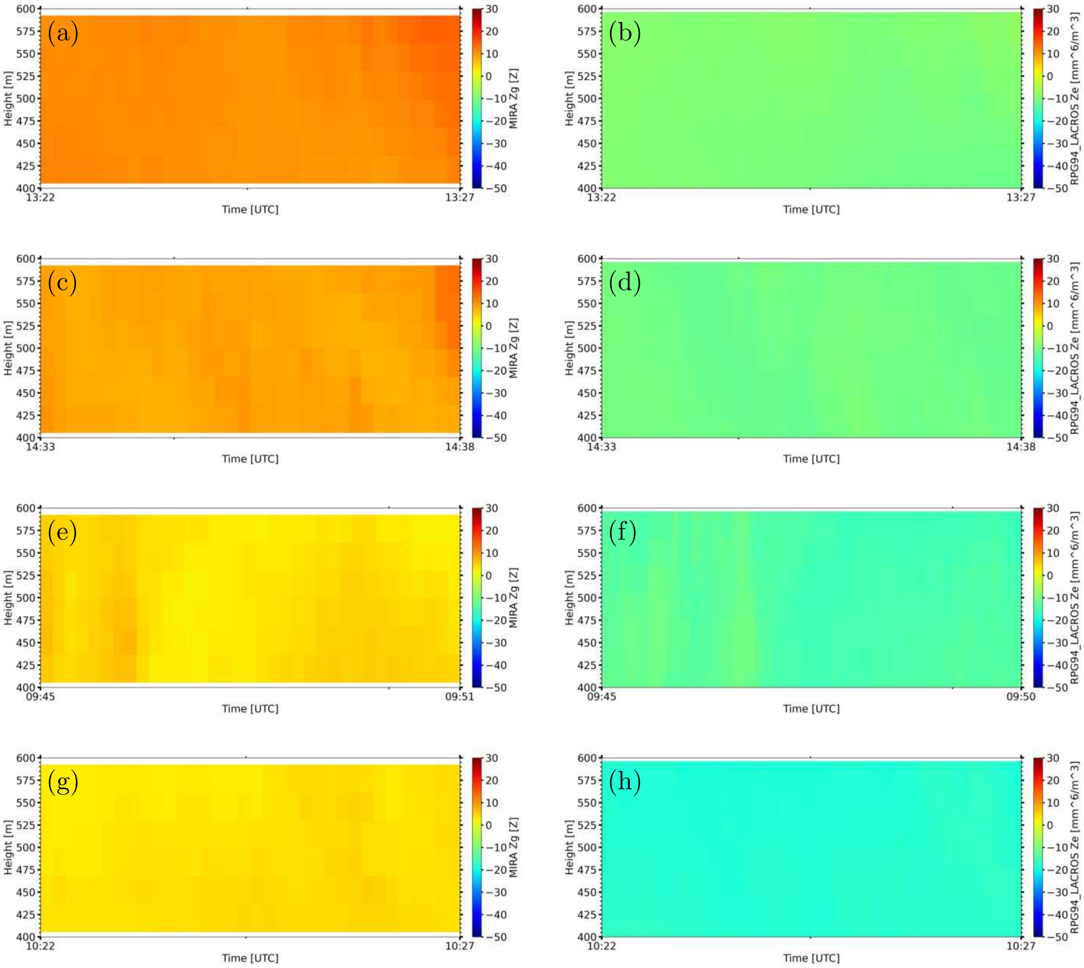

Figure B.3: Measured radar reflectivities by Mira-35 (left) and RPG94_LACROS (right) from 400 m to 600 m above ground. The subfigures represent the time periods from 13:22 – 13:27 UTC (a, b) and 14:33 – 14:38 UTC (c, d) on 17 January 2023, and 09:45 – 09:50 UTC (e, f) and 10:22 – 10:27 UTC (g, h) on 18 January 2023.

Appendix C

Unrealistic particles not filtered by the 2DVD sno-algorithm

The following images contain 2DVD particles supposed by the sno-algorithm of the manufacturer which are most likely unreal.

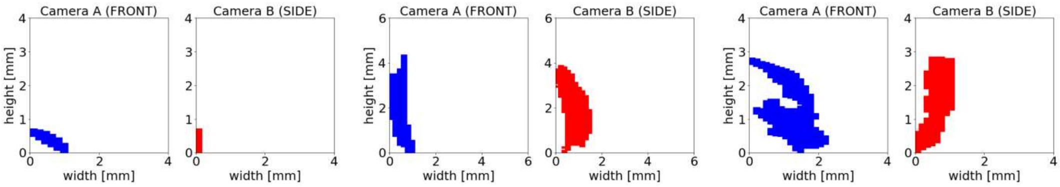

(a) 17 January 2023, 11:30 UTC – 11:35 UTC

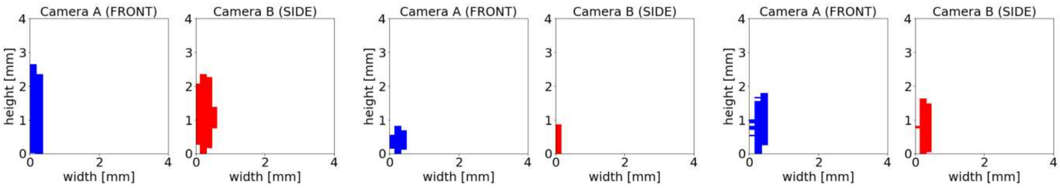

(b) 17 January 2023, 13:50 UTC – 13:54 UTC

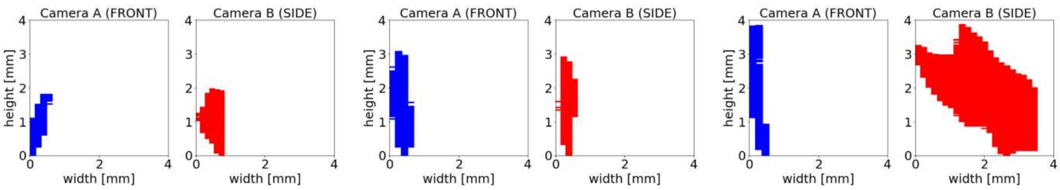

(c) 17 January 2023, 14:07 UTC – 14:11 UTC

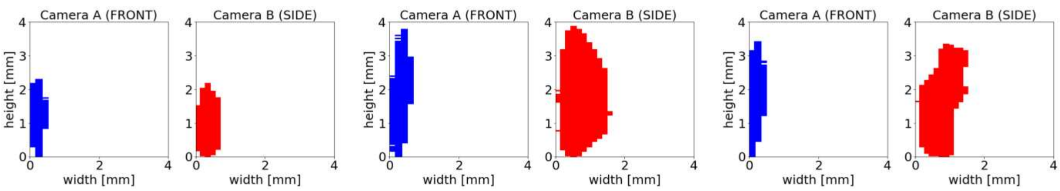

(d) 18 January 2023, 09:44 UTC – 09:48 UTC

Figure C.1: Selection of Particles from the four investigated time periods in Sect. 4.2 which are most likely unreal.

Bibliography

Adirosi, E., Volpi, E., Lombardo, F., and Baldini, L. Raindrop size distribution: Fitting performance of common theoretical models. *Advances in Water Resources*, 96:290–305, 2016. ISSN 0309-1708. doi: 10.1016/j.advwatres.2016.07.010.

Adirosi, E., Baldini, L., and Tokay, A. Rainfall and DSD Parameters Comparison between Micro Rain Radar, Two-Dimensional Video and Parsivel2 Disdrometers, and S-Band Dual-Polarization Radar. *Journal of Atmospheric and Oceanic Technology*, 37(4):621–640, 2020. ISSN 1520-0426. doi: 10.1175/jtech-d-19-0085.1.

Anagnostou, E. N., Anagnostou, M. N., Krajewski, W. F., Kruger, A., and Miriovsky, B. J. High-Resolution Rainfall Estimation from X-Band Polarimetric Radar Measurements. *Journal of Hydrometeorology*, 5(1):110–128, 2004. ISSN 1525-7541. doi: 10.1175/1525-7541(2004)005⟨0110:hrefxp⟩2.0.co;2.

Atlas, D., Srivastava, R. C., and Sekhon, R. S. Doppler radar characteristics of precipitation at vertical incidence. *Reviews of Geophysics*, 11(1):1–35, 1973. ISSN 1944-9208. doi: 10.1029/rg011i001p00001.

Bailey, M. P. and Hallett, J. A Comprehensive Habit Diagram for Atmospheric Ice Crystals: Confirmation from the Laboratory, AIRS II, and Other Field Studies. *Journal of the Atmospheric Sciences*, 66(9):2888–2899, 2009. doi: 10.1175/2009jas2883.1.

Baquero, M., Cruz-Pol, S., Bringi, V., and Chandrasekar, V. Use of Disdrometer Data for X-Band Polarimetric Radar Simulation and Tropical Rain Characterization. In *2006 IEEE International Symposium on Geoscience and Remote Sensing*. IEEE, 2006. doi: 10.1109/igarss.2006.492.

Barthazy, E. and Schefold, R. Fall velocity of snowflakes of different riming degree and crystal types. *Atmospheric Research*, 82(1–2):391–398, 2006. ISSN 0169-8095. doi: 10.1016/j.atmosres.2005.12.009.

Battaglia, A., Rustemeier, E., Tokay, A., Blahak, U., and Simmer, C. PARSIVEL Snow Observations: A Critical Assessment. *Journal of Atmospheric and Oceanic Technology*, 27(2):333–344, 2010. ISSN 0739-0572. doi: 10.1175/2009jtecha1332.1.

Baumgardner, D., Kok, G., Dawson, W., O'Connor, D., and Newton, R. A new ground-based precipitation spectrometer: The Meteorological Particle Sensor (MPS). In *Proceedings of the 11th Conference on Cloud Physics, Ogden, UT, USA*, pages 3–7, 2002.

Baumgardner, D., Avallone, L., Bansemer, A., Borrmann, S., Brown, P., Bundke, U., Chuang, P. Y., Cziczo, D., Field, P., Gallagher, M., Gayet, J.-F., Heymsfield, A., Korolev, A., Krämer, M., McFarquhar, G., Mertes, S., Möhler, O., Lance, S., Lawson, P., Petters, M. D., Pratt, K., Roberts, G., Rogers, D., Stetzer, O., Stith, J., Strapp, W., Twohy, C., and Wendisch, M. In Situ, Airborne Instrumentation: Addressing and Solving Measurement Problems in Ice Clouds. *Bulletin of the American Meteorological Society*, 93(2):ES29–ES34, 2012. doi: 10.1175/bams-d-11-00123.1.

Bergeron, T. On the physics of clouds and precipitation, Proces Verbaux de l'Association de Météorologie, International Union of Geodesy and Geophysics, 1935.

Bernauer, F., Hürkamp, K., Rühm, W., and Tschiersch, J. On the consistency of 2-D video disdrometers in measuring microphysical parameters of solid precipitation. *Atmospheric Measurement Techniques*, 8(8):3251–3261, 2015. doi: 10.5194/amt-8-3251-2015.

Bernauer, F., Hürkamp, K., Rühm, W., and Tschiersch, J. Snow event classification with a 2D video disdrometer — A decision tree approach. *Atmospheric Research*, 172–173: 186–195, 2016. ISSN 0169-8095. doi: 10.1016/j.atmosres.2016.01.001.

Boser, B. E., Guyon, I. M., and Vapnik, V. N. A training algorithm for optimal margin classifiers. In *Proceedings of the fifth annual workshop on Computational learning theory*, COLT92. ACM, 1992. doi: 10.1145/130385.130401.

Boucher, O., Randall, D., Artaxo, P., Bretherton, C., Feingold, G., Forster, P., Kerminen, V.-M., Kondo, Y., Liao, H., Lohmann, U., Rasch, P., Satheesh, S. K., Sherwood, S., Stevens, B., and Zhang, X. Y. *Clouds and aerosols*, pages 571–657. Cambridge University Press, Cambridge, UK, 2013. doi: 10.1017/CBO9781107415324.016.

Brandes, E. A., Zhang, G., and Vivekanandan, J. An Evaluation of a Drop Distribution–Based Polarimetric Radar Rainfall Estimator. *Journal of Applied Meteorology*, 42(5):652–660, 2003. ISSN 1520-0450. doi: 10.1175/1520-0450(2003)042⟨0652:aeoadd⟩2.0.co;2.

Brandes, E. A., Zhang, G., and Vivekanandan, J. Drop Size Distribution Retrieval with Polarimetric Radar: Model and Application. *Journal of Applied Meteorology*, 43(3):461–475, 2004. ISSN 1520-0450. doi: 10.1175/1520-0450(2004)043⟨0461:dsdrwp⟩2.0.co;2.

Brandes, E. A., Zhang, G., and Sun, J. On the Influence of Assumed Drop Size Distribution Form on Radar-Retrieved Thunderstorm Microphysics. *Journal of Applied Meteorology and Climatology*, 45(2):259–268, 2006. ISSN 1558-8424. doi: 10.1175/jam2335.1.

Brandes, E. A., Ikeda, K., Zhang, G., Schönhuber, M., and Rasmussen, R. M. A Statistical and Physical Description of Hydrometeor Distributions in Colorado Snowstorms Using a Video Disdrometer. *Journal of Applied Meteorology and Climatology*, 46(5):634–650, 2007. ISSN 1558-8424. doi: 10.1175/jam2489.1.

Brandes, E. A., Ikeda, K., Thompson, G., and Schönhuber, M. Aggregate Terminal Velocity/Temperature Relations. *Journal of Applied Meteorology and Climatology*, 47 (10):2729–2736, 2008. ISSN 1558-8424. doi: 10.1175/2008jamc1869.1.

Bringi, V., Thurai, M., and Baumgardner, D. Raindrop fall velocities from an optical array probe and 2-D video disdrometer. *Atmospheric Measurement Techniques*, 11(3): 1377–1384, 2018. ISSN 1867-8548. doi: 10.5194/amt-11-1377-2018.

Bringi, V. M. and Hubbert, J. *Validation of Polarimetric Radar Signatures Using the 2D-Video Distrometer*. 1997. doi: 10.21236/ada334153.

Bringi, V. N., Chandrasekar, V., Hubbert, J., Gorgucci, E., Randeu, W. L., and Schoenhuber, M. Raindrop Size Distribution in Different Climatic Regimes from Disdrometer and Dual-Polarized Radar Analysis. *Journal of the Atmospheric Sciences*, 60(2):354–365, 2003. ISSN 1520-0469. doi: 10.1175/1520-0469(2003)060⟨0354:rsdidc⟩2.0.co;2.

Bringi, V. N., Thurai, M., Nakagawa, K., Huang, G. J., Kobayashi, T., Adachi, A., Hanado, H., and Sekizawa, S. Rainfall Estimation from C-Band Polarimetric Radar in Okinawa, Japan: Comparisons with 2D-Video Disdrometer and 400 MHz Wind Profiler. *Journal of the Meteorological Society of Japan. Ser. II*, 84(4):705–724, 2006. ISSN 2186-9057. doi: 10.2151/jmsj.84.705.

Bühl, J., Seifert, P., Wandinger, U., Baars, H., Kanitz, T., Schmidt, J., Myagkov, A., Engelmann, R., Skupin, A., Heese, B., Klepel, A., Althausen, D., and Ansmann, A. LACROS: the Leipzig Aerosol and Cloud Remote Observations System. In Comeron, A., Kassianov, E. I., Schäfer, K., Stein, K., and Gonglewski, J. D., editors, *SPIE Proceedings*. SPIE, 2013. doi: 10.1117/12.2030911.

Bühl, J., Seifert, P., Radenz, M., Baars, H., and Ansmann, A. Ice crystal number concentration from lidar, cloud radar and radar wind profiler measurements. *Atmospheric Measurement Techniques*, 12(12):6601–6617, 2019. doi: 10.5194/amt-12-6601-2019.

Bukovčić, P., Zrnić, D., and Zhang, G. Winter Precipitation Liquid–Ice Phase Transitions Revealed with Polarimetric Radar and 2DVD Observations in Central Oklahoma. *Journal of Applied Meteorology and Climatology*, 56(5):1345–1363, 2017. ISSN 1558-8432. doi: 10.1175/jamc-d-16-0239.1.

Bukovčić, P., Ryzhkov, A. V., and Carlin, J. T. Polarimetric Radar Relations for Estimation of Visibility in Aggregated Snow. *Journal of Atmospheric and Oceanic Technology*, 38(4):805–822, 2021. ISSN 1520-0426. doi: 10.1175/jtech-d-20-0088.1.

Bukovčić, P., Zrnić, D., and Zhang, G. Convective–stratiform separation using video disdrometer observations in central Oklahoma – the Bayesian approach. *Atmospheric Research*, 155:176–191, 2015. ISSN 0169-8095. doi: 10.1016/j.atmosres.2014.12.002.

Bühl, J., Seifert, P., Myagkov, A., and Ansmann, A. Measuring ice- and liquid-water properties in mixed-phase cloud layers at the Leipzig Cloudnet station. *Atmospheric Chemistry and Physics*, 16(16):10609–10620, 2016. ISSN 1680-7324. doi: 10.5194/acp-16-10609-2016.

Cao, Q. and Zhang, G. Errors in Estimating Raindrop Size Distribution Parameters Employing Disdrometer and Simulated Raindrop Spectra. *Journal of Applied Meteorology and Climatology*, 48(2):406–425, 2009. ISSN 1558-8424. doi: 10.1175/2008jamc2026.1.

Cao, Q., Zhang, G., Brandes, E., Schuur, T., Ryzhkov, A., and Ikeda, K. Analysis of Video Disdrometer and Polarimetric Radar Data to Characterize Rain Microphysics in Oklahoma. *Journal of Applied Meteorology and Climatology*, 47(8):2238–2255, 2008. ISSN 1558-8424. doi: 10.1175/2008jamc1732.1.

Caracciolo, C., Prodi, F., and Uijlenhoet, R. Comparison between Pludix and impact/optical disdrometers during rainfall measurement campaigns. *Atmospheric Research*, 82(1–2):137–163, 2006. ISSN 0169-8095. doi: 10.1016/j.atmosres.2005.09.007.

Cauteruccio, A., Stagnaro, M., Lanza, L. G., and Chan, P.-W. Adjustment of 1 min rain gauge time series using co-located drop size distribution and wind speed measurements. *Atmospheric Measurement Techniques*, 16(17):4155–4163, 2023. ISSN 1867-8548. doi: 10.5194/amt-16-4155-2023.

Chang, W.-Y., Wang, T.-C. C., and Lin, P.-L. Characteristics of the Raindrop Size Distribution and Drop Shape Relation in Typhoon Systems in the Western Pacific from the 2D Video Disdrometer and NCU C-Band Polarimetric Radar. *Journal of Atmospheric and Oceanic Technology*, 26(10):1973–1993, 2009. ISSN 0739-0572. doi: 10.1175/2009jtecha1236.1.

Chang, W.-Y., Lee, G., Jou, B. J.-D., Lee, W.-C., Lin, P.-L., and Yu, C.-K. Uncertainty in Measured Raindrop Size Distributions from Four Types of Collocated Instruments. *Remote Sensing*, 12(7):1167, 2020. ISSN 2072-4292. doi: 10.3390/rs12071167.

Chen, J.-Y., Chang, W.-Y., and Chang, P.-L. A Synthetic Quantitative Precipitation Estimation by Integrating S- and C-Band Dual-Polarization Radars over Northern Taiwan. *Remote Sensing*, 13(1):154, 2021. ISSN 2072-4292. doi: 10.3390/rs13010154.

Costa, A., Meyer, J., Afchine, A., Luebke, A., Günther, G., Dorsey, J. R., Gallagher, M. W., Ehrlich, A., Wendisch, M., Baumgardner, D., Wex, H., and Krämer, M. Classification of Arctic, midlatitude and tropical clouds in the mixed-phase temperature regime. *Atmospheric Chemistry and Physics*, 17(19):12219–12238, 2017. doi: 10.5194/acp-17-12219-2017.

Das, S. K., Simon, S., Kolte, Y. K., Krishna, U. V. M., Deshpande, S. M., and Hazra, A. Investigation of Raindrops Fall Velocity During Different Monsoon Seasons Over the Western Ghats, India. *Earth and Space Science*, 7(2), 2020. ISSN 2333-5084. doi: 10.1029/2019ea000956.

Diederich, M., Crewell, S., Simmer, C., and Uijlenhoet, R. Investigation of rainfall microstructure and variability using vertically pointing radar and disdrometer. In *European Conference on Radar in Meteorology and Hydrology (ERAD), Visby, 6-10 September 2004*, pages 80–86, 2004.

Douville, H., Raghavan, K., Renwick, J., Allan, R. P., Arias, P. A., Barlow, M., Cerezo-Mota, R., Cherchi, A., Gan, T. Y., Gergis, J., Jiang, D., Khan, A., Pokam Mba, W., Rosenfeld, D., Tierney, J., and Zolina, O. *Water Cycle Changes*, page 1055–1210. Cambridge University Press, Cambridge, United Kingdom and New York, NY, USA, 2021. doi: 10.1017/9781009157896.010.

D'Adderio, L. P., Vulpiani, G., Porcù, F., Tokay, A., and Meneghini, R. Comparison of GPM Core Observatory and Ground-Based Radar Retrieval of Mass-Weighted Mean Raindrop Diameter at Midlatitude. *Journal of Hydrometeorology*, 19(10):1583–1598, 2018. ISSN 1525-7541. doi: 10.1175/jhm-d-18-0002.1.

Feng, L., Liu, X., Xiao, H., Xiao, L., Xia, F., Hao, X., Lu, H., and Zhang, C. Characteristics of Raindrop Size Distribution in Typhoon Nida (2016) before and after Landfall in Southern China from 2D Video Disdrometer Data. *Advances in Meteorology*, 2021: 1–14, 2021. ISSN 1687-9309. doi: 10.1155/2021/9349738.

Findeisen, W. Kolloid-meteorologische Vorgänge bei Niederschlags-bildung. *Meteorol. Z*, 55:121–133, 1938.

Forster, P., Storelvmo, T., Armour, K., Collins, W., Dufresne, J.-L., Frame, D., Lunt, D. J., Mauritsen, T., Palmer, M. D., Watanabe, M., Wild, M., and Zhang, H. *The Earth's Energy Budget, Climate Feedbacks, and Climate Sensitivity*, page 923–1054. Cambridge University Press, Cambridge, United Kingdom and New York, NY, USA, 2021. doi: 10.1017/9781009157896.009.

Garrett, T. J., Fallgatter, C., Shkurko, K., and Howlett, D. Fall speed measurement and high-resolution multi-angle photography of hydrometeors in free fall. *Atmospheric Measurement Techniques*, 5(11):2625–2633, 2012. ISSN 1867-8548. doi: 10.5194/amt-5-2625-2012.

Gatlin, P. N., Thurai, M., Bringi, V. N., Petersen, W., Wolff, D., Tokay, A., Carey, L., and Wingo, M. Searching for Large Raindrops: A Global Summary of Two-Dimensional Video Disdrometer Observations. *Journal of Applied Meteorology and Climatology*, 54 (5):1069–1089, 2015. ISSN 1558-8432. doi: 10.1175/jamc-d-14-0089.1.

Gavrilov, S., Kubo, M., Tran, V. A., Ngo, D. L., Nguyen, N. G., Nguyen, L. A. T., Lumbanraja, F. R., Phan, D., and Satou, K. Feature Analysis and Classification of Particle Data from Two-Dimensional Video Disdrometer. *Advances in Remote Sensing*, 04(01):1–14, 2015. ISSN 2169-2688. doi: 10.4236/ars.2015.41001.

Gires, A., Tchiguirinskaia, I., Schertzer, D., and Berne, A. 2DVD Data Revisited: Multifractal Insights into Cuts of the Spatiotemporal Rainfall Process. *Journal of Hydrometeorology*, 16(2):548–562, 2015. ISSN 1525-7541. doi: 10.1175/jhm-d-14-0127.1.

Grazioli, J., Tuia, D., Monhart, S., Schneebeli, M., Raupach, T., and Berne, A. Hydrometeor classification from two-dimensional video disdrometer data. *Atmospheric Measurement Techniques*, 7(9):2869–2882, 2014. ISSN 1867-8548. doi: 10.5194/amt-7-2869-2014.

Guichard, F. and Couvreux, F. A short review of numerical cloud-resolving models. *Tellus A: Dynamic Meteorology and Oceanography*, 69(1):1373578, 2017. doi: 10.1080/16000870.2017.1373578.

Habib, E. and Krajewski, W. F. An example of computational approach used for aerodynamic design of a rain disdrometer. *Journal of Hydraulic Research*, 39(4):425–428, 2001. ISSN 1814-2079. doi: 10.1080/00221680109499846.

Hanesch, M. *Fall velocity and shape of snowflakes*. PhD thesis, 1999.

Hauser, D., Amayenc, P., Nutten, B., and Waldteufel, P. A New Optical Instrument for Simultaneous Measurement of Raindrop Diameter and Fall Speed Distributions. *Journal of Atmospheric and Oceanic Technology*, 1(3):256–269, 1984. ISSN 1520-0426. doi: 10.1175/1520-0426(1984)001⟨0256:anoifs⟩2.0.co;2.

Helms, C. N., Munchak, S. J., Tokay, A., and Pettersen, C. A comparative evaluation of snowflake particle shape estimation techniques used by the Precipitation Imaging Package (PIP), Multi-Angle Snowflake Camera (MASC), and Two-Dimensional Video Disdrometer (2DVD). *Atmospheric Measurement Techniques*, 15(22):6545–6561, 2022. ISSN 1867-8548. doi: 10.5194/amt-15-6545-2022.

Henneberger, J., Fugal, J. P., Stetzer, O., and Lohmann, U. HOLIMO II: a digital holographic instrument for ground-based in situ observations of microphysical properties of mixed-phase clouds. *Atmospheric Measurement Techniques*, 6(11):2975–2987, 2013. doi: 10.5194/amt-6-2975-2013.

Henneberger, J., Ramelli, F., Spirig, R., Omanovic, N., Miller, A. J., Fuchs, C., Zhang, H., Bühl, J., Hervo, M., Kanji, Z. A., Ohneiser, K., Radenz, M., Rösch, M., Seifert, P., and Lohmann, U. Seeding of Supercooled Low Stratus Clouds with a UAV to Study Microphysical Ice Processes: An Introduction to the CLOUDLAB Project. *Bulletin of the American Meteorological Society*, 104(11):E1962–E1979, 2023. ISSN 1520-0477. doi: 10.1175/bams-d-22-0178.1.

Huang, G.-J., Bringi, V. N., and Thurai, M. Orientation Angle Distributions of Drops after an 80-m Fall Using a 2D Video Disdrometer. *Journal of Atmospheric and Oceanic Technology*, 25(9):1717–1723, 2008. ISSN 0739-0572. doi: 10.1175/2008jtecha1075.1.

Huang, G.-J., Bringi, V. N., Cifelli, R., Hudak, D., and Petersen, W. A. A Methodology to Derive Radar Reflectivity–Liquid Equivalent Snow Rate Relations Using C-Band Radar and a 2D Video Disdrometer. *Journal of Atmospheric and Oceanic Technology*, 27(4):637–651, 2010. ISSN 0739-0572. doi: 10.1175/2009jtecha1284.1.

Huang, G.-J., Bringi, V. N., Moisseev, D., Petersen, W. A., Bliven, L., and Hudak, D. Use of 2D-video disdrometer to derive mean density–size and Ze–SR relations: Four snow cases from the light precipitation validation experiment. *Atmospheric Research*, 153:34–48, 2015. ISSN 0169-8095. doi: 10.1016/j.atmosres.2014.07.013.

Ibrahim, I. A., Chandrasekar, V., Bringi, V. N., Kennedy, P. C., Schönhuber, M., Urban, H. E., and Randen, W. L. Simultaneous multiparameter radar and 2D-video disdrometer observations of snow. In *IGARSS '98. Sensing and Managing the Environment. 1998 IEEE International Geoscience and Remote Sensing. Symposium Proceedings. (Cat. No.98CH36174)*. IEEE, 1998. doi: 10.1109/igarss.1998.702931.

Joss, J. and Waldvogel, A. Ein Spektrograph für Niederschlagstropfen mit automatischer Auswertung. *Pure and Applied Geophysics PAGEOPH*, 68(1):240–246, 1967. ISSN 1420-9136. doi: 10.1007/bf00874898.

Kalogiros, J., Anagnostou, M. N., Anagnostou, E. N., Montopoli, M., Picciotti, E., and Marzano, F. S. Evaluation of a New Polarimetric Algorithm for Rain-Path Attenuation Correction of X-Band Radar Observations Against Disdrometer. *IEEE Transactions on Geoscience and Remote Sensing*, 52(2):1369–1380, 2014. ISSN 1558-0644. doi: 10.1109/tgrs.2013.2250979.

Kärcher, B. A parameterization of cirrus cloud formation: Homogeneous freezing of supercooled aerosols. *Journal of Geophysical Research*, 107(D2), 2002. doi: 10.1029/2001jd000470.

Kim, H.-L., Suk, M.-K., Park, H.-S., Lee, G.-W., and Ko, J.-S. Dual-polarization radar rainfall estimation in Korea according to raindrop shapes obtained by using a 2-D video disdrometer. *Atmospheric Measurement Techniques*, 9(8):3863–3878, 2016. ISSN 1867-8548. doi: 10.5194/amt-9-3863-2016.

Kim, H.-L., Jung, S.-H., and Jang, K.-I. Estimating Rain Microphysical Characteristics Using S-Band Dual-Polarization Radar in South Korea. *Journal of Atmospheric and Oceanic Technology*, 37(6):1067–1084, 2020. ISSN 1520-0426. doi: 10.1175/jtech-d-19-0068.1.

Kneifel, S., Löhnert, U., Battaglia, A., Crewell, S., and Siebler, D. Snow scattering signals in ground-based passive microwave radiometer measurements. *Journal of Geophysical Research: Atmospheres*, 115(D16), 2010. ISSN 0148-0227. doi: 10.1029/2010jd013856.

Korolev, A. and Leisner, T. Review of experimental studies of secondary ice production. *Atmospheric Chemistry and Physics*, 20(20):11767–11797, 2020. doi: 10.5194/acp-20-11767-2020.

Krajewski, W. F., Kruger, A., Caracciolo, C., Golé, P., Barthes, L., Creutin, J.-D., Delahaye, J.-Y., Nikolopoulos, E. I., Ogden, F., and Vinson, J.-P. DEVEX-disdrometer evaluation experiment: Basic results and implications for hydrologic studies. *Advances in Water Resources*, 29(2):311–325, 2006. ISSN 0309-1708. doi: 10.1016/j.advwatres.2005.03.018.

Kruger, A. and Krajewski, W. F. Two-Dimensional Video Disdrometer: A Description. *Journal of Atmospheric and Oceanic Technology*, 19(5):602–617, 2002. doi: 10.1175/1520-0426(2002)019⟨0602:tdvdad⟩2.0.co;2.

Larsen, M. and Schönhuber, M. Identification and Characterization of an Anomaly in Two-Dimensional Video Disdrometer Data. *Atmosphere*, 9(8):315, 2018. ISSN 2073-4433. doi: 10.3390/atmos9080315.

Larsen, M. L. and Blouin, C. K. Refinements to Data Acquired by 2-Dimensional Video Disdrometers. *Atmosphere*, 11(8):855, 2020. ISSN 2073-4433. doi: 10.3390/atmos11080855.

Larsen, M. L., Kostinski, A. B., and Tokay, A. Observations and Analysis of Uncorrelated Rain. *Journal of the Atmospheric Sciences*, 62(11):4071–4083, 2005. ISSN 0022-4928. doi: 10.1175/jas3583.1.

Larsen, M. L., Kostinski, A. B., and Jameson, A. R. Further evidence for superterminal raindrops. *Geophysical Research Letters*, 41(19):6914–6918, 2014. ISSN 1944-8007. doi: 10.1002/2014gl061397.

Lee, G., Bringi, V., and Thurai, M. The Retrieval of Drop Size Distribution Parameters Using a Dual-Polarimetric Radar. *Remote Sensing*, 15(4):1063, 2023. ISSN 2072-4292. doi: 10.3390/rs15041063.

Lee, J.-E., Jung, S.-H., Park, H.-M., Kwon, S., Lin, P.-L., and Lee, G. Classification of precipitation types using fall velocity-diameter relationships from 2D-video distrometer measurements. *Advances in Atmospheric Sciences*, 32(9):1277–1290, 2015. ISSN 1861-9533. doi: 10.1007/s00376-015-4234-4.

Leijnse, H. and Uijlenhoet, R. The effect of reported high-velocity small raindrops on inferred drop size distributions and derived power laws. *Atmospheric Chemistry and Physics*, 10(14):6807–6818, 2010. ISSN 1680-7324. doi: 10.5194/acp-10-6807-2010.

Leijnse, H., Uijlenhoet, R., and Berne, A. Errors and Uncertainties in Microwave Link Rainfall Estimation Explored Using Drop Size Measurements and High-Resolution Radar Data. *Journal of Hydrometeorology*, 11(6):1330–1344, 2010a. ISSN 1525-755X. doi: 10.1175/2010jhm1243.1.

Leijnse, H., Uijlenhoet, R., van de Beek, C. Z., Overeem, A., Otto, T., Unal, C. M. H., Dufournet, Y., Russchenberg, H. W. J., Figueras i Ventura, J., Klein Baltink, H., and Holleman, I. Precipitation Measurement at CESAR, the Netherlands. *Journal of Hydrometeorology*, 11(6):1322–1329, 2010b. ISSN 1525-755X. doi: 10.1175/2010jhm1245.1.

Liu, X., Wan, Q., Wang, H., Xiao, H., Zhang, Y., Zheng, T., and Feng, L. Raindrop Size Distribution Parameters Retrieved from Guangzhou S-band Polarimetric Radar Observations. *Journal of Meteorological Research*, 32(4):571–583, 2018. ISSN 2198-0934. doi: 10.1007/s13351-018-7152-4.

Liu, X., He, B., Zhao, S., Hu, S., and Liu, L. Comparative measurement of rainfall with a precipitation micro-physical characteristics sensor, a 2D video disdrometer, an OTT PARSIVEL disdrometer, and a rain gauge. *Atmospheric Research*, 229:100–114, 2019. ISSN 0169-8095. doi: 10.1016/j.atmosres.2019.06.020.

Liu, X. C., Gao, T. C., and Liu, L. A comparison of rainfall measurements from multiple instruments. *Atmospheric Measurement Techniques*, 6(7):1585–1595, 2013. ISSN 1867-8548. doi: 10.5194/amt-6-1585-2013.

Liu, X. C., Gao, T. C., and Liu, L. A video precipitation sensor for imaging and velocimetry of hydrometeors. *Atmospheric Measurement Techniques*, 7(7):2037–2046, 2014. ISSN 1867-8548. doi: 10.5194/amt-7-2037-2014.

Locatelli, J. D. and Hobbs, P. V. Fall speeds and masses of solid precipitation particles. *Journal of Geophysical Research*, 79(15):2185–2197, 1974. ISSN 0148-0227. doi: 10.1029/jc079i015p02185.

Löffler-Mang, M. and Joss, J. An Optical Disdrometer for Measuring Size and Velocity of Hydrometeors. *Journal of Atmospheric and Oceanic Technology*, 17(2):130–139, 2000. ISSN 1520-0426. doi: 10.1175/1520-0426(2000)017⟨0130:aodfms⟩2.0.co;2.

Lohmann, U. and Feichter, J. Global indirect aerosol effects: a review. *Atmospheric Chemistry and Physics*, 5(3):715–737, 2005. doi: 10.5194/acp-5-715-2005.

Löhnert, U., Kneifel, S., Battaglia, A., Hagen, M., Hirsch, L., and Crewell, S. A Multisensor Approach Toward a Better Understanding of Snowfall Microphysics: The TOSCA

Project. *Bulletin of the American Meteorological Society*, 92(5):613–628, 2011. ISSN 1520-0477. doi: 10.1175/2010bams2909.1.

Luo, L., Guo, J., Chen, H., Yang, M., Chen, M., Xiao, H., Ma, J., and Li, S. Microphysical Characteristics of Rainfall Observed by a 2DVD Disdrometer during Different Seasons in Beijing, China. *Remote Sensing*, 13(12):2303, 2021. ISSN 2072-4292. doi: 10.3390/rs13122303.

Maeso, J., Bringi, V. N., Cruz-Pol, S., and Chandrasekar, V. DSD characterization and computations of expected reflectivity using data from a two-dimensional video disdrometer deployed in a tropical environment. In *Proceedings. 2005 IEEE International Geoscience and Remote Sensing Symposium, 2005. IGARSS'05.*, volume 7, pages 5073–5076. IEEE, 2005.

Marzuki, Randeu, W. L., Kozu, T., Shimomai, T., Hashiguchi, H., and Schönhuber, M. Raindrop axis ratios, fall velocities and size distribution over Sumatra from 2D-Video Disdrometer measurement. *Atmospheric Research*, 119:23–37, 2013. ISSN 0169-8095. doi: 10.1016/j.atmosres.2011.08.006.

Marzuki, M., Randeu, W. L., Sch?nhuber, M., Bringi, V. N., Kozu, T., and Shimomai, T. Raindrop Size Distribution Parameters of Distrometer Data With Different Bin Sizes. *IEEE Transactions on Geoscience and Remote Sensing*, 48(8):3075–3080, 2010. ISSN 1558-0644. doi: 10.1109/tgrs.2010.2043955.

Miriovsky, B. J., Bradley, A. A., Eichinger, W. E., Krajewski, W. F., Kruger, A., Nelson, B. R., Creutin, J.-D., Lapetite, J.-M., Lee, G. W., Zawadzki, I., and Ogden, F. L. An Experimental Study of Small-Scale Variability of Radar Reflectivity Using Disdrometer Observations. *Journal of Applied Meteorology*, 43(1):106–118, 2004. ISSN 1520-0450. doi: 10.1175/1520-0450(2004)043⟨0106:aesosv⟩2.0.co;2.

Mülmenstädt, J., Sourdeval, O., Delanoë, J., and Quaas, J. Frequency of occurrence of rain from liquid-, mixed-, and ice-phase clouds derived from A-Train satellite retrievals. *Geophysical Research Letters*, 42(15):6502–6509, 2015. doi: 10.1002/2015gl064604.

Myagkov, A., Seifert, P., Wandinger, U., Bühl, J., and Engelmann, R. Relationship between temperature and apparent shape of pristine ice crystals derived from polarimetric cloud radar observations during the ACCEPT campaign. *Atmospheric Measurement Techniques*, 9(8):3739–3754, 2016. doi: 10.5194/amt-9-3739-2016.

Nešpor, V., Krajewski, W. F., and Kruger, A. Wind-Induced Error of Raindrop Size Distribution Measurement Using a Two-Dimensional Video Disdrometer. *Journal of Atmospheric and Oceanic Technology*, 17(11):1483–1492, 2000. ISSN 1520-0426. doi: 10.1175/1520-0426(2000)017⟨1483:wieors⟩2.0.co;2.

Nishikawa, M., Nakamura, K., Fujiyoshi, Y., Nakagawa, K., Hanado, H., Minda, H., Nakai, S., Kumakura, T., and Oki, R. Radar Attenuation and Reflectivity Measurements of Snow With Dual Ka-Band Radar. *IEEE Transactions on Geoscience and Remote Sensing*, 54(2):714–722, 2016. ISSN 1558-0644. doi: 10.1109/tgrs.2015.2464099.

Okazaki, M., Oishi, S., Awata, Y., Yanase, T., and Takemi, T. An analytical representation of raindrop size distribution in a mixed convective and stratiform precipitating system as revealed by field observations. *Atmospheric Science Letters*, 24(6), 2023. ISSN 1530-261X. doi: 10.1002/asl.1155.

Omanovic, N., Ferrachat, S., Fuchs, C., Henneberger, J., Miller, A. J., Ohneiser, K., Ramelli, F., Seifert, P., Spirig, R., Zhang, H., and Lohmann, U. Evaluating the Wegener-Bergeron-Findeisen process in ICON in large-eddy mode with in situ observations from the CLOUDLAB project. *EGUsphere*, 2024. doi: 10.5194/egusphere-2023-3029.

Park, S.-G., Kim, H.-L., Ham, Y.-W., and Jung, S.-H. Comparative Evaluation of the OTT PARSIVEL2 Using a Collocated Two-Dimensional Video Disdrometer. *Journal of Atmospheric and Oceanic Technology*, 34(9):2059–2082, 2017. ISSN 1520-0426. doi: 10.1175/jtech-d-16-0256.1.

Petersen, W. A., Bringi, V. N., Gatlin, P., Phillips, D., Schwaller, M., Tokay, A., Wingo, M., and Wolff, D. Distributed disdrometer and rain gauge measurement infrastructure developed for GPM Ground Validation. In *2010 American Geolophysical Union (AGU) Fall Meeting/AGU*, number M11-0049, 2010.

Pettersen, C., Bliven, L. F., von Lerber, A., Wood, N. B., Kulie, M. S., Mateling, M. E., Moisseev, D. N., Munchak, S. J., Petersen, W. A., and Wolff, D. B. The Precipitation Imaging Package: Assessment of Microphysical and Bulk Characteristics of Snow. *Atmosphere*, 11(8):785, 2020. ISSN 2073-4433. doi: 10.3390/atmos11080785.

Prodi, F., Tagliavini, A., and Pasqualucci, F. Pludix: An X-band sensor for measuring hydrometeors size distributions and fall rate. In *Proc. 13th Int. Conf. on Clouds and Precipitation*, pages 338–339, 2000.

Radenz, M., Bühl, J., Seifert, P., Griesche, H., and Engelmann, R. peakTree: a framework for structure-preserving radar Doppler spectra analysis. *Atmospheric Measurement Techniques*, 12(9):4813–4828, 2019. doi: 10.5194/amt-12-4813-2019.

Radenz, M., Bühl, J., Seifert, P., Baars, H., Engelmann, R., González, B. B., Mamouri, R.-E., Zamorano, F., and Ansmann, A. Hemispheric contrasts in ice formation in stratiform mixed-phase clouds: disentangling the role of aerosol and dynamics with ground-based remote sensing. *Atmospheric Chemistry and Physics*, 21(23):17969–17994, 2021. doi: 10.5194/acp-21-17969-2021.

Ramelli, F., Beck, A., Henneberger, J., and Lohmann, U. Using a holographic imager on a tethered balloon system for microphysical observations of boundary layer clouds. *Atmospheric Measurement Techniques*, 13(2):925–939, 2020. doi: 10.5194/amt-13-925-2020.

Ramelli, F., Henneberger, J., David, R. O., Bühl, J., Radenz, M., Seifert, P., Wieder, J., Lauber, A., Pasquier, J. T., Engelmann, R., Mignani, C., Hervo, M., and Lohmann, U. Microphysical investigation of the seeder and feeder region of an Alpine mixed-phase cloud. *Atmospheric Chemistry and Physics*, 21(9):6681–6706, 2021. doi: 10.5194/acp-21-6681-2021.

Randeu, W. L., Schönhuber, M., and Lammer, G. Real-time measurements and analyses of precipitation micro-structure and dynamics. *Proc. of ERAD (2002)*, pages 78–83, 2002.

Raupach, T. H. and Berne, A. Correction of raindrop size distributions measured by Parsivel disdrometers, using a two-dimensional video disdrometer as a reference. *Atmospheric Measurement Techniques*, 8(1):343–365, 2015. ISSN 1867-8548. doi: 10.5194/amt-8-343-2015.

Raupach, T. H., Gires, A., Tchiguirinskaia, I., Schertzer, D., and Berne, A. Multifractal Analysis of Snowfall Recorded Using a 2D Video Disdrometer. *Journal of Hydrometeorology*, 18(9):2453–2468, 2017. ISSN 1525-7541. doi: 10.1175/jhm-d-16-0224.1.

Schönhuber, M., Urban, H. E., Poiares Baptista, J. P. V., Randeu, W. L., and Riedler, W. Weather radar versus 2D-video-distrometer data. *Weather Radar Technology for Water Resources Management*, 159:171, 1997.

Schönhuber, M., Randeu, W. L., and Poiares Baptista, J. P. V. Application of the 2D-video-distrometer for weather radar data inversion. *Physics and Chemistry of the Earth,* *Part B: Hydrology, Oceans and Atmosphere*, 25(10–12):1037–1042, 2000. ISSN 1464-1909. doi: 10.1016/s1464-1909(00)00149-0.

Schönhuber, M., Lammer, G., and Randeu, W. L. One decade of imaging precipitation measurement by 2D-video-distrometer. *Advances in Geosciences*, 10:85–90, 2007. doi: 10.5194/adgeo-10-85-2007.

Schönhuber, M., Schwinzerl, M., and Lammer, G. 3D Reconstruction of 2DVD-measured Raindrops for Precise Prediction of Propagation Parameters. In *2016 10th European Conference on Antennas and Propagation (EuCAP)*. IEEE, 2016. doi: 10.1109/eucap.2016.7481929.

Schuur, T. J., Ryzhkov, A. V., Zrnić, D. S., and Schönhuber, M. Drop Size Distributions Measured by a 2D Video Disdrometer: Comparison with Dual-Polarization Radar Data. *Journal of Applied Meteorology*, 40(6):1019–1034, 2001. ISSN 1520-0450. doi: 10.1175/1520-0450(2001)040⟨1019:dsdmba⟩2.0.co;2.

Shakti, P. C., Maki, M., Shimizu, S., Maesaka, T., Kim, D.-S., Lee, D.-I., and Iida, H. Correction of reflectivity in the presence of partial beam blockage over a mountainous region using X-band dual polarization radar. *Journal of Hydrometeorology*, 14(3):744–764, 2013. doi: 10.1175/JHM-D-12-077.1.

Sheppard, B. E. Measurement of Raindrop Size Distributions Using a Small Doppler Radar. *Journal of Atmospheric and Oceanic Technology*, 7(2):255–268, 1990. ISSN 1520-0426. doi: 10.1175/1520-0426(1990)007⟨0255:morsdu⟩2.0.co;2.

Shupe, M. D., Rex, M., Blomquist, B., Persson, P. O. G., Schmale, J., Uttal, T., Althausen, D., Angot, H., Archer, S., Bariteau, L., Beck, I., Bilberry, J., Bucci, S., Buck, C., Boyer, M., Brasseur, Z., Brooks, I. M., Calmer, R., Cassano, J., Castro, V., Chu, D., Costa, D., Cox, C. J., Creamean, J., Crewell, S., Dahlke, S., Damm, E., de Boer, G., Deckelmann, H., Dethloff, K., Dütsch, M., Ebell, K., Ehrlich, A., Ellis, J., Engelmann, R., Fong, A. A., Frey, M. M., Gallagher, M. R., Ganzeveld, L., Gradinger, R., Graeser, J., Greenamyer, V., Griesche, H., Griffiths, S., Hamilton, J., Heinemann, G., Helmig, D., Herber, A., Heuzé, C., Hofer, J., Houchens, T., Howard, D., Inoue, J., Jacobi, H.-W., Jaiser, R., Jokinen, T., Jourdan, O., Jozef, G., King, W., Kirchgaessner, A., Klingebiel, M., Krassovski, M., Krumpen, T., Lampert, A., Landing, W., Laurila, T., Lawrence, D., Lonardi, M., Loose, B., Lüpkes, C., Maahn, M., Macke, A., Maslowski, W., Marsay, C., Maturilli, M., Mech, M., Morris, S., Moser, M., Nicolaus, M., Ortega, P., Osborn, J., Pätzold, F., Perovich, D. K., Petäjä, T., Pilz, C., Pirazzini, R., Posman, K., Powers, H., Pratt, K. A., Preußer, A., Quéléver, L., Radenz, M., Rabe, B., Rinke, A., Sachs, T., Schulz, A., Siebert, H., Silva, T., Solomon, A., Sommerfeld, A., Spreen, G., Stephens, M., Stohl, A., Svensson, G., Uin, J., Viegas, J., Voigt, C., von der Gathen, P., Wehner, B., Welker, J. M., Wendisch, M., Werner, M., Xie, Z., and Yue, F. Overview of the MOSAiC expedition: Atmosphere. *Elem Sci Anth*, 10(1), 2022. ISSN 2325-1026. doi: 10.1525/elementa.2021.00060.

Suh, S.-H., Kim, H.-I., Choi, E.-H., and You, C.-H. Estimation of Liquid Fraction of Wet Snow by Using 2-D Video Disdrometer and S-Band Weather Radar. *Remote Sensing*, 13(10):1901, 2021. ISSN 2072-4292. doi: 10.3390/rs13101901.

Tao, R., Zhao, K., Huang, H., Wen, L., Zhang, G., Zhou, A., and Chen, H. Snow Particle Size Distribution From a 2-D Video Disdrometer and Radar Snowfall Estimation in East China. *IEEE Transactions on Geoscience and Remote Sensing*, pages 1–12, 2020. ISSN 1558-0644. doi: 10.1109/tgrs.2020.2990920.

Teisseire, A., Seifert, P., Myagkov, A., Bühl, J., and Radenz, M. Determination of the vertical distribution of in-cloud particle shape using SLDR-mode 35GHz scanning cloud radar. *Atmospheric Measurement Techniques*, 17(3):999–1016, 2024. ISSN 1867-8548. doi: 10.5194/amt-17-999-2024.

Testik, F. Y. and Pei, B. Wind Effects on the Shape of Raindrop Size Distribution. *Journal of Hydrometeorology*, 18(5):1285–1303, 2017. ISSN 1525-7541. doi: 10.1175/jhm-d-16-0211.1.

Thurai, M. and Bringi, V. N. Drop Axis Ratios from a 2D Video Disdrometer. *Journal of Atmospheric and Oceanic Technology*, 22(7):966–978, 2005. ISSN 0739-0572. doi: 10.1175/jtech1767.1.

Thurai, M. and Bringi, V. N. Application of the Generalized Gamma Model to Represent the Full Rain Drop Size Distribution Spectra. *Journal of Applied Meteorology and Climatology*, 57(5):1197–1210, 2018. ISSN 1558-8432. doi: 10.1175/jamc-d-17-0235.1.

Thurai, M., Huang, G. J., Bringi, V. N., Randeu, W. L., and Schönhuber, M. Drop Shapes, Model Comparisons, and Calculations of Polarimetric Radar Parameters in Rain. *Journal of Atmospheric and Oceanic Technology*, 24(6):1019–1032, 2007. ISSN 1520-0426. doi: 10.1175/jtech2051.1.

Thurai, M., Williams, C. R., and Bringi, V. N. Examining the correlations between drop size distribution parameters using data from two side-by-side 2D-video disdrometers. *Atmospheric Research*, 144:95–110, 2014. ISSN 0169-8095. doi: 10.1016/j.atmosres.2014.01.002.

Thurai, M., Gatlin, P., Bringi, V. N., Petersen, W., Kennedy, P., Notaroš, B., and Carey, L. Toward Completing the Raindrop Size Spectrum: Case Studies Involving 2D-Video Disdrometer, Droplet Spectrometer, and Polarimetric Radar Measurements. *Journal of Applied Meteorology and Climatology*, 56(4):877–896, 2017a. ISSN 1558-8432. doi: 10.1175/jamc-d-16-0304.1.

Thurai, M., Mishra, K. V., Bringi, V. N., and Krajewski, W. F. Initial Results of a New Composite-Weighted Algorithm for Dual-Polarized X-Band Rainfall Estimation. *Journal of Hydrometeorology*, 18(4):1081–1100, 2017b. ISSN 1525-7541. doi: 10.1175/jhm-d-16-0196.1.

Tokay, A., Chamberlain, R., and Schönhuber, M. Laboratory and field measurements of raindrop oscillations. *Physics and Chemistry of the Earth, Part B: Hydrology, Oceans and Atmosphere*, 25(10–12):867–870, 2000. ISSN 1464-1909. doi: 10.1016/s1464-1909(00)00117-9.

Tokay, A., Kruger, A., and Krajewski, W. F. Comparison of Drop Size Distribution Measurements by Impact and Optical Disdrometers. *Journal of Applied Meteorology*, 40(11):2083–2097, 2001. ISSN 1520-0450. doi: 10.1175/1520-0450(2001)040⟨2083:codsdm⟩2.0.co;2.

Tokay, A., Kruger, A., Krajewski, W. F., Kucera, P. A., and Filho, A. J. P. Measurements of drop size distribution in the southwestern Amazon basin. *Journal of Geophysical Research: Atmospheres*, 107(D20), 2002. ISSN 0148-0227. doi: 10.1029/2001jd000355.

Tokay, A., Petersen, W. A., Gatlin, P., and Wingo, M. Comparison of Raindrop Size Distribution Measurements by Collocated Disdrometers. *Journal of Atmospheric and Oceanic Technology*, 30(8):1672–1690, 2013. ISSN 1520-0426. doi: 10.1175/jtech-d-12-00163.1.

Uijlenhoet, R., Porrà, J. M., Torres, D. S., and Creutin, J.-D. Analytical solutions to sampling effects in drop size distribution measurements during stationary rainfall: Estimation of bulk rainfall variables. *Journal of Hydrology*, 328(1–2):65–82, 2006. ISSN 0022-1694. doi: 10.1016/j.jhydrol.2005.11.043.

Wegener, A. *Thermodynamik der atmosphäre*. Barth, J. A., 1911.

Wen, G., Xiao, H., Yang, H., Bi, Y., and Xu, W. Characteristics of summer and winter precipitation over northern China. *Atmospheric Research*, 197:390–406, 2017. ISSN 0169-8095. doi: 10.1016/j.atmosres.2017.07.023.

Wen, L., Zhao, K., Chen, G., Wang, M., Zhou, B., Huang, H., Hu, D., Lee, W., and Hu, H. Drop Size Distribution Characteristics of Seven Typhoons in China. *Journal of Geophysical Research: Atmospheres*, 123(12):6529–6548, 2018. ISSN 2169-8996. doi: 10.1029/2017jd027950.

Wen, L., Zhao, K., Wang, M., and Zhang, G. Seasonal Variations of Observed Raindrop Size Distribution in East China. *Advances in Atmospheric Sciences*, 36(4):346–362, 2019. ISSN 1861-9533. doi: 10.1007/s00376-018-8107-5.

Wetterzentrale. DWD ground data. `https://www.wetterzentrale.de/reanalysis.php?jaar=2023&maand=1&dag=18&uur=000&var=45&map=1&model=dwd`, 2023a. Last access: 6 February 2024.

Wetterzentrale. GFS 850hPa geopotential and temperature. `https://www.wetterzentrale.de/reanalysis.php?map=1&model=avn&var=2&jaar=2023&maand=1&dag=18&h=0&nmaps=24`, 2023b. Last access: 6 February 2024.

Williams, C. R., Kruger, A., Gage, K. S., Tokay, A., Cifelli, R., Krajewski, W. F., and Kummerow, C. Comparison of simultaneous rain drop size distributions estimated from two surface disdrometers and a UHF profiler. *Geophysical Research Letters*, 27(12): 1763–1766, 2000. ISSN 1944-8007. doi: 10.1029/1999gl011100.

Williams, C. R., Bringi, V. N., Carey, L. D., Chandrasekar, V., Gatlin, P. N., Haddad, Z. S., Meneghini, R., Joseph Munchak, S., Nesbitt, S. W., Petersen, W. A., Tanelli, S., Tokay, A., Wilson, A., and Wolff, D. B. Describing the Shape of Raindrop Size Distributions Using Uncorrelated Raindrop Mass Spectrum Parameters. *Journal of Applied Meteorology and Climatology*, 53(5):1282–1296, 2014. ISSN 1558-8432. doi: 10.1175/jamc-d-13-076.1.

Zängl, G., Reinert, D., Rípodas, P., and Baldauf, M. The ICON (ICOsahedral Non-hydrostatic) modelling framework of DWD and MPI-M: Description of the non-hydrostatic dynamical core. *Quarterly Journal of the Royal Meteorological Society*, 141 (687):563–579, 2014. doi: 10.1002/qj.2378.

Zhang, G., Vivekanandan, J., and Brandes, E. A method for estimating rain rate and drop size distribution from polarimetric radar measurements. *IEEE Transactions on Geoscience and Remote Sensing*, 39(4):830–841, 2001. ISSN 0196-2892. doi: 10.1109/36.917906.

Zhang, G., Xue, M., Cao, Q., and Dawson, D. Diagnosing the Intercept Parameter for Exponential Raindrop Size Distribution Based on Video Disdrometer Observations: Model Development. *Journal of Applied Meteorology and Climatology*, 47(11):2983–2992, 2008. ISSN 1558-8424. doi: 10.1175/2008jamc1876.1.

Zhang, G., Luchs, S., Ryzhkov, A., Xue, M., Ryzhkova, L., and Cao, Q. Winter Precipitation Microphysics Characterized by Polarimetric Radar and Video Disdrometer Observations in Central Oklahoma. *Journal of Applied Meteorology and Climatology*, 50(7):1558–1570, 2011. ISSN 1558-8432. doi: 10.1175/2011jamc2343.1.

Zhang, Y., Zheng, H., Zhang, L., Huang, Y., Liu, X., and Wu, Z. Assessing the Effect of Riming on Snow Microphysics: The First Observational Study in East China. *Journal of Geophysical Research: Atmospheres*, 126(7), 2021. ISSN 2169-8996. doi: 10.1029/2020jd033763.

Zheng, H., Zhang, Y., Li, H., Wu, Z., and Zhou, Z. Revisiting Raindrop Axis Ratios Based on 3D Oblate Spheroidal Reconstruction: 2D Video Disdrometer Observations During Tropical Cyclone Passages. *Geophysical Research Letters*, 50(9), 2023. ISSN 1944-8007. doi: 10.1029/2023gl103281.

Zhou, L., Dong, X., Fu, Z., Wang, B., Leng, L., Xi, B., and Cui, C. Vertical Distributions of Raindrops and Z-R Relationships Using Microrain Radar and 2-D-Video Distrometer Measurements During the Integrative Monsoon Frontal Rainfall Experiment (IMFRE). *Journal of Geophysical Research: Atmospheres*, 125(3), 2020. ISSN 2169-8996. doi: 10.1029/2019jd031108.

Selbstständigkeitserklärung

Hiermit erkläre ich, dass ich die vorliegende Masterarbeit selbstständig und nur unter Verwendung der angegebenen Literatur und Hilfsmittel angefertigt habe. Die aus fremden Quellen direkt oder indirekt übernommenen Stellen sind als solche kenntlich gemacht. Die Arbeit wurde bisher in gleicher oder ähnlicher Form keiner anderen Prüfungsbehörde vorgelegt und auch nicht veröffentlicht.

Leipzig, 29. Februar 2024